MULTILAYER FILMS FOR CORROSION PROTECTION OF METALS

& MECHANICAL BEHAVIOR OF POLYELECTROLYTE COMPLEXES

A Dissertation

by

PILAR CONSTANZA SUAREZ-MARTINEZ

Submitted to the Office of Graduate and Professional Studies of
Texas A&M University
in partial fulfillment of the requirements for the degree of

DOCTOR OF PHILOSOPHY

Chair of Committee,	Jodie Lutkenhaus
Committee Members,	Micah Green
	Yossef Elabd
	Homero Castaneda-Lopez
Head of Department,	Nazmul Karim

December 2018

Major Subject: Chemical Engineering

ABSTRACT

Polyelectrolyte complexes (PECs) and polyelectrolyte multilayers (PEMs) have become materials of interest due to their potential applications. As for every other material, understanding their properties under conditions of use (temperature, humidity, ionic strength, etc) is paramount. This work comprises two main sections.

Section one addresses the need for an efficient, environment-friendly, and scalable chromium-free surface pretreatment coating. Environment-friendly materials such as sodium montmorillonite clay (MMT) and branched polyethylenimine (BPEI) were used to prepare PEM coatings through techniques such as spray-assisted layer-by-layer assembly (LbL) and airbrushing of a one-pot formulation. PEM coatings prepared through LbL contained 25 wt% MMT, while MMT content was tailorable for coatings prepared with the one-pot formulation. Salt spray testing and electrochemical impedance spectroscopy were used to assess the corrosion protection provided by BPEI/MMT PEM coatings to an aluminum alloy. Results indicated that corrosion protection improved with increasing both coating thickness and clay content in the coating. Thus, a 2 μm thick BPEI/MMT PEM coating with 80 wt% MMT demonstrated the best corrosion protection performance, where MMT provided a physical barrier to corrosive agents and BPEI provided surface buffering and structural support.

Section two addresses a literature gap regarding PECs dynamic mechanical behavior as a function of water content, important information for any potential use of PECs in real life applications. PECs were prepared from poly(allylamine hydrochloride) (PAH) and poly(acrylic acid) (PAA). PAH/PAA PEC films were made through compression molding and preconditioned to specific relative humidity values before mechanical testing. A dynamic mechanical analyzer

was used to test the dynamic mechanical behavior of PAH/PAA PEC films under different temperature and humidity conditions over a 10^{-1} to 10^{1} Hz frequency range. Data showed that increasing both water content and temperature decreased the moduli of the material. Water increased the free volume in the PEC, weakening the intrinsic ion paring. Temperature weakened the hydrogen bonding between water and the polyelectrolytes, promoting the relaxation of polyelectrolyte chains. Finally, time-temperature and time-water superposition principles were successfully applied and validated.

DEDICATION

I would like to dedicate this accomplishment to

my parents, Rafael and Nubia,

my sister, Diana,

my nephew, Samuel,

and my husband, Kerron.

You all are the love of my life.

ACKNOWLEDGEMENTS

I would like to thank Axalta Coating Systems and the National Science Foundation for funding the work in this dissertation. Special thanks go to Axalta Coating Systems for welcoming me in their internships program twice.

I would like to thank my advisor Prof. Jodie Lutkenhaus. She has been an excellent mentor always providing me with opportunities to learn and grow. She trusted my capabilities to successfully execute projects and to mentor graduate and undergraduate students. Most importantly, she always made time to individually meet with me in order to provide guidance and to discuss experimental plans, results, setbacks, etc. She also took the time to carefully edit manuscripts together, so I would become a better writer. In general, she provided all available resources for my professional development; she not only cared about my technical skills but also my soft skills. She helped me become a better team player, engineer, leader, and mentor. Thank you!

I would like to thank my committee members, Prof. Yossef Elabd, Prof. Micah Green, and Prof. Homero Castaneda-Lopez, for their collaboration, feedback and advice. Their feedback made my work better and pushed me to become a better engineer. Special thanks to Prof. Castaneda-Lopez for his guidance regarding electrochemical impedance spectroscopy measurements and to Prof. Green for making his laboratory resources available for viscosity measurements.

I would like to thank Prof. James Holste and Prof. Kenneth R. Hall for welcoming me into their research group and for providing me with endless opportunities to learn and develop myself. I would not be at Texas A&M University without their support and encouragement.

I would like to thank Prof. Patricia Goodson for her great service with the P.O.W.E.R program at Texas A&M University. Learning about P.O.W.E.R turned my life around. She was key during the writing process of this dissertation; she provided me with support, advice, resources, and feedback.

I would also like to thank other wonderful people I met during my journey in the Ph.D. program: Dr. Harris for his career advice; my mentors Dr. Tatiana Eliseeva, and Dr. Robert Nahas who taught me about corrosion, coatings, and life; Dr. Robert Nahas, Prof. Jerome Robinson, and Dr. Douglas Cinoman for their valuable feedback and collaboration during the development of the corrosion project; Dr. Bisrat for her help and feedback during EDS and SEM measurements; Yenny Cubides for her instrumental help on the set up of electrochemical impedance spectroscopy experiments; Towanna Arnold, Ashley Stokes, and Terah Cooper for their valuable help navigating the Texas A&M system; and P.O.W.E.R consultants, Patrick Lathrop, Smit Shah, Hyosung An, and Olivia Wright for proofreading and providing feedback to make this dissertation better.

When I left Colombia to come to the United States, I left my Colombian family behind but not forgotten. Surprisingly, I left one family to be welcomed by four: my Trinidadian family, Holste's family, Lutkenhaus lab family, and friends. I would like to thank my Trinidadian family — especially Lincoln and Tricia — for welcoming me into the family and for supporting me throughout this journey; Prof. Holste and his wife Cathy for always making me feel welcomed and cared for; my co-workers and colleagues, some of which have become lifetime friends, for their feedback and support; and my closest friends, Bob, Patrick, Kevin, Pritishma and Behnaz for their support and for sometimes taking me away from work (I will miss you guys … but I am ready to graduate).

Finally and most importantly, I would like to thank my parents, Rafael and Nubia, for laying a strong and solid foundation that ultimately defined the woman and engineer that I am today. I would like to thank my sister, Diana, for her company and unstoppable support, but most importantly for bringing my nephew, Samuel, to this world. I would like to thank my husband, Kerron, for sharing with me this adventure and always believe in me. I have learnt a great deal from him; he has helped me grow immensely as a person and an engineer.

CONTRIBUTORS AND FUNDING SOURCES

Contributors

This work was supported and supervised by a dissertation committee consisting of Professors Jodie Lutkenhaus, Micah Green, and Yossef Elabd of the Department of Chemical Engineering and Professor Homero Castaneda-Lopez of the Department of Materials Science and Engineering.

Salt spray tests in Chapters II and III were performed by Axalta Coating Systems. X-ray photoelectron spectroscopy (XPS), X-ray diffraction (XRD), energy-dispersive X-ray spectroscopy (EDS), and cryogenic transmission electron microscopy (TEM) measurements, in Chapters II and III, were performed by Dr. Hyosung An, Dr. Anup Bandyopadhyay, Dr. Yordanos Bisrat, and Dr. Alexander Ribbe, respectively. Viscosity measurements in Chapter III were performed by Professor Micah Green and Mr. Aaron Moran.

All other work conducted for the dissertation was completed by the student independently.

Funding Sources

Graduate study and this work were supported by Axalta Coatings System under Grant and by the National Science Foundation under Grant Number 1609696.

NOMENCLATURE

a_T	Temperature-dependent shift factor
a_W	Water-dependent shift factor
AA	Aluminum alloy
AFM	Atomic force spectroscopy
AGC_{16}	1,3-bis(N,N-dimethyl-N-cetylammonium)-2-propylacrylate dibromide
ALG	Alginic acid
B	Slope obtained from the linear behavior of a_W with W
BPEI	Branched polyethylenimine
C_1	Empirically adjustable parameter
C_2	Empirically adjustable parameter
CCC	Chromium conversion coating
CHI	Chitosan
Cr	Chromium
Cr(III)	Trivalent chromium
Cr(VI)	Hexavalent chromium
CS	Chondroitin sulfate
DMA	Dynamic mechanical analysis
DMTA	Dynamic mechanical thermal analysis
E	Young's modulus or Elastic modulus
E_a	Activation energy
E*	Complex modulus

E’	Storage Modulus
E”	Loss Modulus
EIS	Electrochemical impedance spectroscopy
f	Frequency
F127	Triblock copolymer PluronicVR
G	Shear modulus
GO	Graphene oxide
LbL	Layer-by-layer
LPEI	Linear polyethylenimine
MDSC	Modulated differential scanning calorimetry
MMT	Sodium montmorillonite clay
Mw	Molecular weight
NCF	Nanofibrillated cellulose
NMC	Nanomechanical cantilever
NTS	Trisodium 1,3,6-naphthalenetrisulfonate
O	Oxygen
OTR	Oxygen transmission rate
PAA	Poly(acrylic acid)
PAH	Poly(allylamine hydrochloride)
PDADMA	Poly(diallyldimethylammonium chloride)
PDDA	Poly(diallyldimethyldiammonium chloride)
PDMAEMA	Poly(N,N-dimethylaminoethyl methacrylate)
PDMS	Poly(dimethylsiloxane)

PEC	Polyelectrolyte Complex
PEG	Poly(ethylene glycol)
PEI	Polyethylenimine
PEM	Polyelectrolyte multilayer
PEO	Poly(ethylene oxide)
PET	Polyethylene terephthalate ST505
P-Et-P	Poly(triethyl(4-vinylbenzyl)phosphonium chloride)
PLGA	Poly-L-glutamic acid
PLK	Poly(L-lysine hydrochloride)
PLL	Poly-L-lysine
PMMA	Poly(methacrylic acid)
PMPTC	Poly(3-(methacryloylamino) propyl-trimethylammonium chloride)
PNaSS	Poly(sodium p-styrenesulfonate)
Pol^+	Polycation
Pol^-	Polyanion
PRE	Poly(D,L-glutamic acid sodium salt)
PS	Polystyrene
PSS	Poly(sodium 4-styrenesulfonate)
QCM-D	Quartz crystal microbalance with dissipation monitoring
QVP	Poly(4-vinylpyridine)
R	Universal gas constant
RH_{ref}	Reference relative humidity
SIEBIMM	Strain-induced elastic buckling instability for mechanical measurements

SS	Salt spray test
T	Temperature
T_{ref}	Reference temperature
T_g	Glass transition temperature
TpHSP	Time-pH superposition principle
TSSP	Time-salt superposition principle
TTSP	Time-temperature superposition principle
TTSSP	Time-temperature-salt superposition principle
THSP	Time-humidity superposition principle
UTS	Ultimate tensile strain
W	Water content
δ	Delta
σ	Stress
ε	Strain
τ	Shear stress
η	Viscosity

TABLE OF CONTENTS

TABLE OF CONTENTS

Page

LIST OF FIGURES

Page

Page

LIST OF TABLES

CHAPTER I

INTRODUCTION AND LITERATURE REVIEW

1.1 Introductory Remarks

Polyelectrolyte complexes (PECs) and polyelectrolyte multilayers (PEMs) are fundamentally formed through electrostatic attraction between oppositely charged materials (e.g., polyelectrolytes, macromolecules, and nanoparticles). Most importantly, the properties of PECs and PEMs (e.g., anticorrosive, mechanical, thermal, and electrical) are easily tailorable.

PECs were first discovered in the early 1930 by Bungenberg de Jong et al.,[1] when the mixture of two oppositely charged polyelectrolytes resulted in the formation of a coacervate PEC or a flocculated PEC. PECs, however, presented challenges regarding processability which caused researchers to lose interest in PECs and drove them to find a new technique that would allow controlled formation of PEC films or PEMs — layer-by-layer assemblies. While PECs are formed by simultaneous mixing of two oppositely charged materials, PEMs are partially stratified structures made by sequentially applying layers of oppositely charged materials onto a substrate.

Although PECs and PEMs formation relies on the same physical phenomenom, their structural arrangements, properties, and dynamics differ. Therefore, PECs and PEMs have shown potential to be used in diverse applications such as drug delivery, electronics, food packaging, pharmaceutics, biomedical devices, and corrosion protection.[2]

In this dissertation, Chapter I introduces PECs and PEMs, their potential applications, as well as their anticorrosive and mechanical properties. Chapters II and III present PEMs potential use for corrosion protection of metals and alloys. Chapter IV presents water content and

temperature effects on PECs mechanical behavior. Finally, Chapter V presents a summary and future work.

1.2 Polymers and Polyelectrolytes

Polymers are macromolecules made from repeat subunits (monomers). Polymers can be classified according to their source as: natural, semi-synthetic and synthetic.[3] Natural polymers (e.g., DNA, proteins, and silk) are obtained from natural sources; semi-synthetic polymers (e.g., rubber and cellulose nitrate) are obtained by modifying a natural polymer; and synthetic polymers (e.g., polyethylene, polypropylene, and nylon) are produced by chemical reactions commonly known as polymerization.

Polyelectrolytes (PEs) are water-soluble polymers with partially ionizable structures.[4] PEs are categorized as weak and strong according to their charge density (**Figure 1.1**). While weak PEs charge density changes as a function of pH, the charge density of strong PEs does not.

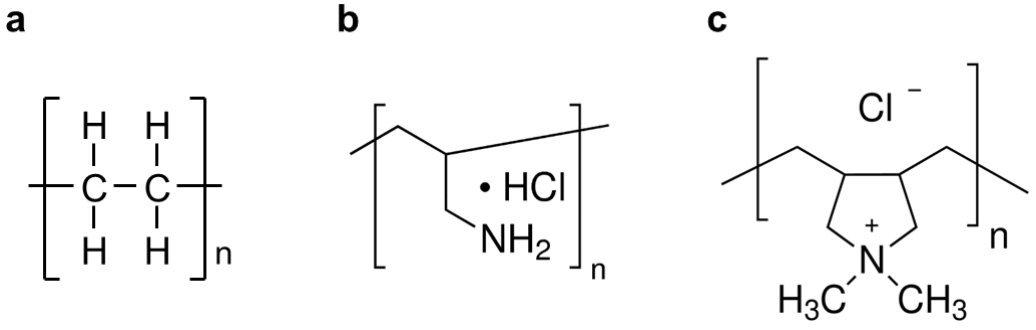

Figure 1.1 a) Polyethylene (polymer), b) poly(allylamine hydrochloride) (weak PE), and c) poly(diallyldimethylammonium chloride) (strong PE).

1.3 Polyelectrolyte Complexes (PECs) and Polyelectrolyte Multilayers (PEMs)

PECs and PEMs are the product of the strong interactions between oppositely charged macromolecules.[5] Other interactions such as hydrogen bonding, hydrophobic interactions, dipole interactions, and van der Waals forces can also generate PECs and PEMs.[3] Therefore, PECs and PEMs can be made from PEs, or by the combination of PEs with charged material such as nanoparticles (e.g., carbon nanotubes,[6-9] graphene oxide,[10-14] clay,[15-22] gold nanoparticles,[23] iron oxide nanoparticles,[24] melanine[25], MXene,[26] etc).

PECs and PEMs formation depend on assembly conditions such as PE concentration, PE ionic strength (salt content), PE charge density, PE molecular weight, assembly method/mixing ratio, temperature, and pH.[3, 27, 28] Additionally, PECs and PEMs stability depends on their conditions of use (e.g., pH, temperature, humidity, and salt).

1.3.1 Polyelectrolyte Complexes (PECs)

PECs have several morphologies — depending on preparation procedures — ranging from solid-like (polyelectrolyte complexes) to liquid-like (polyelectrolyte coacervates).[29, 30] PECs formation in solution (**Equation 1.1, Figure 1.2**) occurs after mixing, due to the electrostatic attraction between the oppositely charged polymers (**Pol^+ and Pol^-**). This ionic reaction also causes the release of associated counter-ions as free salt (**Na^+_{aq} and Cl^-_{aq}**).[5]

$$Pol^+Cl^-_{aq} + Pol^-Na^+_{aq} \rightarrow Pol^+Pol^-_s + Na^+_{aq} + Cl^-_{aq} \qquad \textbf{(Equation 1.1)}$$

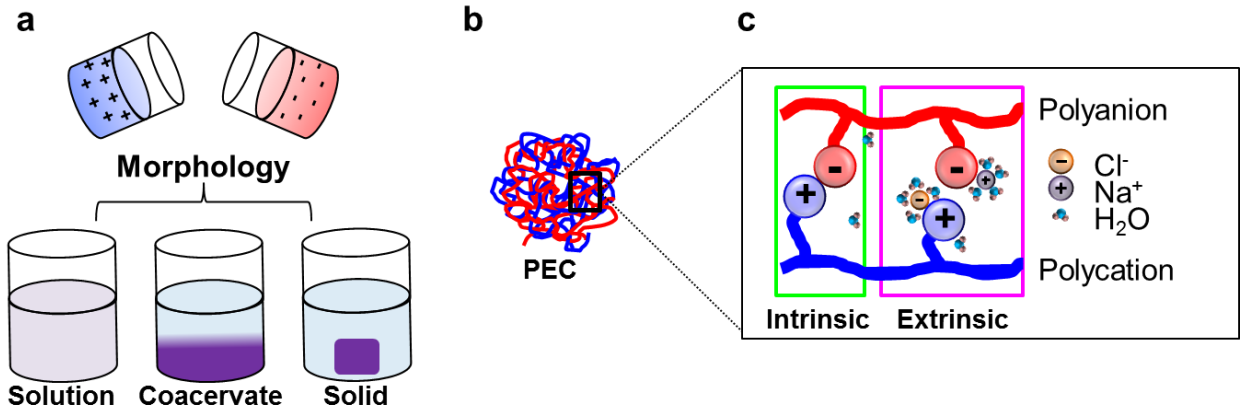

Figure 1.2 a) PEC formation from two oppositely charged polyelectrolytes (polycation and polyanion) and PEC morphology. b) Example of PECs disordered configuration. c) Intrinsic and extrinsic ion pairing within the PEC structure.

PECs morphology — comprising intrinsic and extrinsic sites — influences the properties of the PEC. [29, 31] PECs contain intrinsic and extrinsic sites depending on the presence or absence of salt during PECs preparation or post-treatment (**Equation 1.2**: Salt doping). Intrinsic sites are formed by the electrostatic interaction between oppositely charged polymer repeat units (**Pol$^+$Pol^-_s**), and extrinsic sites result from interactions of polymer repeat units and salt ions (**Pol$^+$Cl$_s^-$** and **Pol$^-$Na$_s^+$**).[29] Most importantly, PECs morphology depends on several factors: PE type,[32] molecular weight,[27] charge density,[32], stoichiometry,[29] chemical or physical cross-links,[4] water content,[33, 34] ionic strength (salt content),[5] and pH[34, 35].

$$Pol^+Pol_s^- + Na_{aq}^+ + Cl_{aq}^- \rightarrow Pol^+Cl_s^- + Pol^-Na_s^+ \qquad \textbf{(Equation 1.2)}$$

PECs were first studied by Michaels' group, who showed PECs difficulty to be processed into a determined solid form through thermal treatment or common solvents.[4] PEC intractability is attributed to high crosslink density resulting from dominant intrinsic ion pairing (Figure 1.2). Further studies confirmed that dry PECs — glassy and brittle [4] — do not show a thermal transition temperature as a result of extensive ion pairing.[34] Thus, to address PECs

unprocessability, Michaels' group proposed the use of aggressive ternary solvents.[4] These solvents break all ion pairs causing the dissociation of PE chains in the PECs to form a solution that could be dropcasted as films.[4] However, ternary solvents were not an appealing solution and made PECs unattractive for practical applications.

1.3.2 Polyelectrolyte Multilayers (PEMs)

Due to PECs intractability, researchers focused their efforts in finding a technique that would yield easily-processable PECs. In 1991, Decher's group[36] introduced a new way to process PEs into thin films — layer-by-layer (LbL) assembly. LbL assembly is an environment-friendly water-borne process, consisting in alternative deposition of oppositely charged PEs onto a substrate (**Figure 1.3**). LbL assembly allows nanometric control over PEMs thickness, roughness, and growth profile by tuning assembly conditions (PEs, pH, salt, PE concentration, and number of layers).[28, 37] Finally, although LbL assembly facilitates PECs processability as PEMs, LbL assembly does not change PEMs ion pairing. Both PECs and PEMs contain intrinsic and extrinsic ion pairing. Thus, PEMs are glassy in the absence of water, just like PECs.[38]

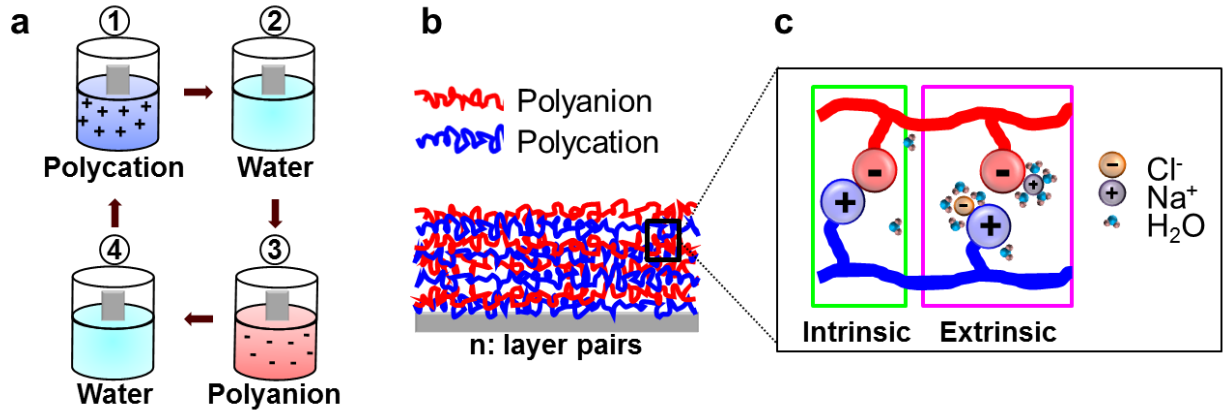

Figure 1.3 a) Dip-assisted layer-by-layer assembly of PEMs. b) Example of final product: PEM (stratified film). c) Intrinsic and extrinsic ion pairing within the PEM structure.

Researchers have extensively investigated tunability of PEMs morphology and properties as well as scalability of the LbL assembly .[28] PEMs morphology and properties highly depend on materials choice, film structure, film assembly, and film post-treatment.[20, 22, 39-43] Thus, depending on the application, materials with specific properties as well as assembly conditions (e.g., pH, ionic strength, temperature) are purposely chosen to prepare PEMs. Additionally, ways to assist the LbL assembly at an industrial scale have been explored (**Figure 1.4**) — dip, spin, spray, electromagnetic, and fluidic assembly[28, 44] — in order to cover large areas and 3D substrates while maintaining or reducing processing time.

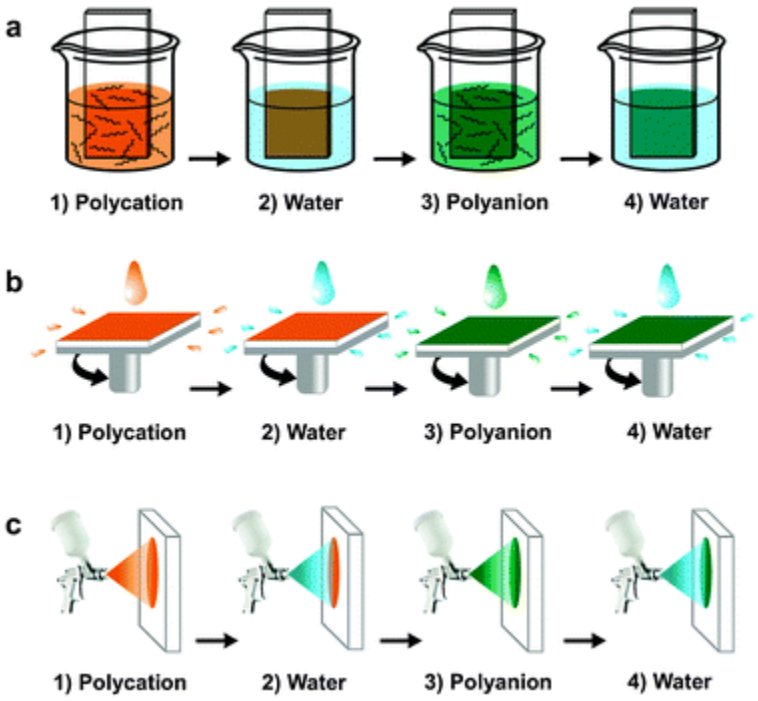

Figure 1.4 Layer-by-layer assembly technologies. a) Immersive (e.g., dip), b) spin, and c) spray. Reproduced from [45] with permission from The Royal Society of Chemistry.

1.4 Applications of PECs and PEMs

Since their discovery, PECs and PEMs have been widely studied in order to understand their structure and properties as well as their potential applications.

On one hand, PECs interdigitated structure, biocompatibility and stimuli-responsiveness (e.g., to pH, salt, temperature, humidity/water content) have motivated the study of PECs for biomedical applications such as drug delivery,[3, 46-50] gene delivery,[51, 52] and protein and peptide delivery.[53] Researchers have also investigated PECs potential use for applications where self-healing,[54] adhesion,[54] magnetic,[24] and conductive properties are desired.[27, 55]

On the other hand, PEMs stratified structure, easy processability, and their capabilities to be applied on diverse substrates have incentivized researchers to study PEMs for multiple applications: humidity sensors,[56] anti-smudge and oil and water separation,[57] anticorrosion,[15, 16, 58] biocompatibility and antibacterial efficacy for implants,[59] energy storage,[11, 60] hydrophobicity,[61, 62] gas barrier,[63, 64] etc.[57, 65]

PECs and PEMs potential applications are numerous, especially for PEMs due to their easy processability and potential industrial scalability. In this dissertation, research efforts focused on studying PEMs anticorrosion properties (Chapters II and III) and PECs mechanical behavior (Chapter IV).

1.4.1 Anticorrosion Properties

1.4.1.1 Corrosion

Corrosion is a natural spontaneous process consisting of the decay of a metal due to its reaction with the environment. In order for corrosion to take place four fundamental elements must be present: 1) anode, 2) cathode, 3) electrical contact, and 4) electrolyte. **Figure 1.5** illustrates the corrosion process in an aluminum-copper couple: aluminum behaves as the anode — where oxidation occurs — and copper behaves as the cathode — where reduction takes place.

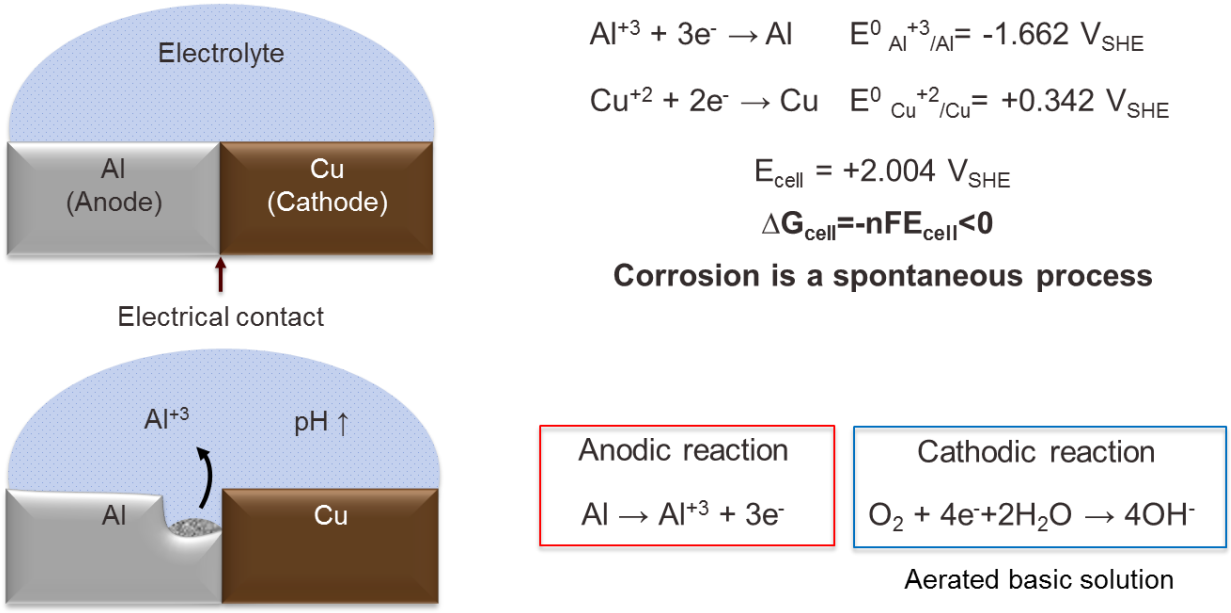

Figure 1.5 Corrosion process for an aluminum-copper couple. E^0: Standard electrode potential; E_{cell}: Cell potential; ΔG: Gibbs energy change of the cell; n: number of electrons transferred; F: Faraday's constant; SHE: Standard hydrogen electrode.

In general, oxidation of metals results in the formation of a passive layer. On one hand, this passive layer can either be porous or lack good adhesion to the metal, resulting in corrosion. On the other hand, this passive layer can be compact and resistant, providing excellent corrosion

protection, unless the passive layer is exposed to harsh conditions resulting in its break-down and continuous corrosion of the metal. Therefore, coatings are an excellent option to provide corrosion protection to metals.[66]

1.4.1.2 Coatings

Coatings provide corrosion protection through four possible mechanisms (**Figure 1.6**):[67] a) sacrificial, where a metallic coating (e.g., zinc) is sacrificed to protect the metal of interest (e.g., mild steel); b) barrier, where the coating provides a physical barrier to corrosive agents; c) chemical inhibitors, where chemical species are used to suppress cathodic and/or anodic reactions rates; and d) self-healing, where chemical species are used to repair damages in the coating. Coatings are usually composed of several layers such as surface pretreatment, primer, undercoat and topcoat layers (**Figure 1.7**). Each coating layer serves a specific purpose such as corrosion resistance, aesthetics (color and appearance), UV protection and mechanical properties.[68] In particular, the surface pretreatment layer serves an essential purpose in the coating system — corrosion protection.

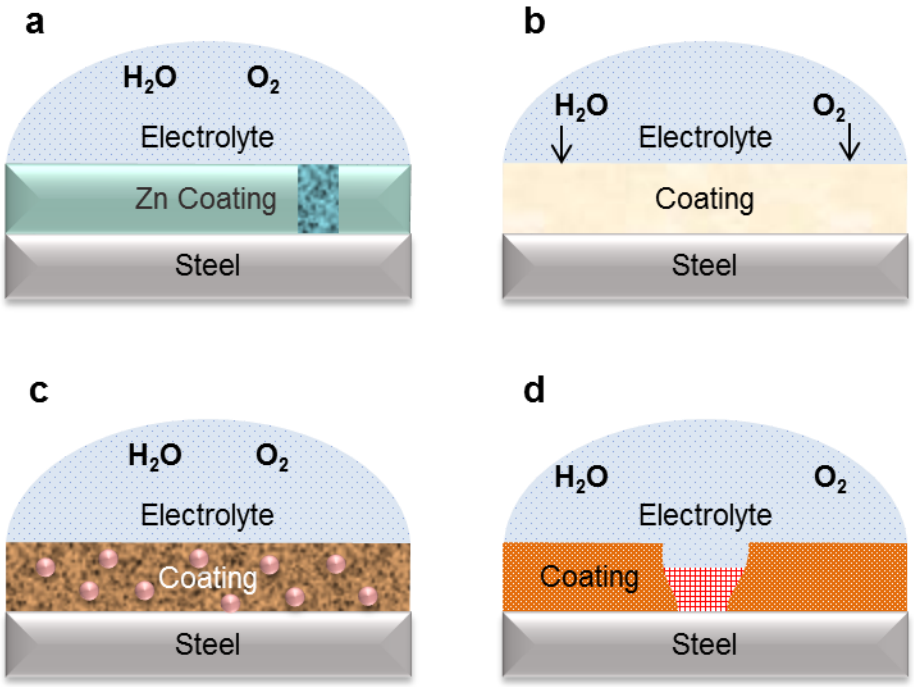

Figure 1.6 Corrosion protection mechanisms of coatings: a) sacrificial, b) barrier, c) chemical inhibitors, and d) self-healing.

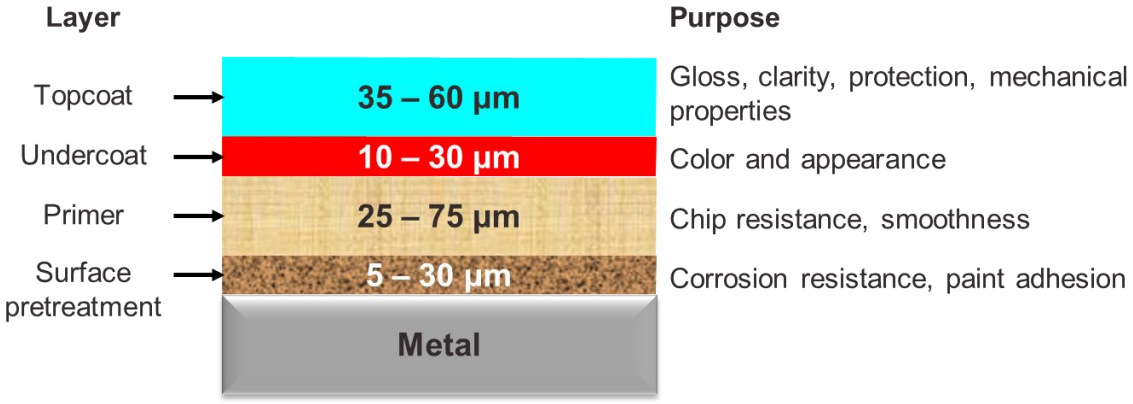

Figure 1.7 Usual coating layered structure (coating system).

Industries (e.g., aerospace, military) desire environment-friendly coatings capable of providing long-term corrosion protection under diverse environmental conditions. For over 90 years, long-term corrosion resistance — for products containing metals such as aluminum alloys and steel — has been provided through the use of chromium conversion coatings (CCCs) — well-known surface pretreatment coatings. CCCs provide excellent long-term corrosion protection due to their chemistry, barrier properties, and self-healing capabilities (**Figure 1.8**).[67, 69] However, CCCs' chromium VI-based chemistry makes them non-environment-friendly and a threat to human health and safety.[70, 71] Consequently, industry and researchers are exploring potential environment-friendly coating solutions including LbL assembled films.[67]

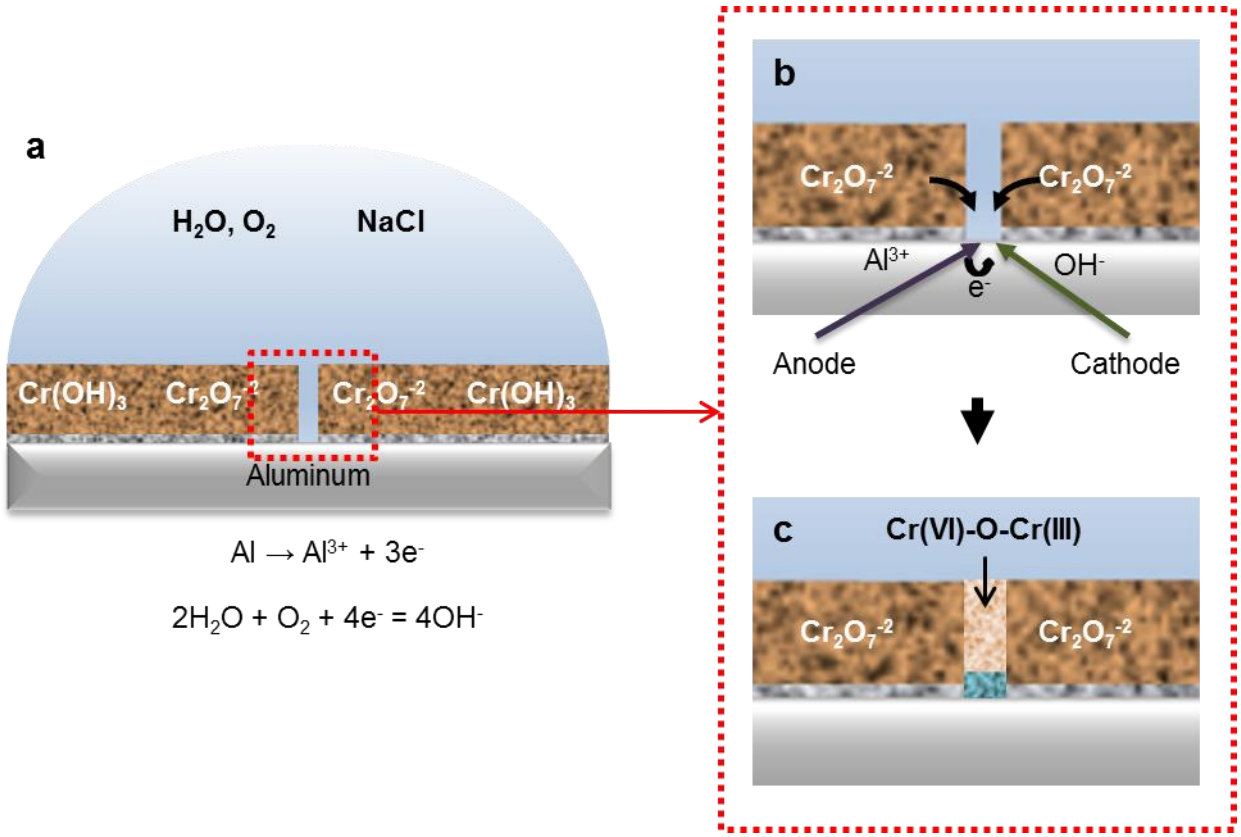

Figure 1.8 CCCs' anticorrosion mechanism. Barrier mechanism: Cr(III) hydroxide insoluble coating. Corrosion inhibitors mechanism: Soluble Cr(VI) corrosion inhibitor species. Self-healing mechanism: Formation of a Cr(VI)-O-Cr(III) mixed oxide. a) Scratch or defect on the CCC coated metal. b) Cr(VI) species are released. c) CCC self-heals through the reversible formation of a Cr(VI)-O-Cr(III) mixed oxide.

1.4.1.3 PEMs for Corrosion Protection

1.4.1.3.1 PEMs – Coatings

LbL assembly techniques can be used to design PEM coatings that provide corrosion protection through a combination of corrosion mechanisms: 1) barrier, 2) self-healing, and 3) corrosion inhibitors.[72-75] Andreeva's group, for example, studied PEMs with: a) self-healing;[76] and b) self-healing and corrosion inhibitors.[77] PEMs with barrier properties have been explored by others.[10, 78-80]

In 2008, Andreeva et al., studied a PEM coating made from a strong-weak PE couple (PSS and PEI),[77] which provided corrosion protection to an aluminum alloy through self-healing. In this PEM coating, PSS provided good adhesion to the metal, while PEI provided surface buffering — neutralizing OH^- ions produced during the corrosion process. Surface buffering resulted in swelling of the PEM coating — due to water formation — which enhanced polymer chains mobility, leading to self-healing of the PEM coating in the corrosive crack.

PEM coatings providing corrosion protection through combined mechanisms such as self-healing and corrosion inhibitors have also been studied. Andreeva's group, for example, studied the release of 8-hydroxyquinoline (8HQ) — an environment-friendly corrosion inhibitor — in a PSS/PEI/8HQ PEM coating.[77] Andreeva et al.,[81] also studied the corrosion protection provided to an aluminum alloy substrate by PEM coatings made from a combination of weak-weak, strong-weak, and strong–strong PEs, as well as corrosion inhibitors release in a PEM matrix (**Figure 1.9**). Interestingly, self-healing was observed only in PEM coatings containing at least one weak PE. Most importantly, this self-healing mechanism has been observed in other PEM coatings made from weak-weak and weak-strong PEs, under stimuli such as humidity/water, pH, and ionic strength.[75]

Finally, PEM coatings that provide a barrier corrosion protection mechanism using nanoparticles (e.g., clay) have been studied.[10, 78] Kotov's group,[79, 80] for example, studied a PEM coating made from PDDA/PAA/PDDA/clay quadlayers,[80] where clay played an important role due to its excellent barrier properties.[64, 80]

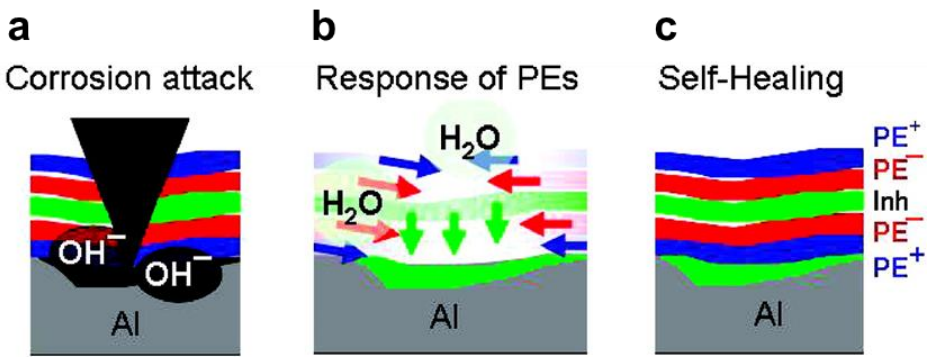

Figure 1.9 Corrosion protection mechanism provided by PEM coatings. a) Corrosion attack causing an increase in pH. b) PEs response to pH change: surface buffering. c) Self-healing due to PE chains relaxation and corrosion inhibitors release. Reprinted with permission from [81]. Copyright 2010 American Chemical Society.

1.4.1.3.2 PEMs – Corrosion Inhibitors Carriers

PEM coatings can be used on nanoreservoirs and microcapsules to aid with controlled corrosion inhibitors release under the right stimuli (e.g., pH).[82-85] Skorb et al.,[82] for example, used LbL assembly to create a shell around SiO_2 containers loaded with a corrosion inhibitor (2-(benzothiazol-2-ylsulfanyl)-succinic acid) in order to prevent its spontaneous release. At pH neutral the PEM shell remained intact, but at pH 10.1 the shell broke down releasing the corrosion inhibitor species (**Figure 1.10**).

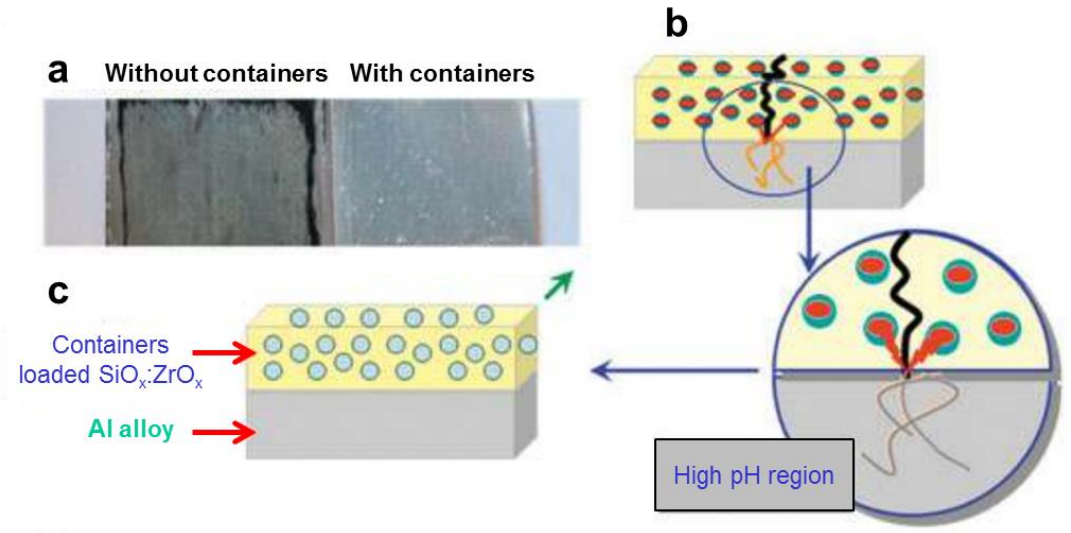

Figure 1.10 Sol-gel silica-zirconia hydride matrix incorporated with corrosion inhibitor-loaded nanocontainers. a) Images of coated substrate (aluminum alloy) after corrosion testing, with and without nanocontainers. b) Corrosion inhibitors release due to a pH change. c) Self-healed coating. Adapted with permission from [82]. Copyright © 2009 WILEY-VCH Verlag GmbH & Co. KGaA, Weinheim.

Regarding microcapsules, Leal et al.,[83] studied stimuli–responsive linseed oil-filled poly(urea-formaldehyde) microcapsules coated with a PEI/PSS/benzotriazole/PSS/PEI PEM coating. These stimuli–responsive microcapsules responded to two stimuli: pH and mechanical stress (**Figure 1.11**). Benzotriazole was released due to the pH sensitivity of the PEM coating, and linseed oil was released when a defect was induced in the coating. Thus, addition of these macrocapsules in an epoxy coating resulted in significant corrosion protection enhancement.

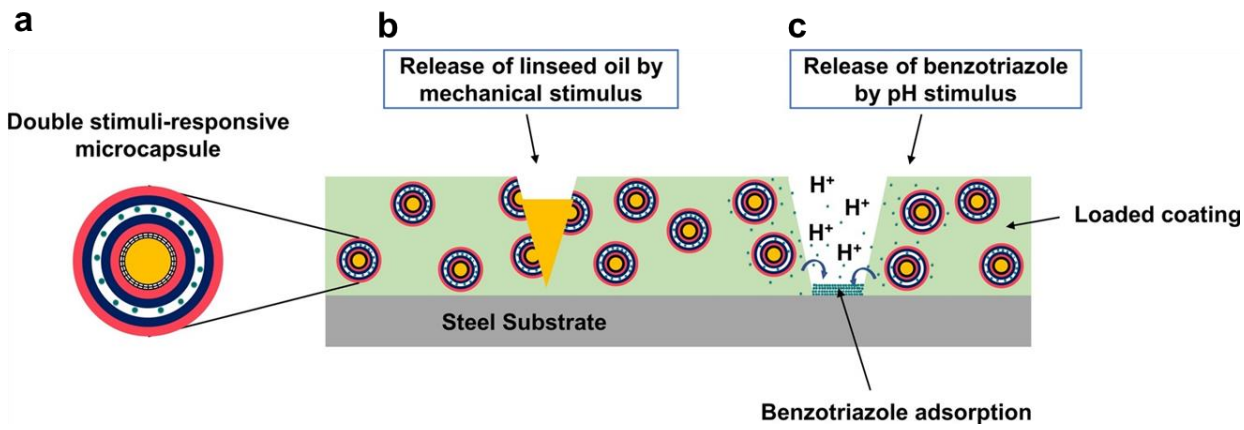

Figure 1.11 a) Double stimuli-responsive linseed oil/PEI/PSS/benzotriazole/PSS/PEI microcapsule. b-c) Release of linseed oil and benzotriazole by mechanical and pH stimuli, respectively. Reprinted from [83]. Copyright 2018, with permission from Elsevier.

1.4.2 Mechanical Properties of PECs and PEMs

PECs and PEMs morphology depend on factors — such as pH, ionic strength, and water content — that can be controlled during their preparation or post-treatment. Therefore, effects of pH, salt, and water in PECs and PEMs morphology and consequently their properties have been studied.

pH is an important factor in the morphology (stoichiometry) as well as thermal and mechanical properties of PECs made from weak PEs.[2] pH modifies weak PEs charge density (**Figure 1.12**), controlling the strength of electrostatic interactions.[2, 34] Zhang et al.,[34] and Reisch et al.,[2] for example, studied the morphology and properties of PECs made from weak PEs (PAH and PAA). Zhang showed that PECs stoichiometry — PAH:PAA ratio — is determined by the pH of the PE solutions, where higher pH values (7 – 9) resulted in quasistoichiometric PECs — PAH:PAA ratio ~ 1:1.[34] Most importantly, Zhang also showed the effects of pH and water in PAH/PAA PECs thermal transition, where increasing pH and increasing water content,

increases and decreases the PECs thermal transition temperature, respectively. Additionally, Reisch showed that pH doping changes PECs morphology, directly affecting their mechanical properties, where the closer the PAH:PAA ratio is to 1:1 — stoichiometric complex — the stiffer the PEC becomes.[2, 27]

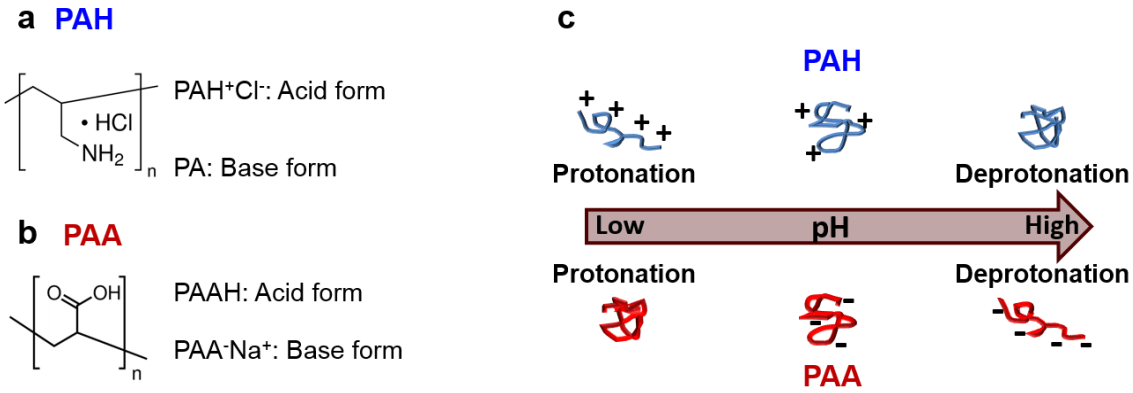

Figure 1.12 a) Poly(allylamine hydrochloride) chemical structure. b) Polyacrylic acid chemical structure. c) Effect of pH on weak PEs charge density. Adapted from [86]. Copyright 2008, with permission from Elsevier.

Salt influences the morphology as well as thermal and mechanical properties of PECs made from strong or weak PEs — salt facilitates PECs plasticization, but water is essential for it. [4, 27, 34, 87] In 2011, Zhang et al.,[88] studied the glass transition temperature of nearly dry ionically assembled PEO complexes as a function of salt concentration. Zhang showed that T_g increased with increasing salt concentration (**Figure 1.13a**), where salt acted as a hardener due to insufficient water content in the complex.[88] In 2012, Hariri et al.,[89] studied the effect of water content on PDADMA/PSS PEMs modulus, where a decrease in the PEC modulus was evidenced with increasing water content (**Figure 1.13b**). During the same year, Shamoun et al.,[90] studied the

modulus of PSS/PDADMA PECs immersed in salt solutions as a function of salt concentration. Shamoun showed that PECs modulus decreased with increasing salt concentration (**Figure 1.13c**), where salt acted as a plasticizer. Later in 2017, Zhang et al.,[33] systematically studied salt concentration effects in the thermal behavior of partially hydrated PDADMA/PSS PEMs. Zhang found that salt acts as a plasticizer — weakening ion pairing — or a hardener — immobilizing the water molecules — depending on the PEM hydration level (**Figure 1.13d**). Thus, salt also influences whether a hydrated PEC is glassy — moduli ~ 10^9 Pa — or rubbery — moduli ~ 10^6 Pa.[31, 87, 91, 92]

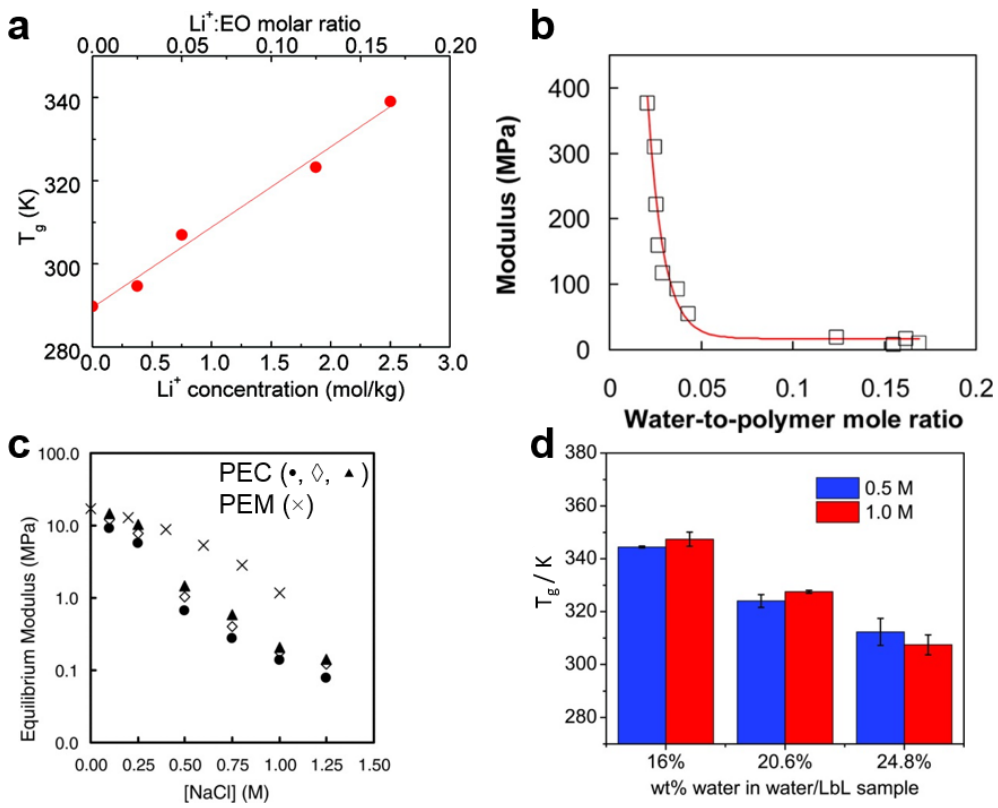

Figure 1.13 a) T_g of nearly dry ionically assembled PEO complexes as a function of salt concentration. T_g increases with lithium salt concentration due to insufficient water content in the complex. Reprinted with permission from [88]. Copyright 2011 American Chemical Society. b) PDADMA/PSS PEMs equilibrium elastic modulus as a function of water mole fraction in the polymer matrix. Modulus decreases with increasing water content in the PEM. Reprinted with permission from [89]. Copyright 2012 American Chemical Society. c) Equilibrium modulus of PDADMA/PSS PECs immersed in salt solutions. Modulus decreases with increasing salt concentration. Reprinted with permission from [90]. Copyright © 2012 WILEY-VCH Verlag GmbH & Co. KGaA, Weinheim. d) PDADMA/PSS PEMs T_g as a function of salt concentration and water content. T_g is significantly affected by water content in the PEM, while the effect of salt concentration on the T_g is insignificant.[33] Water determines plasticization response and material properties. Adapted with permission from [33]. Copyright 2017 American Chemical Society.

Water is essential. Water acts as a plasticizing agent relaxing the polymer chains within the PEC. Increasing the water content in PECs causes an increase in volume — structural rearrangement — and a decrease in both the PECs thermal transition temperature and moduli.[27, 33] PECs and PEMs are brittle when dry, and rubbery when fully hydrated. Although water has

proven to be critical for plasticization and its effects in PECs and PEMs thermal behavior have been studied, not much work has been devoted to systematically study PECs and PEMs mechanical behavior as a function of water content. **Table 1.1** shows that most studies addressing PECs and PEMs mechanical behavior have been done in PEC coacervates (gel-like morphology) and in wet PECs. This is because studying mechanical properties of PECs while immersed in aqueous solutions is more convenient.[27] Thus, only one article where PEMs mechanical behavior was systematically studied as a function of water content was found and is discussed below.

Table 1.1 Studies addressing PECs and PEMs mechanical behavior (2005 - 2018)

Ref.	Year	PEM or PEC / Materials	Test conditions / Technique	Purpose of the study	Conclusions
[93]	2005	PEM capsules PDADMA/PSS	Wet (Immersion in Milli-Q water). 25 – 70 ^{o}C AFM	E as a function of T	E decreases with increasing T
[92]	2005	PEM (Free standing) PEO/PAA	0 and 50% RH DMA / Tensile test	E as a function of RH	E decreases with increasing RH
[94]	2006	PEM (Free standing) PDADMA/PSS	Wet (Immersion in NaCl solution). 28 ± 1 ^{o}C Laboratory homebuilt instrument / Tensile test	E as a function of ionic strength (assembly [salt])	E decreases with increasing ionic strength
[95]	2008	PEM (On a substrate) PSS/PAH PAH/PAA	12 – 96% RH Tensile stage / SIEBIMM / Compression geometry (Buckling)	E as a function of RH, pH and chemistry	See reference
[96]	2011	PEM (On a substrate) NCF/PEI	0 and 50% RH Tensile stage / SIEBIMM / Compression geometry (Buckling)	E as a function of RH	E decreases with increasing RH
[97]	2011	PEC PDADMA/PSS	29 – 85% RH EIS	Conductivity as a function of RH. THSP	Conductivity increases with increasing RH
[90]	2012	PEC PDADMA/PSS	Wet (Immersion in NaCl solution) Tensile testing unit / Stress relaxation	E as a function of [salt]	E decreases with increasing [Salt]
[31]	2012	PEC PDADMA/PSS	Wet (Immersion in NaCl solution). 0 – 80 ^{o}C Rheometer in a parallel plate configuration / DMTA mode	G as a function of [salt] and T. TTSP, TSSP, and TTSSP	G decreases with increasing [Salt] and increasing T

Table 1.1 Continued

Ref.	Year	PEM or PEC / Materials	Test conditions	Purpose of the study	Conclusions
[89]	2012	PEC PDADMA/PSS	Wet (Immersion in a PEG-salt solution). 23 ± 1 °C AFM	E as a function of water content in the PEC	E decreases with increasing water content
[98]	2013	PEM (On a substrate) PAH/PAA	0 – 100% RH. 25 °C QCM-D	G as a function of RH	G decreases with increasing RH
[99]	2013	PEC Coacervate PAA/PDMAEMA	N/A Rheometer with a parallel cone-plate configuration	G as a function of polymer chain length and [salt]. TSSP	G decreases with increasing polymer chain length and increasing [salt]
[100]	2014	PEM (On a substrate) PAH/PSS	5 – 80% RH Room temperature NMC	E as a function of RH	E decreases with increasing RH
[54]	2014	PEC PAH/PAA	Wet (Immersion in salt solution) Rheometer with clamps / Strain to break experiments	UTS as a function of [salt]	UTS increases with [salt]
[101]	2014	PEC Coacervate PAA/PDMAEMA/PEI	N/A Nanorheometer with a parallel plate geometry	G as a function of [salt] and pH	G decreases with increasing [salt] and increasing pH
[102]	2015	PEC Coacervate PAA/PDADMA	N/A 25 °C Rheometer with a truncated cone-plate configuration	G as a function of pH and [salt]. TpHSP and TSSP	G decreases with increasing pH and increasing [salt]

Table 1.1 Continued

Ref.	Year	PEM or PEC / Materials	Test conditions	Purpose of the study	Conclusions
[103]	2015	PEC CHI/ALG	Wet (Immersion in salt solution or PBS) 37 ^{o}C Universal mechanical testing machine / Tensile test	E' as a function of ionic strength (assembly [salt])	See reference
[104]	2016	PEC CHT/CS	Wet (Immersion in salt solution) Universal mechanical testing machine / Tensile test	E as a function of [salt]	E decreases with increasing [salt]
[105]	2016	PEC PMPTC/PNaSS	Hydrogels Tensile tester / Tensile test / Room T Rheometer with a parallel plate geometry / 20 – 80 ^{o}C	E as prepared and after equilibration G as a function of T	G decreases with increasing T
[106]	2016	PEC PSS/PDDA, PAA/PEI, PAH/PAA	Room conditions Dual column tensile meter / Tensile test	E as a function of chemistry	See reference
[107]	2016	PEC BPEI/PAA	Wet (Immersion in different solutions) Tensile tester / Tensile test Rheometer with a parallel plate geometry	E and G as a function of wetting solution	See reference
[30]	2017	PEC PSS/PDADMA	Wet (Immersion in salt solution) Rheometer with a parallel plate geometry	G as a function of [salt]. TSSP	G decreases with increasing [salt]

Table 1.1 Continued

Ref.	Year	PEM or PEC / Materials	Test conditions	Purpose of the study	Conclusions
[108]	2017	PEC PAA/P-Et-P	Wet (Immersion in salt solution) Tensile tester / Tensile test Rheometer with a parallel plate geometry	E before and after healing G as a function of composition	See reference
[109]	2017	PEC PMMA/F127	Wet (Immersion in aqueous buffer solution) Rheometer with stainless steel parallel disks, and cone and disk fixtures	G as a function of T and pH. TTSP	G decreases with increasing T and increasing pH
[110]	2017	PEC Coacervate PSS/QVP	N/A Rheometer with a cone-plate geometry	G as a function of chemistry, [salt] and T. TSSP and TTSP	See reference
[111]	2017	PEC PADADMA/PSS	10 and 50% RH DMA / Compression geometry	E' as a function of T, time and RH	See reference
[112]	2017	PEC Coacervate (Hydrogel) GO/BPEI GO/LPEI Cloisite Na^+/BPEI Cloisite Na^+/LPEI	Wet (Immersion in Milli-Q water) Rheometer with a parallel plate geometry	G as a function of frequency	See reference
[113]	2018	PEC Coacervate (Hydrogel) AGC_{16}/NTS	Rheometer Rheometer with a parallel plate geometry 20 – 60 ºC	G as a function of T	G decreases with increasing T

Table 1.1 Continued

Ref.	Year	PEM or PEC / Materials	Test conditions	Purpose of the study	Conclusions
[114]	2018	PEC PDADMA/PSS	Wet (Immersion in salt solution) Rheometer with a cone-plate geometry	G as a function of T and [salt]. TTSP and TSSP	G decreases with increasing T and increasing [salt]
[115]	2018	PEC Coacervate PLK/PRE	N/A Rheometer with a cone-plate geometry	G as a function of [salt]. TSSP	G decreases with increasing [salt]
[116]	2018	PEC Coacervate PDADMA/PSS	N/A Rheometer with a parallel plate geometry	G as a function of [dye]	See reference

[Salt]: Salt concentration; [Dye]: Dye concentration

In 2008, Nolte et al.,[95] systematically measured the Young's modulus of ultrathin PEM films, assembled on a PDMS substrate, as a function of relative humidity. Nolte studied E's behavior under humid conditions as a function of both PE type and assembly pH, which affect the PEMs chemical composition and internal structure, respectively. In order to assess PEMs chemical structure effects, two different PEM systems were tested: PAH/PSS (weak-strong system) and PAH/PAA (weak-weak system). To evaluate assembly pH effects on the PEM structure, PAH/PAA PEM films were assembled at two different pH values.

Figure 1.14 shows a decrease in Young's modulus with increasing relative humidity, evidencing the plasticizing effect of water, regardless of chemistry or internal structure. E's behavior is summarized in **Table 1.2**. **Figure 1.14a** presents E's behavior for the $PAH_{3.0}/PSS_{3.0}$ system as a function of RH, where E had values of 7.60 ± 0.80 GPa and 0.93 ± 0.09 GPa for 12% RH and 96% RH, respectively.[95, 117] For a fully hydrated $PAH_{3.0}/PSS_{3.0}$ film (wet state, PEM film immersed in DI water), E = 0.59 ± 0.09 GPa.[117] A decrease in E is attributed to PE chains higher mobility in the swollen PEM film. **Figure 1.14b** presents E's behavior for the $PAH_{7.5}/PAA_{3.5}$ system as a function of RH, where E had values of 10.8 ± 1.50 GPa and 1.10 ± 0.20 GPa for 12% RH and 90% RH, respectively. Finally, **Figure 1.14c** presents E's behavior for the $PAH_{2.5}/PAA_{2.5}$ system as a function of RH, where E had values of 8.10 ± 0.90 GPa and 0.14 ± 0.15 GPa for 12% RH and 84% HR, respectively. Overall, results presented by Nolte et al.,[95] indicate that PEMs mechanical properties significantly change with water content (humidity), regardless of PEMs chemical structure and assembly conditions.

Table 1.2 E's behavior as a function of RH, chemistry and internal structure.[95]

System	**E / GPa (RH / %)**	**Swelling / %**
$PAH_{3.0}/PSS_{3.0}$	7.60 ± 0.80 (12) 0.93 ± 0.09 (96) 0.59 ± 0.09 (Fully hydrated)[117]	21 - 28 (Fully hydrated)[117]
$PAH_{7.5}/PAA_{3.5}$	10.8 ± 1.50 (12) 1.10 ± 0.20 (90)	26
$PAH_{2.5}/PAA_{2.5}$	8.10 ± 0.90 (12) 0.14 ± 0.15 (84)	46

However, it is important to point out the following: a) measurements were not performed in free-standing films, and b) temperature effects on PEMs mechanical behavior was not addressed. Young's modulus was measured on a PEM film/substrate assembly, thus the contribution of the PEM film to E was calculated through mathematical deconvolution. Fortunately, since Nolte's article, Shamoun et al.,[90] and Lutkenhaus et al.,[92] have proposed methods to prepare PECs and PEMs free standing films. Shamoun prepared PEC free standing films through extrusion and Lutkenhaus prepared PEM free standing films on low-energy surface substrates.

As described in this section, information is lacking regarding water content effects on PECs and PEMs dynamic mechanical behavior. In real life applications, materials are not always under completely dry or wet environments. Therefore, Chapter IV presents a systematic study of water content effects on PECs dynamic mechanical behavior, which provides insight regarding the behavior of these materials under real environmental conditions (e.g., temperature, and humidity (water content)).

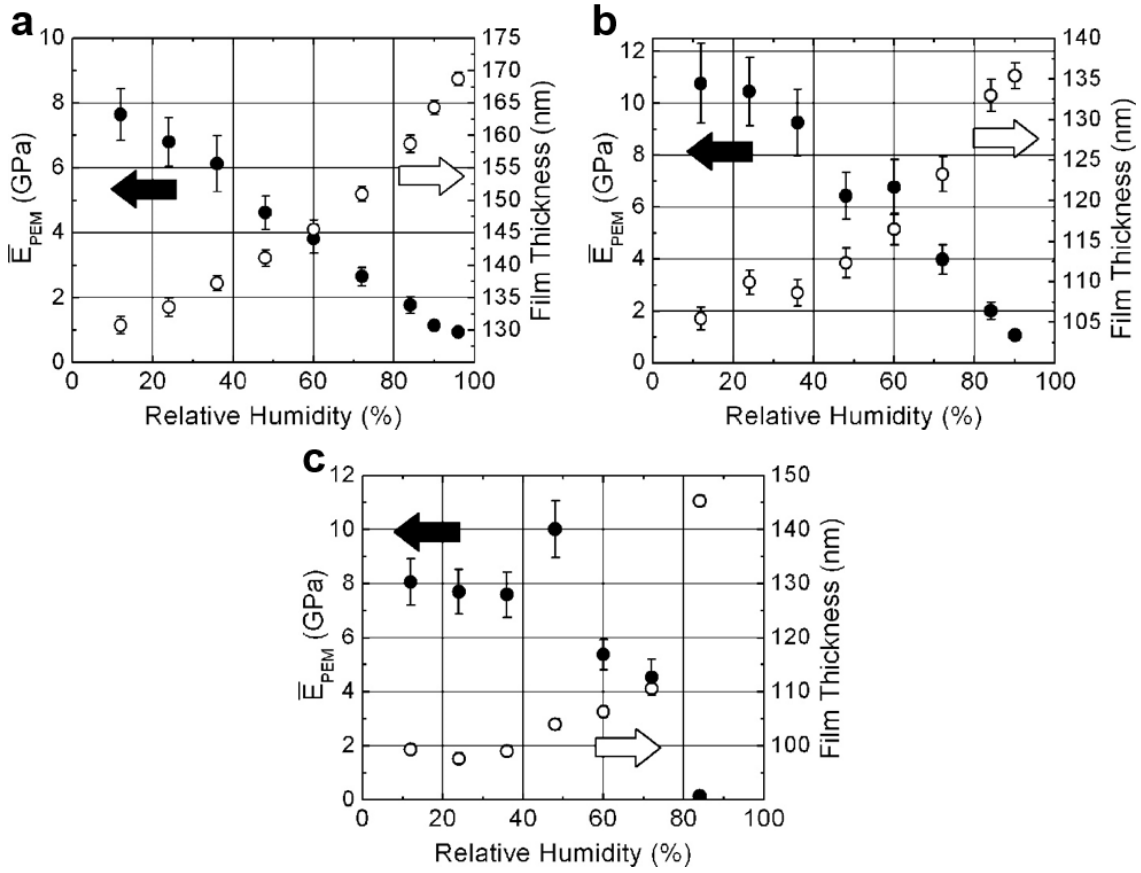

Figure 1.14 Plane strain Young's modulus (solid circles) and film thickness (hollow circles) as a function of relative humidity for PEM films. a) $PAH_{3.0}/PSS_{3.0}$, b) $PAH_{7.5}/PAA_{3.5}$, and c) $PAH_{2.5}/PAA_{2.5}$. PEM films designated as Pol^{+}_{x}/Pol^{-}_{y}, where x and y correspond to the pH of the corresponding PE solution. Adapted with permission from [95]. Copyright 2008 American Chemical Society.

CHAPTER II

SPRAY-ON POLYMER-CLAY MULTILAYERS AS A SUPERIOR ANTICORROSION METAL PRETREATMENT[1]

2.1 Introduction

Corrosion is a very expensive natural process, with predicted costs of more than $1 Trillion dollars by 2016.[118] Pretreatment coatings, applied onto a metal prior to the application of paint or other coatings, play a very important role in corrosion inhibition. Hexavalent chromium conversion coatings, commonly used as a pretreatment layer for aluminum metal, is now considered harmful,[70, 71, 119, 120] and new chromate-free pretreatments are of intense interest. These alternatives should be environmentally friendly, be scalable, and provide basic corrosion protection similar or beyond that of hexavalent chromium.[121-123] Polymer-clay nanocomposites[124, 125] are of interest as chromate-free pretreatments for their excellent barrier properties,[43, 126, 127] in which the diffusion of corrosion-causing agents is blocked or hindered.[128-131]

The corrosion of aluminum alloys is complex, thus presenting several opportunities to prevent the corrosion cycle, either by chemical or by barrier methods. When aluminum alloy 2024-T3 (AA2024-T3) is in contact with a naturally aerated NaCl solution, Al-Cu-Mg intermetallic particles existing in the alloy initially behave anodically with respect to the aluminum matrix,

[1] Modified and reprinted with permission from John Wiley and Sons. "Spray-On Polymer–Clay Multilayers as a Superior Anticorrosion Metal Pretreatment" by Pilar C. Suarez-Martinez, Jerome Robinson, Hyosung An, Robert C. Nahas, Douglas Cinoman, Jodie L. Lutkenhaus. Macromol. Mater. Eng. 2017, 302, 1600552.

allowing the rapid oxidation of Mg and Al.[132] The corresponding reduction reactions (reduction of water and/or oxygen) generate hydroxide ions, which cause an increase in the local pH. When the local pH exceeds the equilibrium pH of the aluminum oxide layer (pH 9), this layer dissolves allowing further dissolution of the aluminum matrix in order to form a new oxide layer; this process is also known as "cathodic corrosion". At later exposure times, only the copper in the intermetallic particle is left, now behaving cathodically with respect to the aluminum matrix and thus promoting its dissolution ($Al \rightarrow Al^{3+} + 3e^-$). Another type of intermetallic particle in the alloy (Al-Cu-Fe-Mn) behaves cathodically at all times (galvanic corrosion). As a pretreatment layer, hexavalent chromate-conversion coatings are formed by the destabilization of the natural oxide layer and reduction of the chromate species at the exposed aluminum surface. This coating contains a mixture of a cathodic, insoluble Cr(III) hydroxide and anodic, inhibiting, soluble, mobile Cr(VI) species. When a defect (e.g., scratch) is present, the inhibitor Cr(VI) species migrate in order to self-heal the coating by the formation of a Cr(VI)-O-Cr(III) oxide.[67, 69] This pathway represents a chemical self-healing or pore-plugging corrosion protection mechanism.

Chromate-free coatings such as phosphate,[133] lanthanide-based (Ce, Y, La, Nd, Sm, Pr),[66] potassium permanganate,[134] and group IVB metals-based conversion coatings[135-137] have been proposed. However, many of these options contain toxic components or heavy metals, which make them a potential human health and environmental issue for years to come. Organic pretreatment coatings have also been studied, such as sol-gel coatings,[138, 139] self-assembled coatings,[140, 141] conductive polymers,[142] and self-healing coatings.[141, 143] However, the synthesis of some of these coatings is time consuming and their application is not always scalable. In this regard, layer-by-layer coatings[77, 81, 144-147] are especially promising

because the coating application is a water-based process, is easily scalable by a spray-on approach,[148] and is adaptable to a wide variety of materials and substrates.

Polymer-clay nanocomposites made using layer-by-layer (LbL) assembly have demonstrated highly-ordered structures, which are favorable for corrosion protection.[79, 80] In the LbL process, a substrate of interest is exposed alternately to solutions or dispersion of species bearing complementary interactions (electrostatic, hydrogen bonding, *etc*.). Immersion-based LbL assembly is more common, yet it is not easily scalable to metals or objects of unusual shape or large surface area. For example, Kachurina employed immersion-based LbL assembly using poly(acrylic acid) (PAA), poly(diallyldimethyldiammonium chloride) PDDA and Swy-2 sodium montmorillonite to demonstrate good corrosion protection. [79] This was later translated to spray-assisted LbL assembly,[80] but the long-term corrosion properties of these LbL films remain unknown. Also there remain questions as to the relationship between structure (clay platelet orientation, composition), spray processing (pressure, distance-to-target) and corrosion protection.

Here, we address these on-going questions by investigating the long-term corrosion protection of polymer-clay nanocomposite coatings made using spray-assisted LbL assembly. The LbL coating acts as a pretreatment layer, and is comprised of branched polyethylenimine (BPEI) and natural clay (montmorillonite) — materials that possess good anticorrosion properties.[77, 128-130] Montmorillonite (MMT) is a phyllosilicate with a fairly large diameter of about 1 μm, which provides good barrier properties.[43, 126, 127] As compared to other polymer nanocomposite approaches (which have less than 10 wt% clay), the spray-on LbL approach here yields coatings of higher clay content (25 wt%), allowing for increased structural orientation of the platelets. Following rigorous corrosion testing by salt spray and electrochemical impedance spectroscopy we demonstrate superior long-term corrosion protection in a polymer-clay coating

as thin as 400 nm. Following post-mortem analysis, we propose that the mechanism of corrosion protection is a combination of barrier protection and surface buffering, which leads to the formation of a beneficial protection layer of corrosion byproducts (*i.e.*, self-sealing and pore-plugging). This demonstrates that the polymer-clay LbL coating is a promising pretreatment layer because of its environmentally friendly process, scalability, and good corrosion protection.

2.2 Experimental Section

2.2.1 Materials

Linear polyethylenimine (LPEI, Mw = 25,000), and poly(acrylic acid) (PAA, Mw = 50,000, 25% aqueous solution) were purchased from Polysciences Inc. Branched polyethylenimine (BPEI, Mw ~ 25,000) was purchased from Sigma Aldrich, and Cloisite Na+ (MMT) was provided by BYK Additives Inc for research purposes. Aluminum alloy 2024-T3 (AA2024-T3) panels were provided by Axalta Coatings Systems. Silicon wafers were purchased from University Wafer.

2.2.2 Layer-by-Layer Assembly

BPEI/MMT spray-assisted LbL pretreatment coatings were deposited on silicon wafers and AA2024-T3 panels using an automated spray-assisted LbL system (Svaya Nanotechnologies) for the growth profile and corrosion testing, respectively. Silicon wafers were cleaned in basic piranha solution (H_2O:H_2O_2:NH_4OH, 5:1:1 volume ratio) at 70 ^oC for 15 min. Then, the silicon wafers were rinsed with Milli-Q water and blow-dried. AA2024-T3 panels (2 in x 2 in) were cleaned and degreased with acetone, rinsed with ethanol and Milli-Q water, sonicated in Milli-Q water for 15 min, and blow-dried. All cleaned silicon wafer pieces and AA2024-T3 were plasma treated just before LbL assembly.

LPEI and PAA solutions with concentrations of 20 mM and 5 mM (by repeat unit molar mass), correspondingly, and pH 4 were used as anchor layers to improve the coating's growth. Two layer pairs of PEI and PAA were sprayed (10 s) onto the plasma-treated substrates. Milli-Q water at pH 4 was sprayed (10 s) in between layers of LPEI and PAA as a rinse. Deposition of the PEI/PAA anchor layers was followed by alternating deposition (10 s of spraying, 1 min of air blow-drying) of BPEI and MMT solutions with a concentration of 0.05 wt% and pH 10 and 4, respectively, until achieving the desired number of layer pairs (*n*). Pressures of 25 and 30 psi were used to assemble the coatings for the growth profile. A pressure of 30 psi was used to assemble the coatings for corrosion testing. The distance between the spray nozzle and the substrate was 7.25 in. Samples were dried in a convection oven at 70 ^{o}C for 30 min.

2.2.3 Materials Characterization

The coating thickness was measured using a profilometer (P-6, KLA-Tencor). The mass of the LbL films was measured using a quartz crystal microbalance (Maxtek-RQCM, Inficon). To evaluate the surface morphology and quality of the coating, scanning electron microscopy (SEM) images were taken using a JEOL JSM-7500F field emission SEM. Samples were sputtered with 5 nm of Pt/Pd (80/20) alloy for SEM. Cross-sectional analysis was conducted using transmission electron microscopy (TEM) on the as-prepared film using 177.8 μm (7 mil) PET (polyethylene terephthalate ST505, produced by Dupont-Teijin) as a substrate. Adhesion by tape test was performed on both a pristine and a scribed (x-cut) $(BPEI/MMT)_{40}$ LbL coating. Scotch No. 810 tape and VWR general laboratory tape were used. To study the orientation of the clay platelets in the film, a BRUKER D8 X-ray diffractometer (Cu Kα, $\lambda = 1.541$ Å) was used for wide angle X-ray diffraction (WAXD). Scans were conducted at ambient conditions (25 ^{o}C and 40% RH) from $2\Theta = 3^{o}$ to 50^{o} at a rate of 0.01^{o}/s. Sample composition was determined using energy dispersive

spectroscopy (EDS) and corroborated using an Omicron XPS/UPS system with Argus detector. The XPS spectra were shifted for the C 1s at 285.0 eV. The contact angle was measured using a goniometer. The coating's water uptake was measured using a potentiostat Gamry Interface 1000 following the Rapid Electrochemical Assessment of Paint (REAP) methodology.[149] Oxygen transmission rate (OTR) testing was performed by MOCON (Minneapolis, MN), on a MOCON Oxtran 2/21L Oxygen Permeability Instrument according to the ASTM D-3985. OTR was tested at 0% RH (dry conditions) using 177.8 μm PET as a substrate.

2.2.4 Electrochemical Characterization

Electrochemical impedance spectroscopy (EIS) measurements were performed at the frequency range of 10^{-2} Hz - 10^{5} Hz using a potentiostat Gamry Interface 1000. The electrolyte was 5 wt% NaCl aqueous solution in order to correlate EIS results to salt spray testing results. The coated AA2024-T3 samples were used as the working electrode, which had an exposed area of 1 cm^2 or 1.77 cm^2. A platinum cylindrical mesh was used as the counter electrode and a saturated calomel electrode (SCE) was used as the reference electrode. These measurements were performed at room temperature using a paint test cell placed in a Faraday cage. Before impedance testing, samples were left in contact with the 5 wt% NaCl solution for 30 minutes during which the open circuit potential (OCP) was measured. A BPEI/PAA LbL coating made of 8 layer pairs was used as a control. Samples were tested in triplicates for 40 days. Experimental data obtained from the EIS test was fitted with the Zview software. A representative measurement was chosen for the Bode, Nyquist, and phase angle plots.

2.2.5 Salt Spray Testing ASTM B117

Samples were placed in a fog chamber and exposed for 7 days (168 hours) to a 5 wt% NaCl solution at 35 ^{o}C. A scribed line of 3-3.5 cm of length was made through the coating to expose the underlying metal. Tests were performed by Axalta Coating Systems.

2.3 Results and Discussion

Spray-assisted LbL assembly of polymer and clay presents a unique challenge because clay platelets are anisotropic nanomaterials that must translate, rotate, and diffuse as they approach the substrate surface in a favorable orientation for adsorption. To explore this issue, we examined pH and spraying pressure as parameters for achieving robust film growth and uniform coverage.

Negatively charged MMT and positively BPEI were alternately sprayed from aqueous solutions onto a substrate (silicon, AA2024-T3), **Figure 2.1**. Each cycle of BPEI/MMT deposition is denoted as a "layer pair", and the assembly is denoted as $(BPEI/MMT)_n$ where *n* is the number of layer pairs. Based on prior reports,[43, 127] the pH of the BPEI and MMT solutions (pH 10 and 4, respectively) were purposefully chosen in order to obtain higher adsorption of each component and consequently higher thickness per deposited layer pair. At pH 10, BPEI is partially charged, allowing more mass to be deposited onto the previously deposited layer of negatively charged MMT. The pH chosen for the MMT solution was 4 so as to increase the charge density of the previously deposited BPEI layer and therefore enhance the deposition of MMT platelets.

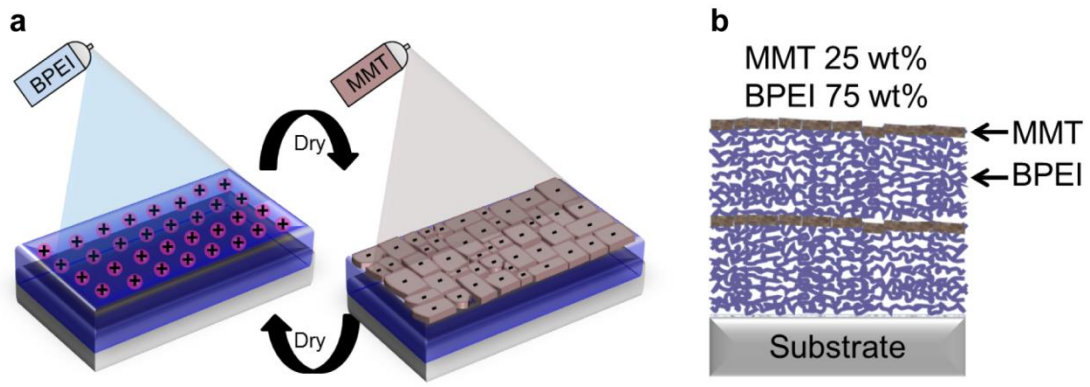

Figure 2.1 a) Spray-assisted layer-by-layer assembly of positively charged BPEI and negatively charged MMT onto a substrate. b) BPEI/MMT LbL film (25 wt% MMT and 75 wt% BPEI). Reprinted with permission from John Wiley and Sons.

Figure 2.2a shows the thickness of the BPEI/MMT coating as a function of layer pairs (*n*) measured using profilometry for two different spraying pressures. Both exhibited characteristic linear growth, where the thickness per layer pair was taken as the calculated slopes, 8.2 and 10.5 nm for pressures of 25 and 30 psi, correspondently. This difference probably results from the wetted layer at the substrate, which is thinner for higher spraying pressures, leading to a shorter diffusion path and enhanced adsorption. The smoothness of the film was also calculated using profilometry where the root-mean-square (rms) roughness for a film with $n = 40$ was 180 nm (less than half the film's thickness). The spraying pressure of 30 psi was chosen for further study because of the higher layer pair thickness. The mass of the BPEI/MMT LbL film was measured using a quartz crystal microbalance where the clay (MMT) content of the film was calculated to be 25 wt%.

Figure 2.2b shows a TEM cross-section of the BPEI/MMT coating on a PET plastic substrate. The red box outlines the LbL coating, where the dark regions are a result of the clay platelets. The clay platelets appear to generally orient parallel to one another. Spray-assisted LbL

assembly was next successfully conducted on aluminum alloy (AA2024-T3). **Figure 2.2c-d** shows SEM images of the coating at different magnifications, demonstrating uniform deposition of the coating onto the underlying alloy. No major pinholes or defects were visible. The vertical striations in **Figure 2.2c** reflect the underlying surface morphology of the AA2024-T3 surface. Additionally, adhesion of the as prepared $(BPEI/MMT)_{40}$ LbL film to the AA2024-T3 substrate was evaluated through a tape test, where both a pristine and a scribed coating were investigated (**Movie 2.1,** see supplemental files). This test demonstrates the good adhesiveness of the $(BPEI/MMT)_{40}$ LbL film to the substrate.

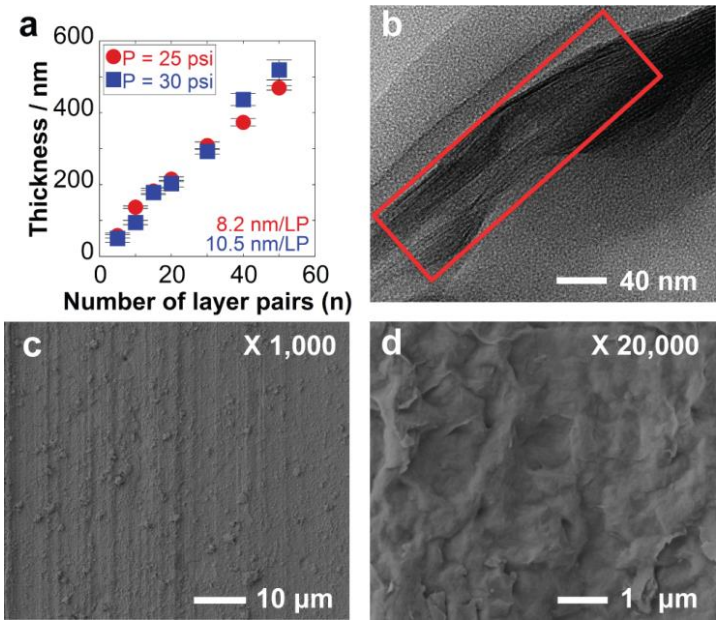

Figure 2.2 a) Thickness of a $(BPEI/MMT)_n$ layer-by-layer coating on silicon wafer as a function of the number of layer pairs for spraying pressures of 25 and 30 psi. Each data point represents the average of 5 profilometry measurements. b) TEM cross-sectional image and (c-d) SEM images of the as-prepared $(BPEI/MMT)_{40}$ coating before corrosion testing. These demonstrate linear growth, conformal coating, and stacking of the clay platelets. Reprinted with permission from John Wiley and Sons.

To further investigate the structure of the film, wide angle X-ray diffraction (WAXD) was performed on a $(BPEI/MMT)_{100}$ assembled on glass. As observed in **Figure 2.3a**, this film exhibited a very distinct peak at 6.3°, attributed to a basal (d_{001}) spacing of 14.0 Å. This is similar to previous studies of PEI/Laponite/poly(ethyleneoxide) thin films.[21] Two other peaks at 19.5° and 25.4° show spacings of 4.5 Å and 3.5 Å, respectively, suggesting that several clay platelet layers are deposited per clay deposition step.

The orientation of the clay platelets was explored using WAXD with tilt where 2θ was fixed at 6.3°, **Figure 2.3b**. The maximum intensity was at a tilt angle of φ = 0, which confirmed that clay platelets were preferentially oriented parallel to the substrate. This was corroborated by calculating the Herman's orientation parameter (f)[150] in order to quantify the degree of orientation. f ranges from -0.5 to 1, depending on whether the clay platelets are oriented perpendicular or parallel to the substrate respectively. An f-value of zero indicates random orientation. Here, we calculated an f-value of 0.31, meaning that the clay platelets in the LbL assembly have a preferential orientation parallel to the substrate.

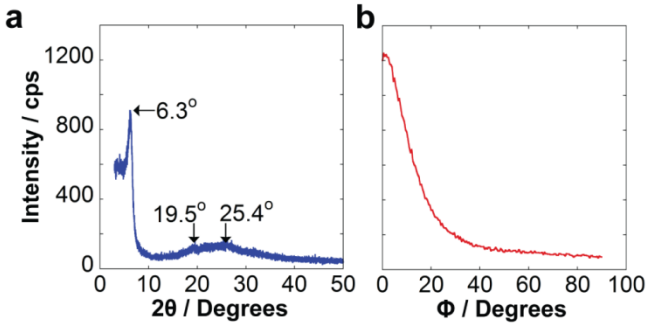

Figure 2.3 a) 2-Theta pattern for a $(BPEI/MMT)_{100}$ coating. b) WAXD with tilting where 2θ was fixed at 6.3°. The Herman's orientation parameter was measured from (b) as 0.31, indicating preferential alignment of the clay platelets parallel to the substrate. Reprinted with permission from John Wiley and Sons.

In order to assess the performance of the layer-by-layer coating, $(BPEI/MMT)_n$, coatings with 10, 20, 30 and 40 layer pairs and the bare alloy were exposed to 5 wt% NaCl at 35 ^oC for 168 hours of salt spray testing. The digital images in **Figure 2.4** show that corrosion resistance improves and fewer corrosion pits result as the number of layer pairs increases. From this test it was established that the coating composed of 40 layer pairs was the minimum number to achieve satisfactory corrosion resistance. Thicker films may perhaps exhibit better corrosion resistance, but this comes at the cost of processing time.

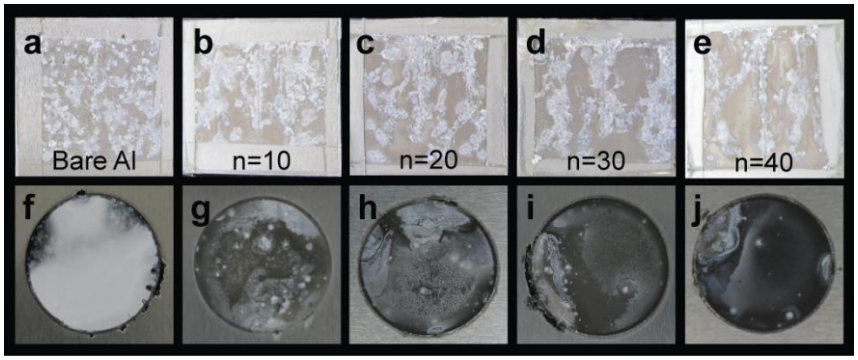

Figure 2.4 (a-e) Samples exposed to 7d (168h) of salt spray exposure (5 wt% NaCl at 35°C). (f-j) Images taken after 50 days of EIS testing for samples of corresponding composition. The composition with 40 layer pairs demonstrated the least pitting as compared to other samples investigated. Reprinted with permission from John Wiley and Sons.

Electrochemical impedance spectroscopy was used to evaluate the corrosion resistance of aluminum alloy coated with $(BPEI/MMT)_{40}$ over 40 days of exposure to 5 wt% NaCl. The Nyquist and Bode plots (**Figure 2.5a-b**) show that the impedance increases with time and stabilizes after 13 days. This behavior is better visualized in **Figure 2.5c**, where the magnitude of the complex impedance |Z| is plotted as a function of time. After 40 days, the impedance of the coated aluminum is ~ 800 times higher than that of the original bare aluminum alloy on day 1 (taken at a frequency of 0.01 Hz). This dramatic difference in impedance shows that the polymer-clay coating provides

remarkable corrosion protection, considering that it is only 400 nm thick. This behavior is characteristic of 'self-healing' and 'defect self-plugging', arising from surface buffering provided by BPEI, the barrier provided by the MMT, and corrosion products that beneficially passivate the surface.[77, 151, 152]

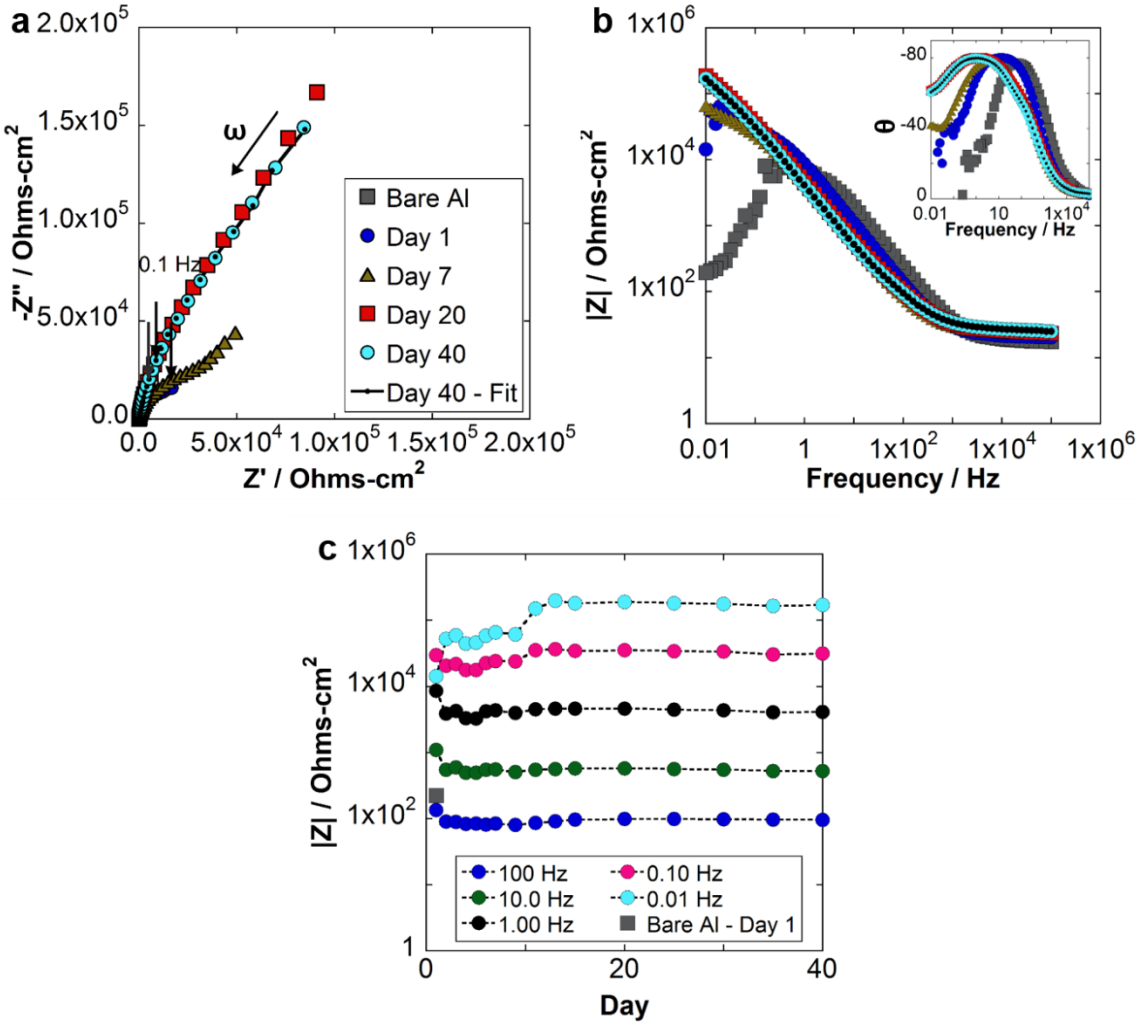

Figure 2.5 Aluminum alloy 2024-T3 coated with $(BPEI/MMT)_{40}$. a) Nyquist plot, b) Bode plot, (Inset: Phase angle plot), and c) impedance for frequencies of 0.01, 0.1, 1, 10, and 100 Hz as a function of time. The decrease and then recovery and stabilization of |Z| with time is suggestive of self-healing of defects and pore-plugging. Reprinted with permission from John Wiley and Sons.

The impedance response was modeled using the equivalent circuit shown in **Figure 2.6a** to capture physical processes occurring during corrosion.[79, 80, 153-155] Of particular note is the pore resistance (R_{pore}), coating capacitance (CPE_c), polarization resistance (R_p), double layer capacitance (CPE_{dl}) and a Warburg diffusion element (W, used at later exposure times). **Figure 2.6b** shows R_{pore} with time, which is considered an indicator of the integrity of the coating. The coating with n = 40 shows a decrease in R_{pore} after 9 days of exposure to the electrolyte solution, which is associated with the formation of defects. For n = 10, 20 and 30, this occurs earlier at or before 7 days. The coating with n = 40 shows an increase in R_{pore} after day 9, which suggests the beginning of a 'self-healing' cycle. The LbL film's conductivity was estimated from R_{pore} at early times as $\sigma = 9 \times 10^{-10}$ S-cm^{-1}, which demonstrates the generally insulating nature of the coating. On the other hand, **Figure 2.6c** shows the polarization resistance R_p, which is inversely proportional to the rate of the corrosion process; for the coating with 40 layer pairs, R_p remains steady and bears the highest value on the order of 10^5 ohms-cm^2. For the thinner coatings, R_p values fluctuated throughout most of the testing period probably as a result of pit development and formation/dissolution of corrosion products. In sum, the impedance analysis suggests that small defects in the coating appear in the first few days, followed by pit development, and the formation of a beneficial layer of corrosion products that stabilizes and delays the diffusion of corrosive agents towards the alloy or corrosion products away from it, thus preventing further corrosion long-term (i.e., the plugging effect).

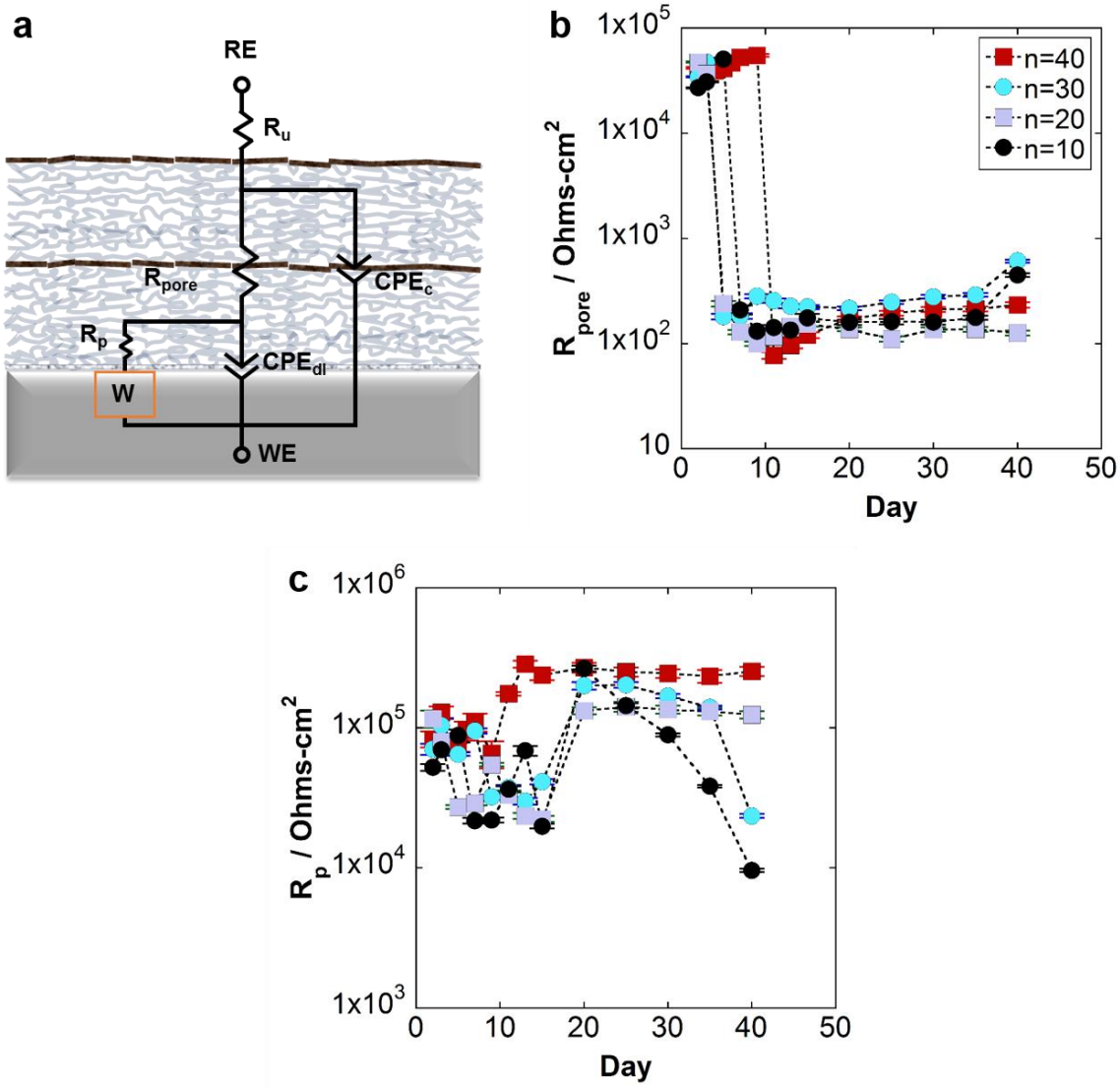

Figure 2.6 Impedance results for AA 2024-T3 coated with $(BPEI/MMT)_n$, n = 10, 20, 30, and 40 modeled by the equivalent circuit shown in (a). The equivalent circuit model includes R_u: Resistance of the electrolyte, CPE_c: Coating capacitance, R_{pore}: Resistance of the coating, CPE_{dl}: Double layer capacitance, R_p: Polarization resistance or charge transfer resistance, and W: Warburg element. b) Pore resistance R_{pore} and c) polarization resistance R_p with time. Reprinted with permission from John Wiley and Sons.

Physically, the superior corrosion protection arises from two mechanisms associated with the MMT platelets and BPEI. MMT platelets provide outstanding barrier protection[156, 157] in that they physically delay the transport of oxygen and ions through the coating towards the

underlying alloy. The good corrosion barrier properties are supported by images of the coated aluminum alloy surface after electrochemical impedance spectroscopy (EIS) testing, **Figure 2.4 f-j**. Bare aluminum alloy exhibited substantial white corrosion products at the surface, whereas the coated samples did not. SEM images of these samples post-testing show some evidence of polymer dissolution at the surface, while revealing stacks of clay aggregates, **Figure 2.7**. There is also a possible secondary corrosion resistance mechanism arising from BPEI, a weak polyelectrolyte that possibly contributes to the self-healing of the aluminum alloy/LbL coating system due to a surface-buffering effect, acting as a "proton sponge".[77][81] When the corrosion process starts, Al oxidizes to Al^{+3} and H_2 as OH^- ions are produced. The positively charged amines in the BPEI structure neutralize the OH^- ions, thus hindering the corrosion process.[77] Also, BPEI can create a complex with the aluminum oxide consequently acting as a corrosion inhibitor.[77, 158]

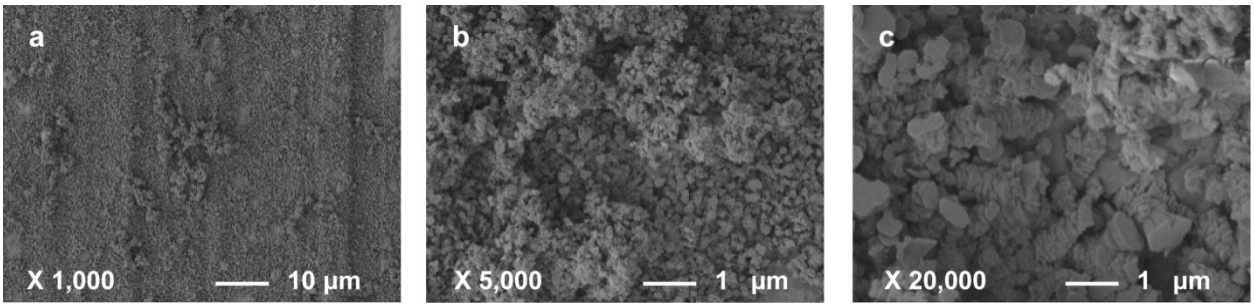

Figure 2.7 SEM images for $(BPEI/MMT)_{40}$ after 50 days of exposure to 5 wt% NaCl and electrochemical impedance spectroscopy. (a-c) Same sample at different magnifications. Reprinted with permission from John Wiley and Sons.

We also examined a control sample in which the clay was replaced with PAA to form an all-polymer $(BPEI/PAA)_{8,}$ LbL coating, **Figures 2.8 and 2.9**. The most remarkable difference is shown in **Figure 2.8**, where the BPEI/PAA film showed severe corrosion. The Nyquist plot in

Figure 2.9c shows that for the BPEI/PAA film the impedance oscillates possibly because of self-healing attempts of the aluminum alloy/LbL coating system and the continued formation and dissolution of corrosion products. When examining R_{pore} with time (not shown) a significant decrease from 1.7×10^4 to 2.1×10^1 ohms-cm^2 is observed during the first three days of exposure to the electrolyte solution. This negative control unambiguously shows that clay platelets significantly enhance the corrosion resistance of LbL coatings, probably because they block the diffusion of corrosive agents towards the alloy.

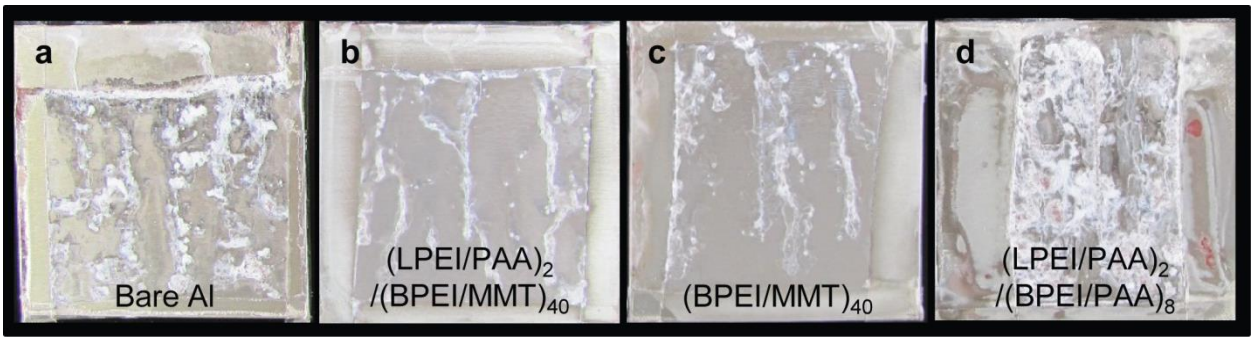

Figure 2.8 Samples exposed to 7d (168h) of salt spray exposure (ASTM B117; 5 wt% NaCl at 35°C). a) Bare AA2024-T3, b) $(LPEI/PAA)_2/(BPEI/MMT)_{40}$, c) $(BPEI/MMT)_{40}$ (no anchor layers), d) $(LPEI/PAA)_2/(BPEI/PAA)_8$. The thickness for both layer-by-layer coatings $(LPEI/PAA)_2/(BPEI/MMT)_{40}$ and $(LPEI/PAA)_2/(BPEI/PAA)_8$ was about 400 nm. Figure 2.8d shows the case for when MMT was substituted by PAA. This shows that the MMT platelets are needed for the corrosion inhibition. Reprinted with permission from John Wiley and Sons.

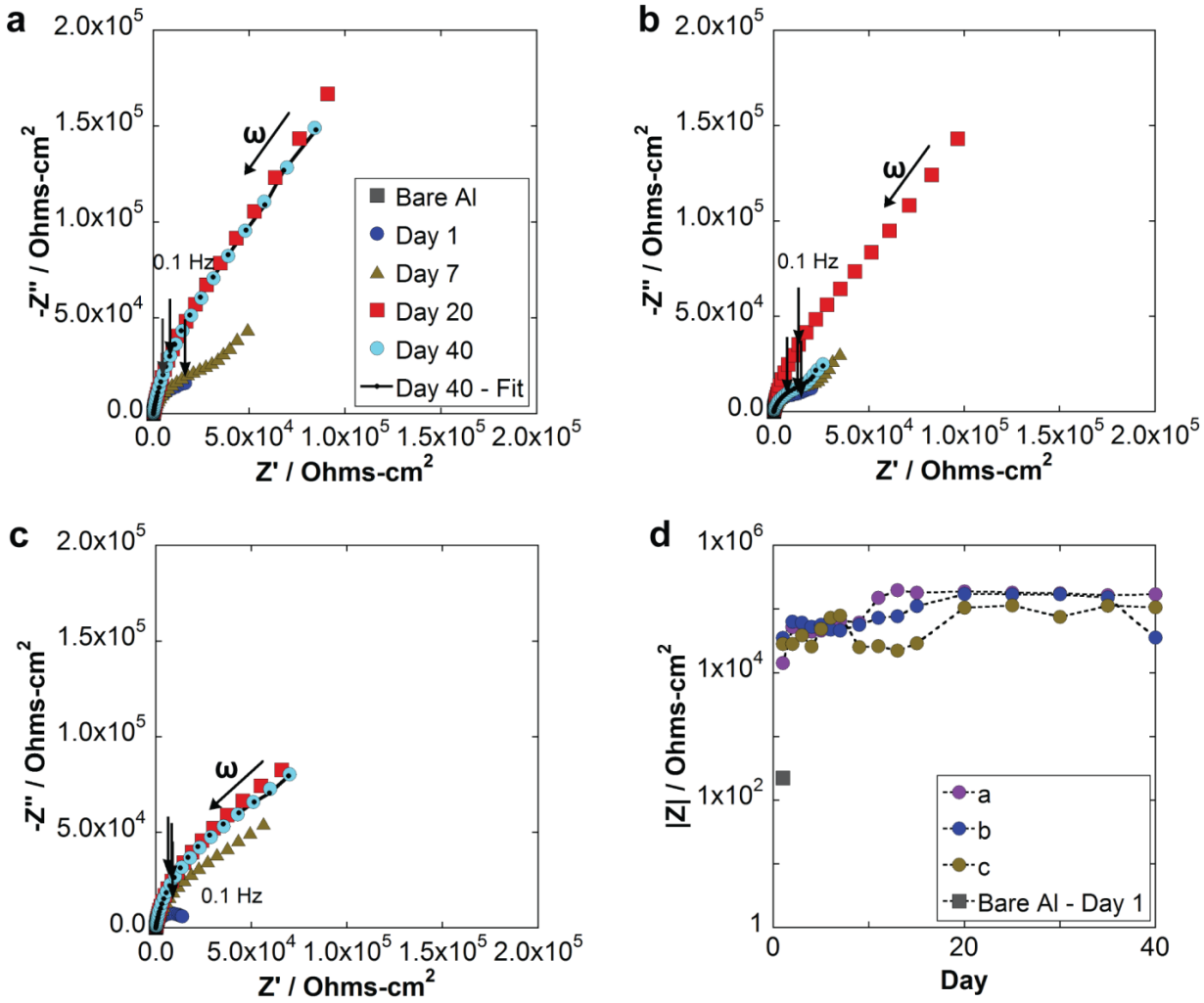

Figure 2.9 Electrochemical impedance spectroscopy of samples exposed to 5 wt% NaCl for 40 days. a) $(LPEI/PAA)_2/(BPEI/MMT)_{40}$, b) $(BPEI/MMT)_{40}$ (no anchor layers), c) $(LPEI/PAA)_2/(BPEI/PAA)_8$, d) Impedance at 0.01 Hz for samples a-c as a function of time. Reprinted with permission from John Wiley and Sons.

Energy dispersive spectroscopy (EDS) and X-ray photoelectron spectroscopy (XPS) were used to examine the composition of the $(BPEI/MMT)_{40}$ coating on aluminum alloy panels before and after corrosion testing, **Figure 2.10**. Initially, the detected elements included aluminum, oxygen, carbon, silicon, nitrogen, copper, and magnesium. These elements come from the aluminum alloy and the layer-by-layer BPEI/MMT coating. After 50 days of exposure to 5 wt%

NaCl, three areas were studied: a corrosion pit (area 1), the region near the pit (area 2), and far from the pit where no obvious defects were observed (area 3). As evidenced by the increased oxygen content, some amount of corrosion products cover the surface in all areas. Area 3, showed no presence of nitrogen after corrosion testing, which suggests that some of the BPEI dissolved at the top surface of the coating. The existence of the corrosion products on all areas is further evidence of the plugging effect that facilitates healing over corrosion defects. This is confirmed further using XPS, in which survey scans clearly show the presence of carbon, manganese, iron, oxygen, nitrogen, silicon, magnesium, and aluminum.

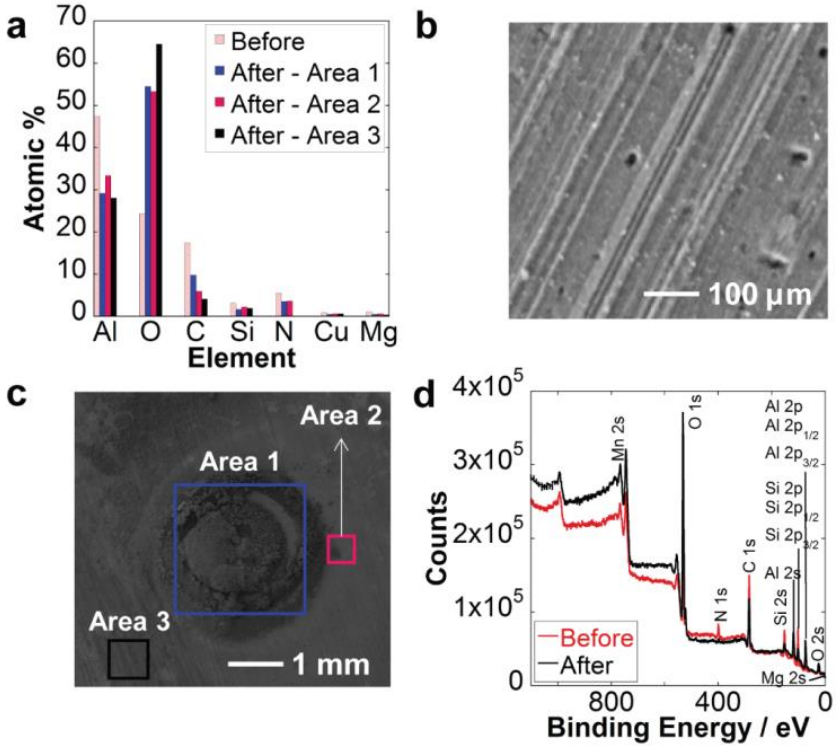

Figure 2.10 (a-c) Composition from EDS and (d) XPS survey scans of aluminum alloy panels coated with $(BPEI/MMT)_{40}$ before and after 50 days of exposure to 5 wt% NaCl. Fe, Na, and Mn < 0.15 atomic %. (b) and (c) show the coated panels used for EDS before and after the salt exposure, respectively. In (c), three areas were examined: a corrosion pit (area 1), the region near the pit (area 2), and far from the pit (area 3). The increased presence of oxygen after salt exposure shows the generation of corrosion products in all three areas. Reprinted with permission from John Wiley and Sons.

The Brasher-Kingsbury equation was used to calculate the water uptake for $(BPEI/MMT)_{40}$ as a function of its coating capacitance. By this estimate, the polymer-clay coating contains 36 v% water. Similarly, the coating exhibits moderately hydrophilic properties with advancing and receding contact angles of 54.8° and 43.1° respectively. Although water seems to penetrate into the film, it does not appear to accelerate corrosion. This is possibly due to the tortuous path afforded by the MMT clay platelets, the surface buffering effects provided by the BPEI, and the formation of a stable passivating layer of corrosion products.

To assess the barrier properties of the coatings, the oxygen transmission rate (OTR) and the oxygen permeability were examined at 0% relative humidity for bare PET and PET coated with $(BPEI/PAA)_8$ or $(BPEI/MMT)_{40}$. Both films were fabricated in order to have similar thickness (~ 400 nm). The OTR for samples $(BPEI/PAA)_8$ or $(BPEI/MMT)_{40}$ were similar, 1.310 and 1.789 cm^3/m^2-day-atm respectively, and about five times lower than the bare PET (8.6 cm^3/m^2-day-atm). This finding is consistent with other BPEI/MMT films previously reported in the literature.[43, 127] The oxygen permeability was calculated and decoupled[159] in order to obtain the individual contribution of the layer-by-layer films $(BPEI/PAA)_8$ and $(BPEI/MMT)_{40}$, 0.007 x 10^{-16} and 0.010 x 10^{-16} cm^3 (STP) cm/cm^2-s-Pa, respectively. Although both thin films present a very similar oxygen permeability, only the very good oxygen barrier properties of the $(BPEI/MMT)_{40}$ coating translate into good anticorrosion properties, as supported by the electrochemical measurements.

This combination of findings provides support for the proposed anticorrosion mechanism, where the MMT clay platelets act collectively as an outstanding barrier to the mobility of corrosive agents towards the underlying metal, while the BPEI obstructs the progress of the corrosion process through surface buffering. Thus, both the MMT and BPEI simultaneously promote the integrity of a uniform layer of corrosion products that delays the onset of new defects (plugging

effect). This combination of effects provided by the MMT, BPEI and the corrosion products layer result in a self-healing synergistic effect of the aluminum alloy/LbL coating system.

2.4 Conclusions

A highly ordered, multilayered, corrosion-blocking polymer-clay nanocomposite coating was demonstrated. The coating was deposited by spray-assisted LbL assembly, a water-based deposition technique with low environmental impact as compared to current chromium conversion coatings. The coating consisted of tightly packed layers of BPEI and MMT platelets, resulting in a conformal coating in which MMT clay platelets provided barrier protection and BPEI provided surface buffering effects. The combination of these two corrosion prevention mechanisms resulted in self-sealing defects that could withstand the harsh environment of salt spray testing (7 days a 5 wt% NaCl solution at 35 ^{o}C) and EIS testing (40 days, 5 wt% NaCl) when examined as coatings on aluminum alloy 2024-T3. Compared to other systems in the literature (bis-sulfur silane (350 nm thick film)[152], and cerium-doped sol-gels (2 μm thick film)[160]) a 400 nm thick BPEI/MMT LbL coating performs similarly by maintaining and recovering its integrity (R_{pore}) for more than 30 days without the use of any additional corrosion inhibiting species. More broadly, these results demonstrate a new type of spray-on coating consisting of polymers and clay nanoplatelets. These may have significant impact in applications extending to separations and gas barriers.

CHAPTER III

POLYMER-CLAY NANOCOMPOSITE COATINGS AS EFFICIENT, ENVIRONMENT-FRIENDLY SURFACE PRETREATMENTS FOR ALUMINUM ALLOY 2024-T3[2]

3.1 Introduction

Chromium conversion coatings (CCCs) are very effective surface pretreatments and have been used by the aerospace and military industry for decades. CCC's popularity stems from the corrosion resistance provided to most metals and alloys (e.g., steel or aluminum).[67] For example, aluminum alloy 2024-T3 with a CCC is used in aircraft due to the light weight alloy's good mechanical properties and the CCC's corrosion resistance. The CCC acts as a multifunctional coating, for which it is both an insoluble inhibiting barrier as well as a self-healing coating due to soluble chromium (VI) species.[67, 69] CCC's performance has been outweighed by many environmental and safety concerns regarding its use,[70, 71, 120, 161-163] resulting in strict regulation of CCC's use and a pressing search for CCC substitutes. Therefore, the desired CCC substitute should be environment-friendly in the long term, cost-effective, industrially scalable, and most importantly provide equal or better corrosion resistance. In this study, the surface pretreatment coatings for the corrosion protection of aluminum alloy 2024-T3 is of specific focus.

[2] Modified and reprinted with permission from Elsevier. "Polymer-Clay Nanocomposite Coatings as Efficient, Environment-Friendly Surface Pretreatments for Aluminum Alloy 2024-T3" by Pilar C. Suarez-Martinez, Jerome Robinson, Hyosung An, Robert C. Nahas, Douglas Cinoman, Jodie L. Lutkenhaus. Electrochim. Acta. 2018, 260, 73-81. Copyright © 2017 Elsevier Ltd

In consequence, new chromium-free pretreatment coatings for the aluminum alloy 2024-T3 have been studied,[66, 164] some successfully, while others still present several challenges. The corrosion process for aluminum alloy 2024-T3 is well described elsewhere.[15, 132] Briefly, the process consists of both galvanic corrosion and cathodic corrosion of the aluminum matrix. For instance, pretreatments containing heavy metals represent a potential long term pollutant;[165, 166] pretreatments employing rare earth metals involve high costs;[167] others such as sol-gels require complex and time-consuming synthesis processes;[138, 168, 169] or some pretreatments' corrosion resistance do not par with CCCs.[170]

Polymer-clay nanocomposites (PCNs) are potentially interesting as anti-corrosion surface pretreatment layers because of their outstanding barrier characteristics, which have been shown to correlate to good anticorrosion properties.[15, 79, 80, 128, 171-173] Intercalated PCNs with high clay content and a highly oriented structure promote effective gas barrier properties.[157, 174-176] Yet, it is not completely clear how these structure-property relationships might similarly influence anticorrosion properties for PCNs. There are several approaches to obtaining intercalated PCNs: *in situ* template synthesis, *in situ* intercalative polymerization, melt intercalation, layer-by-layer (LbL) assembly and solution intercalation (exfoliation-adsorption).[15, 177-179] For a versatile and scalable surface pretreatment coating, it is desired to reduce coating application time and its associated costs, but many of these methods exhibit significant disadvantages. *In situ* template synthesis may result in platelet aggregation, and the high temperatures required to synthesize the clay minerals may induce polymer degradation. *In situ* intercalative polymerization requires modified monomers to intercalate between clay platelets, limiting monomer choice. Melt intercalation involves heat to achieve polymer intercalation into the clay platelets, and performs best with organomodified clays. Layer-by-layer assembly requires long processing time (> 2h) for

thick films (> 400 nm), and clay content is not easy to control *a priori*. Out of all of these approaches, a single-step, single-application surface pretreatment is desired. To that end, solution intercalation and subsequent spraying is an attractive process.

In previous work, we presented the long-term corrosion protection of aluminum alloy 2024-T3 provided by a polymer-clay LbL coating, where branched polyethylenimine (BPEI) and montmorillonite (MMT) clay were used.[15] A self-healing synergistic effect of the aluminum alloy 2024-T3/LbL coating system was observed, where: (a) MMT clay platelets act as physical barriers for the diffusion of corrosive agents/corrosion products through the coating, (b) BPEI provides surface buffering in order to decelerate the corrosion process, and (c) the BPEI/MMT LbL coating promotes the integrity of a passivating layer formed where defects are present (plugging effect). However, the spray-assisted LbL assembly technique limits scalability and control over the film's composition. For example, it takes 2h to prepare a LbL coating 400 nm thick with a 25 wt% clay content.

Here, we report an aqueous-based, sprayable one-pot surface pretreatment for aluminum alloy 2024-T3, prepared by simply mixing BPEI and MMT. BPEI and MMT were strategically chosen due to their individual and synergistic anticorrosion properties.[15, 77, 128] The two are mixed in a solution intercalation process, enabling precise control of the polymer-clay ratio. The structure and morphology of the sprayed coating on aluminum alloy 2024-T3 was investigated, as well as the long-term corrosion performance. The composition was varied so as to understand structure-property-performance relationships. To our knowledge, this work represents one of the first demonstrations of water-based, one-pot, spray-on PCNs surface pretreatments. This is probably because of prior challenges with designing a one-pot mixture with good polymer-clay

interactions, while remaining water-stable and sprayable. Therefore, this work addresses the needs for scalable, environment-friendly corrosion protection coatings.

3.2 Experimental Section

3.2.1 Materials and Preparation of Substrates

Cloisite Na+ montmorillonite (MMT) was supplied by BYK Additives Inc for academic use. Branched polyethylenimine (BPEI) Mw ~ 25,000 g-mol^{-1} and Mw ~ 2,000,000 g-mol^{-1} were acquired from Sigma Aldrich. Aluminum alloy 2024-T3 coupons, silicon wafers, glass slides and polyethylene terephthalate ST505 (PET, 177.8 μm) were purchased from ACT Test Panel Technologies, University Wafer, VWR and Tekra, respectively. PET, silicon wafers, glass slides, and aluminum alloy 2024-T3 panels were used for transmission electron microscopy (TEM) and oxygen transmission rate (OTR), growth profile, wide angle X-ray diffraction (WAXD), and corrosion testing, correspondingly. Silicon wafers and glass slides were cleaned by immersion in basic piranha solution (H_2O:H_2O_2:NH_4OH, 5:1:1 volume ratio) at 70 ^oC for 15 min, rinsing (Milli-Q water) and drying. PET was cleaned by alternating rinsing with methanol and Milli-Q water. Polished and non-polished aluminum alloy 2024-T3 coupons were cleansed with acetone, ethanol and Milli-Q water, followed by sonication in Milli-Q water for 15 min, rinsing and drying.

3.2.2 Preparation of the BPEI-MMT One-Pot Mixture and Application of the Coating

The BPEI/MMT one-pot mixture was prepared by simple mixing of an aqueous dispersion of negatively charged MMT (1 wt%) with an aqueous solution of positively charged BPEI (1 wt%). The natural pH values of the BPEI (pH 10.9) solution and the MMT dispersion (pH 9.5) were not adjusted; the pH of the final mixture was around 11.0. Upon mixing, the solution-dispersion became opaque and the viscosity increased, evidencing affinity of the two components by electrostatic attractions. The BPEI/MMT one-pot mixture was then airbrushed (atomization air

flow rate = 18 ft^3-h^{-1} STP; 0.40 mm nozzle diameter) onto a substrate (silicon, glass, and aluminum alloy 2024-T3) held at 70-80 ^oC, **Figure 3.1**. The coating application process is shown in **Movie 3.1** (see supplemental files). Here, each BPEI/MMT nanocomposite coating is identified by the polymer-clay ratio and volume of the one-pot mixture used to make the coating. For example, $(BPEI_x/MMT_y)_v$ identifies a coating with final '*x*' wt% BPEI and '*y*' wt% MMT made by airbrushing '*v*' milliliters of a BPEI/MMT one-pot mixture with a *x:y* polymer-clay ratio. All coatings were prepared with BPEI molecular weight (Mw) 25,000 g-mol^{-1} unless otherwise stated.

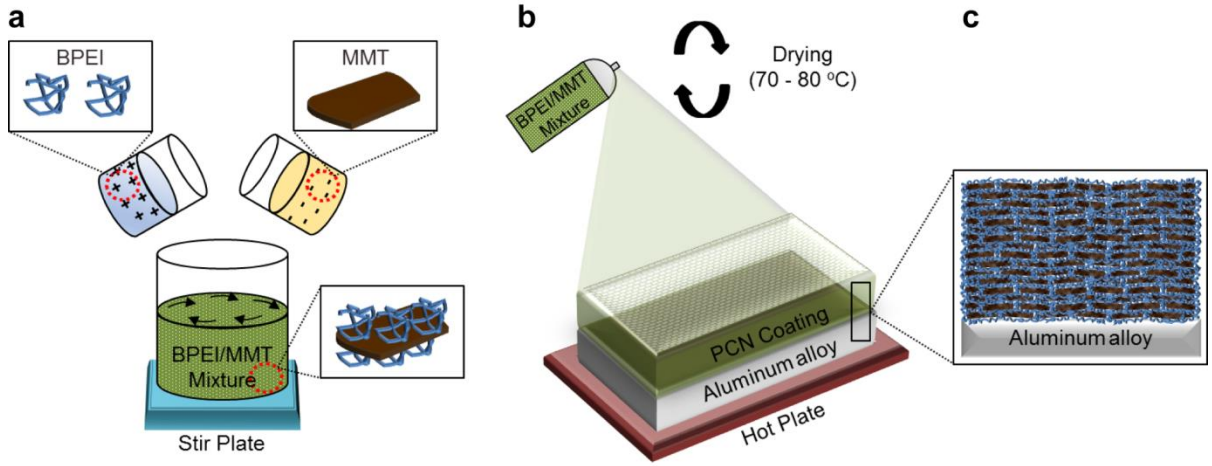

Figure 3.1 a) Preparation of the BPEI/MMT one-pot mixture by simple mixing of the two solutions and homogenization of the resulting mixture by stirring. b) Airbrushing of the BPEI/MMT one-pot mixture onto a substrate (e.g., aluminum alloy 2024-T3), where heat was used to facilitate the application process. c) BPEI/MMT polymer-clay nanocomposite (PCN) coating. Reprinted with permission from Elsevier.

3.2.3 Instrumentation

3.2.3.1 Salt Spray Testing

Salt spray testing was performed by Axalta Coating Systems during 7 d (168 h) in compliance with ASTM B117. Scribe length, 3-3.5 cm.

3.2.3.2 Electrochemical Impedance Spectroscopy

Electrochemical impedance spectroscopy (EIS) measurements were conducted with a potentiostat Gamry Interface 1000 in a frequency range of 10^{-2} Hz – 10^{5} Hz. Measurements were executed at room temperature in a three electrode configuration paint cell. The three electrode configuration included the sample as working electrode, a Pt cylindrical mesh as counter electrode, and a saturated calomel reference electrode. The tested area of the working electrode was either 1 cm^2 or 1.7 cm^2. For comparison purposes with salt spray testing, 5 wt% NaCl was chosen as the electrolyte solution. All samples were enabled to reach an equilibrium state for 30 minutes before EIS measurements, during which the open circuit potential (OCP) was measured. The EIS experimental set-up was enclosed in a Faraday cage. Zview software was used for experimental data fitting. Samples were measured in triplicates but only one sample was chosen for data representation.

All EIS measurements and salt spray testing were performed on cleaned as-received aluminum alloy 2024-T3 coupons unless otherwise stated.

3.2.3.3 Dynamic Viscosity

Dynamic viscosity (η) measurements were performed at 25 ^{o}C and 100 RPM, using an Anton Paar MCR 301 rheometer with a coaxial double gap cup and bob accessory (DG26.7-SS).

3.2.3.4 Wide Angle X-ray Diffraction

A BRUKER D8 X-ray diffractometer (Cu Kα, λ = 1.541 Å) was used for wide angle X-ray diffraction (WAXD) measurements at room conditions (25 ^{o}C and ~ 40% RH), with a 2Θ range of 3^{o} to 50^{o}, and a rate of 0.01^{o}/s.

3.2.3.5 Growth Profile

The coating thickness and roughness were measured using a profilometer P-6, KLA-Tencor. The average of 5 profilometry measurements constituted one data point.

3.2.3.6 Scanning Electron Microscopy and Transmission Electron Microscopy

A JEOL JSM-7500F field emission scanning electron microscopy (SEM) was used to capture surface and cross-sectional images of the samples. Due to the non-conductive nature of the BPEI/MMT film, samples were sputtered with 4-5 nm of Pt/Pd (80/20) alloy for SEM analysis. Cryogenic transmission electron microscopy (TEM) was used for further cross-sectional analysis of the as-prepared BPEI/MMT film.

3.2.3.7 Adhesion

Adhesion of the intact $(BPEI_{20}/MMT_{80})_3$ coating to the aluminum alloy 2024-T3 was evaluated using a tape test, where VWR general lab tape was used.

3.2.3.8 Hydrophilic-Hydrophobic and Gas Barrier Properties

The BPEI/MMT film water uptake was measured with a potentiostat Gamry Interface 1000.[149] Receding and advancing contact angles were measured using a goniometer. Oxygen transmission rate (OTR) measurements at dry conditions (0% RH, 23 ^{o}C) using an Oxtran 2/21L Oxygen Permeability Instrument (ASTM D-3985) were performed by MOCON (Minneapolis, MN).

3.2.3.9 Energy Dispersive Spectroscopy and X-ray Photoelectron Spectroscopy

Elemental analysis was performed to determine sample composition through energy dispersive spectroscopy (EDS) and verified by X-ray photoelectron spectroscopy (XPS). A JEOL JSM-7500F field emission SEM/EDS and an Omicron XPS system with Argus detector were used for EDS and XPS analysis, respectively.

3.3 Results and Discussion

Three BPEI/MMT one-pot mixtures with polymer:clay ratios of 50:50, 20:80, and 10:90 were prepared and applied onto aluminum alloy 2024-T3 coupons. Scribed coated coupons were exposed to salt spray testing (ASTM B117, 5 wt% NaCl at 35 ^{o}C) to assess the effect of the polymer-clay ratio on the anticorrosion properties. **Figure 3.2a** and **Figure 3.2b** show digital pictures of the bare aluminum alloy 2024-T3 before and after 7d salt spray testing, respectively. Severe corrosion, as evidenced by white corrosion products and large pits, was observed for the bare aluminum alloy 2024-T3. **Figure 3.2c** shows an example of the general appearance of a $(BPEI_x/MMT_y)_v$-coated aluminum alloy 2024-T3 before exposure, where the surface is uniform with a white tinge, arising from the clay platelets. **Figure 3.2d-f**, **g-i** and **j-l** correspond to the $(BPEI_{10}/MMT_{90})_{v,}$ $(BPEI_{50}/MMT_{50})_v$ and $(BPEI_{20}/MMT_{80})_v$ compositions after salt spray exposure, respectively. Both the 90 wt% and 50 wt% MMT coatings displayed evidence of corrosion on the aluminum alloy 2024-T3 surface. The 80 wt% MMT coating provided the best corrosion protection, with less occurrence of pitting and corrosion products.

Additionally, superior corrosion inhibition is observed for thicker films (higher volume v of the $BPEI_x/MMT_y$ one-pot mixture). This is exemplified by **Figure 3.2l**, where corrosion was observed mainly near the location of the scribe (red arrow). **Figure 3.3** confirms the trend, in which films containing 90 wt% MMT and $v \geq 4$ ml also showed enhanced performance. The $(BPEI_{20}/MMT_{80})_3$ coating was selected for further study because it provided the best corrosion resistance with less materials consumed.

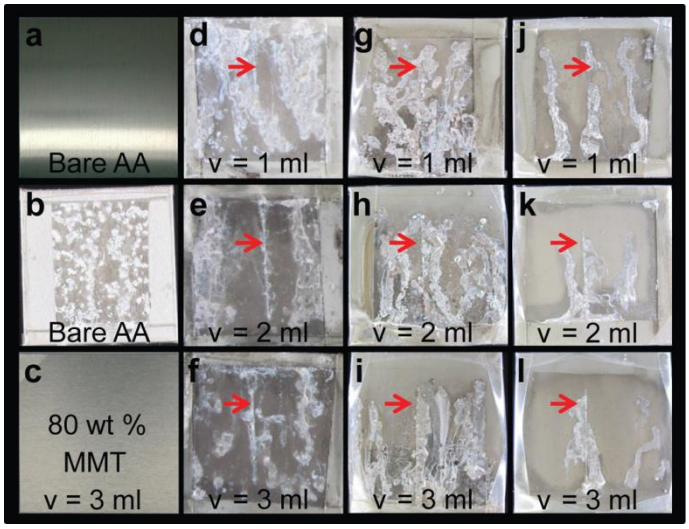

Figure 3.2 Samples exposed to 7d (168h) of salt spray exposure (5 wt% NaCl at 35°C). Bare aluminum alloy 2024-T3 (Bare AA), (a) before and (b) after salt spray exposure. Coated aluminum alloy 2024-T3 panels, c) $(BPEI_{20}/MMT_{20})_3$ before salt spray exposure (example of the general appearance of a $(BPEI_x/MMT_y)_v$–coated aluminum alloy 2024-T3), (d-f) $(BPEI_{10}/MMT_{90})_v$, (g-i) $(BPEI_{50}/MMT_{50})_v$, and (j-l) $(BPEI_{20}/MMT_{80})_v$ after salt spray exposure. Increased thickness (higher volume of the $BPEI_x/MMT_y$ mixture) improved the anticorrosion performance of the coating. The coating with 80 wt% MMT demonstrated superior corrosion inhibition especially where the coating remains intact, as compared to other samples investigated. The red arrows indicate the location of the scribe. Reprinted with permission from Elsevier.

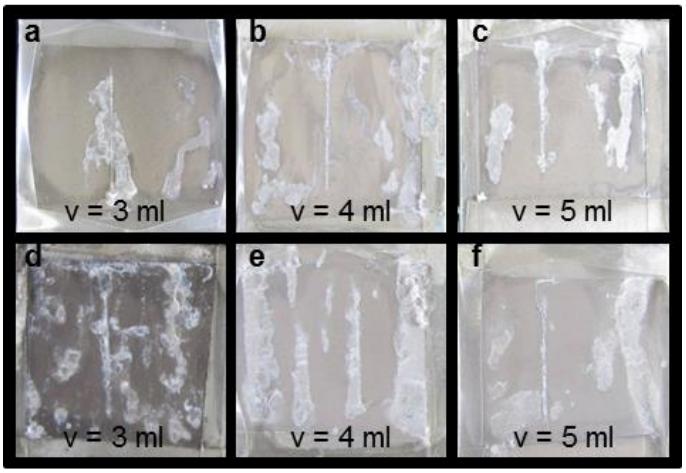

Figure 3.3 Coated aluminum alloy 2024-T3 coupons exposed to 7d (168h) of salt spray testing (5 wt% NaCl at 35°C). (a-c) $(BPEI_{20}/MMT_{80})_v$ and (d-f) $(BPEI_{10}/MMT_{90})_v$. Enhanced corrosion resistance is observed for 90 wt% MMT coatings when $v \geq 4$ ml. Reprinted with permission from Elsevier.

Results from the salt spray test can be linked to the very important role of BPEI with regard to both the properties of the original solution-dispersion mixture and the integrity and anticorrosion properties of the $(BPEI_x/MMT_y)_v$ coatings. The 50:50 BPEI/MMT mixture was watery (η = 2.89 cP) and produced a non-uniform coating, probably because of the excess polymer. The 10:90 BPEI/MMT blend was also watery (η = 6.06 cP) and similarly produced a non-uniform coating, which we attribute to an excess of clay in the mixture. If clay is in excess, then there is not enough BPEI to fully intercalate within the clay platelets and the resulting coating will likely contain clay aggregates. A good balance of BPEI and MMT was found for the 20:80 BPEI/MMT mixture (η = 7.82 cP), where there is likely just enough BPEI to intercalate within the MMT clay, but not too much so as to compromise film quality. This composition also lead to an increase in viscosity, which positively influenced atomization, substrate wetting and the overall corrosion protection performance of the $(BPEI_{20}/MMT_{80})_v$ coatings.

3.3.1.2 Electrochemical Impedance Spectroscopy Measurements

Electrochemical impedance spectroscopy (EIS) was used to evaluate the corrosion resistance of the bare and coated aluminum alloy 2024-T3 when exposed to 5 wt% NaCl over 40 d. To assess the effect of coating thickness on the corrosion resistance, aluminum alloy 2024-T3 coupons were coated with $(BPEI_{20}/MMT_{80})_v$ where v = 1, 2, and 3 ml, with a corresponding thickness of 490, 884, and 1859 nm, respectively. EIS data analysis was performed by fitting the data to an equivalent circuit shown in **Figure 3.4a**. At later times and when a distinct diffusion tail was observed at low frequency, a Warburg element (W) was used to model the diffusion of corrosive agents or corrosion products through the coating. In the circuit, R_u, $R_{pore,}$ and R_p are the electrolyte, the pore, and the polarization resistances, respectively; CPE_c and CPE_{dl} are constant phase elements that describe the coating and the double layer capacitances.

Figure 3.4b presents the behavior of the pore resistance over a 40d period. The $(BPEI_{20}/MMT_{80})_v$ coating made with v = 3ml shows the most stable behavior up to day 9. On day 10, a decrease in pore resistance from 44 x 10^3 ohms-cm^2 to around 190 ohms-cm^2 occurred due to the diffusion of corrosive agents through the coating. After day 10, R_{pore} stabilized around 220 ohms-cm^2, indicating the onset of a self-healing cycle. **Figure 3.4c** shows the behavior of the polarization resistance, which indicates the resistance of the aluminum alloy 2024-T3 to corrosion. R_p values for the $(BPEI_{20}/MMT_{80})_3$-coated aluminum alloy 2024-T3 indicate a higher resistance to corrosion when compared to other samples (v = 1 and 2 ml). Even after 20d of salt exposure, R_p values for the $(BPEI_{20}/MMT_{80})_3$-coated aluminum alloy 2024-T3 remain stable around 1.5 x 10^5 ohms-cm^2. In regards to the other $(BPEI_{20}/MMT_{80})_v$-coated aluminum alloy 2024-T3 samples with v = 1 and 2 ml, R_{pore} and R_p values oscillate throughout the 40d period, probably due to the formation and dissolution of corrosion products. Overall, results from EIS measurements indicate a trend, where thicker coatings provide better corrosion protection to the underlying aluminum alloy 2024-T3.

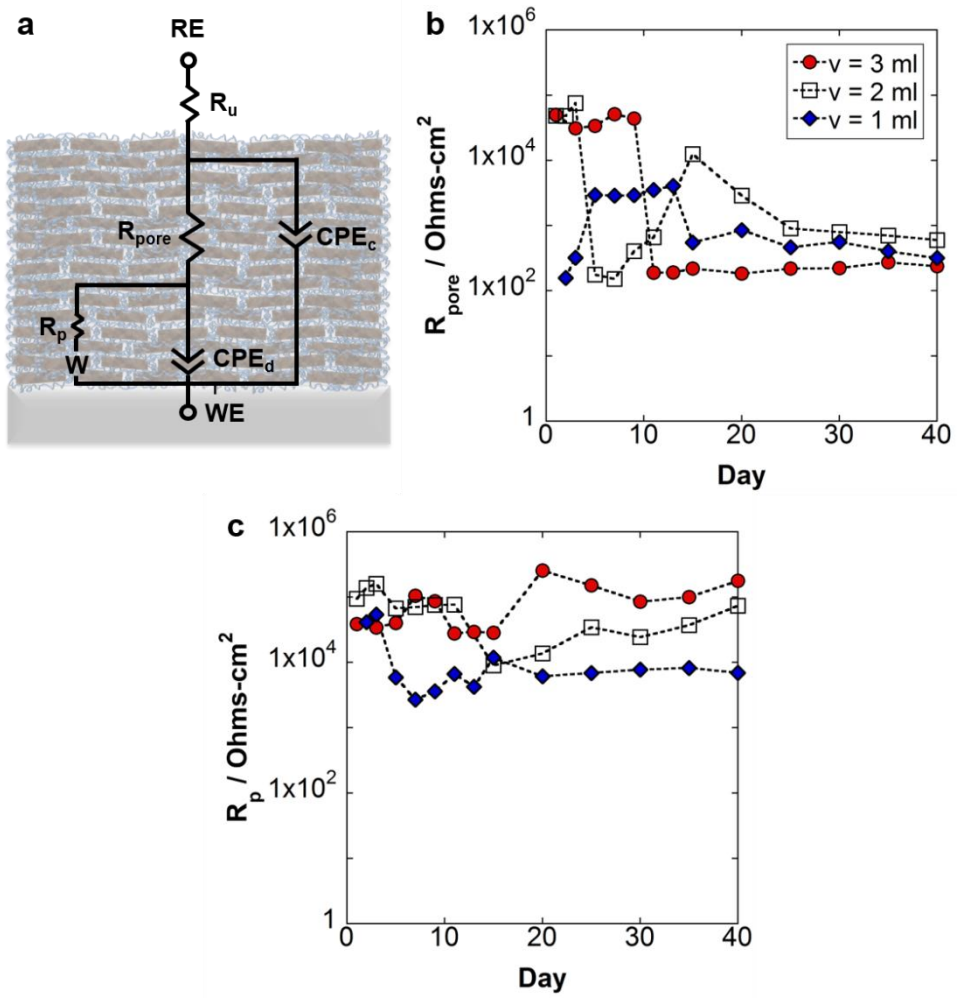

Figure 3.4 Fitted impedance data for $(BPEI_{20}/MMT_{80})_v$–coated aluminum alloy 2024-T3, with *v* = 1, 2, and 3 ml. a) Equivalent circuit used for data fitting, where R_u, R_{pore}, and R_p correspond to the resistances of the electrolyte, the coating, and the charge transfer or polarization. CPE_c and CPE_{dl} are the capacitances of the coating and the double layer, respectively. W: Warburg element. b) R_{pore} and c) R_p behaviors with time. A Warburg element (W) was used to model the diffusion of corrosive agents or corrosion products through the coating. Reprinted with permission from Elsevier.

Figure 3.5 presents Nyquist, Bode, and phase angle plots for the $(BPEI_{20}/MMT_{80})_3$-coated aluminum alloy 2024-T3 sample over the course of 40 d. **Figure 3.5a** shows an increase in the diameter of the impedance arc with exposure time, indicating an improvement in corrosion resistance. **Figure 3.5b** presents the behavior of the total impedance (|Z|) as a function of

frequency. |Z| values at a frequency of 0.01 Hz, initially at 22 x 10^3 ohms-cm^2 on day 1, stabilized after day 20 at 150 x 10^3 ohms-cm^2, indicating improved corrosion protection capabilities of the coating. It is worth noting that after 40 d of salt-exposure the impedance at 0.01 Hz (142 x 10^3 ohms-cm^2) was 730 times higher than that of the bare aluminum alloy 2024-T3 (194 ohms-cm^2) on day one. **Figure 3.5c** shows a phase angle–frequency plot, where a broad peak in the 0.1 – 1000 Hz frequency range can be divided in two time constants. These two time constants correspond to the coating's pore resistance and charge transfer polarization at the coating/substrate interface. The effect of BPEI's molecular weight and the aluminum alloy 2024-T3 surface finish on the anticorrosion performance of the $(BPEI_{20}/MMT_{80})_3$ coatings can be found in Sections 3.3.5 and 3.3.6, respectively.

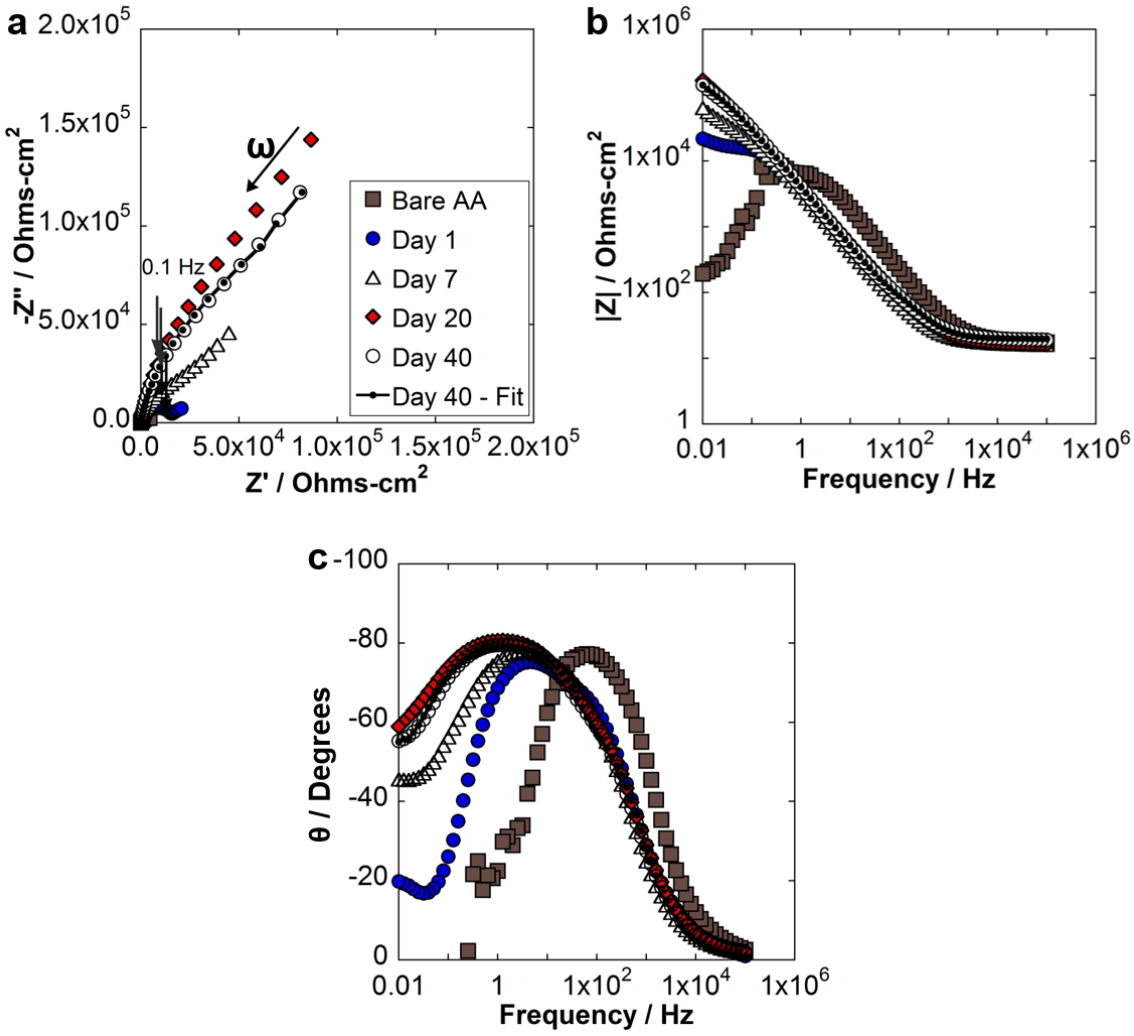

Figure 3.5 $(BPEI_{20}/MMT_{80})_v$–coated aluminum alloy 2024-T3. a) Nyquist plot, b) Bode plot, and c) Phase angle plot. The impedance response of the bare aluminum alloy 2024-T3 (Bare AA) is shown for the first day only. Reprinted with permission from Elsevier.

3.3.2 $(BPEI_x/MMT_y)_v$ Coatings – Effect of Polymer-Clay Ratio on Structure

3.3.2.1 Orientation of MMT Clay Platelets in the Polymer Matrix

A good balance of BPEI and MMT was found to positively impact the corrosion protection properties of the polymer-clay coatings. Therefore, understanding the effect of composition in the PCN's structure is of great interest. The extent of polymer intercalation within the clay platelets,

assessed through the interlayer spacing via wide angle X-ray diffraction (WAXD), provides insight into the PCN's structure, **Figure 3.6**. The basal spacing, which describes the platelet-to-platelet stacking distance, is attributed to the peak at small 2θ values, **Figure 3.6a**. Considering the basal spacing for natural MMT (d_{001} ~ 1 nm),[180, 181] the interlayer spacings for the three compositions were 0.42 nm, 1.15 nm and > 1.94 nm for $BPEI_{10}/MMT_{90}$, $BPEI_{20}/MMT_{80}$ and $BPEI_{50}/MMT_{50}$, respectively. This shows that the interlaying spacing increases as the BPEI content increases, providing important insight into the role of BPEI. An interlayer spacing of 0.42 nm for the $BPEI_{10}/MMT_{90}$ composition indicated clay aggregation and poor polymer intercalation. On the other end, the $BPEI_{50}/MMT_{50}$ composition presented an interlayer spacing greater than 1.94 nm, where the excess of polymer promoted both polymer intercalation and further exfoliation of the clay platelets. The $BPEI_{20}/MMT_{80}$ composition showed an intermediate interlayer spacing of 1.15 nm, consistent with the trend in composition. Results from interlayer spacing as a function of $BPEI_x/MMT_y$ composition align with the analysis of corrosion protection performance in section 3.3.1.1.

The clay platelet orientation was evaluated employing WAXD with tilt where 2θ was fixed at 6.2° for the $BPEI_{20}/MMT_{80}$ composition, **Figure 3.6b**. The maximum intensity was observed at a tilt angle of $\varphi = 6^{\circ}$, suggesting a mostly parallel orientation of the clay platelets with respect to the substrate. This finding is additionally supported by a calculated Herman's orientation parameter of $f = 0.34$,[20] which allows the quantification of the clay platelet alignment within the film with reference to the substrate. *f* values range from -0.5 to 1, where values of -0.5, 0, and 1 indicate perpendicular, random, and parallel orientation, respectively. This shows that the sprayed BPEI/MMT coatings have a tunable interlayer spacing with platelets oriented parallel to the substrate surface.

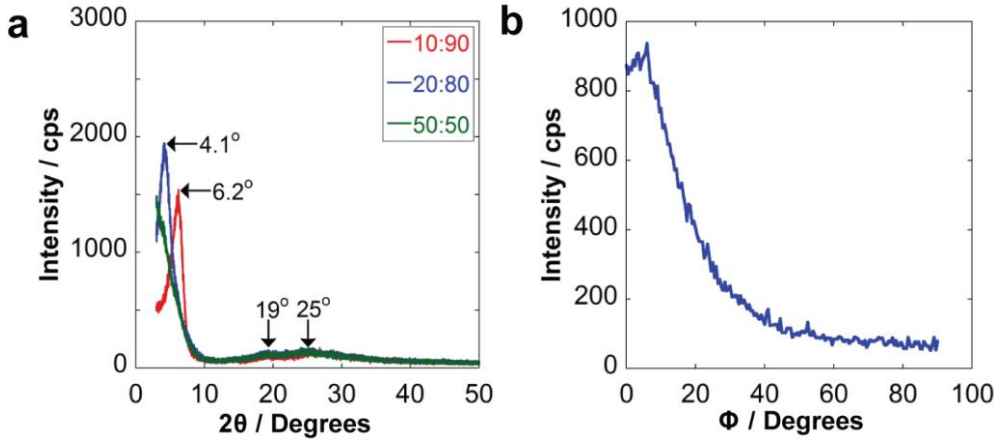

Figure 3.6 a) 2θ patterns for PCN films with $BPEI_x/MMT_y$ compositions. b) WAXD with tilting for a $(BPEI_{20}/MMT_{80})_v$ where 2θ was fixed at 6.2°. A Herman's orientation parameter of 0.34 was calculated from (b); this value indicates preferential parallel orientation of the clay platelets with respect to the substrate. Reprinted with permission from Elsevier.

3.3.2.2 $(BPEI_{20}/MMT_{80})_3$ Coating – Structure

The $(BPEI_{20}/MMT_{80})_3$ coating was chosen for more in depth study due to the results from corrosion tests in section 3.3.1, and structure characterization in section 3.3.2.1. **Figure 3.7a** presents the thickness of the $(BPEI_{20}/MMT_{80})_v$ coating as a function of the one-pot mixture volume (v), measured using profilometry. A linear growth is exhibited, where the calculated thickness per milliliter (slope) is 705 nm-ml^{-1}. The $(BPEI_{20}/MMT_{80})_3$ film exhibited a root-mean-square (rms) roughness of 201 nm (around 11 % of the film's total thickness). **Figure 3.7b,c** exhibit TEM and SEM cross-sectional images of the $(BPEI_{20}/MMT_{80})_v$ coating on a PET plastic substrate and a silicon wafer, respectively. The TEM image in **Figure 3.7b** supports the intercalated structure of the $BPEI_{20}/MMT_{80}$ PCN, where the clay platelets appear as dark elongated particles. Similarly, the coating's multilayered structure is evidenced in **Figure 3.7c**. **Figure 3.7d** (surface SEM image) reveals the smooth surface of the successfully applied $(BPEI_{20}/MMT_{80})_3$ coating on aluminum alloy 2024-T3. The good adhesion of the $(BPEI_{20}/MMT_{80})_3$ coating to the aluminum alloy 2024-

T3 substrate was evaluated by a tape test, **Movie 3.2** (see supplemental files). The processing time for a 1859 nm thick $(BPEI_{20}/MMT_{80})_3$ film was 15 minutes (124 nm-min^{-1}), ~ 40 times faster than films made through spray-assisted layer-by-layer assembly (3 nm-min^{-1}).[15]

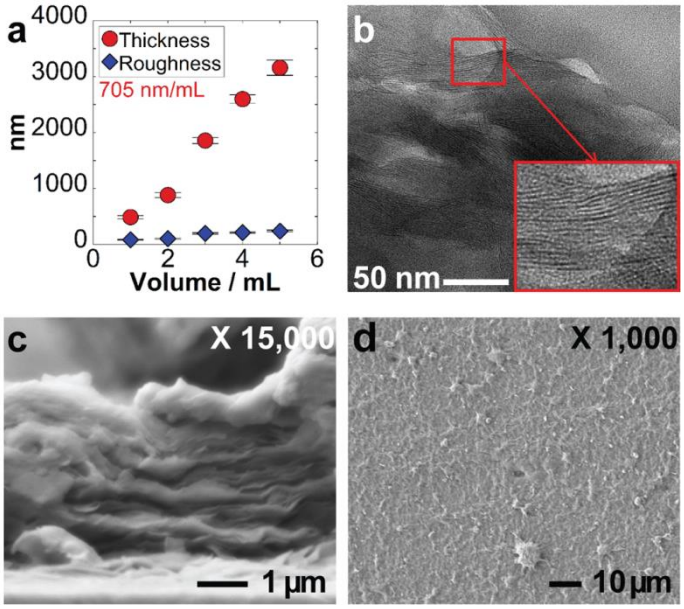

Figure 3.7 $(BPEI_{20}/MMT_{80})_v$ coating. a) Film thickness and roughness on a silicon wafer as a function of the volume of the one-pot mixture sprayed at 30 psi (~206,800 Pa). TEM (b) and SEM (c) cross-sectional images, d) SEM image of the as-prepared $(BPEI_{20}/MMT_{80})_3$ coating on an aluminum alloy 2024-T3 coupon. Reprinted with permission from Elsevier.

3.3.3 $(BPEI_{20}/MMT_{80})_3$ Coating - Barrier Properties

Results from corrosion tests evidenced the good anticorrosion properties of the $(BPEI_{20}/MMT_{80})_3$ coating. Previous work on PCNs has suggested a relationship between corrosion protection and barrier properties.[15, 79, 80, 128, 171-173] Thus, barrier properties of the $(BPEI_{20}/MMT_{80})_3$ coating were examined by oxygen transmission rate (OTR) and oxygen permeability measurements at 0% relative humidity. The OTR for the PET (polyethylene terephthalate ST505) coated with $(BPEI_{20}/MMT_{80})_3$ was 0.047 cm^3-m^{-2}-d^{-1}-atm^{-1}, nearly 180 times

less than the OTR for bare PET (8.6 cm^3-m^{-2}-d^{-1}-atm^{-1}). This data is consistent with data provided in the literature for BPEI/MMT LbL films containing ~ 80 wt% clay.[127, 174] The oxygen permeability of the $(BPEI_{20}/MMT_{80})_3$ film was decoupled from the PET substrate,[159] and calculated to be 0.001 x 10^{-16} cm^3 (STP) cm-cm^{-2}-s^{-1}-Pa^{-1}. The oxygen permeability of the $(BPEI_{20}/MMT_{80})_3$ film is 10 - 100-fold lower than ethylene vinyl alcohol (EVOH), and even lower than most materials used for packaging applications (polyvinyl alcohol, polyamide, etc).[182]

Next, the Brasher-Kingsbury equation was used to calculate the coating water uptake, by relying on values of the coating's capacitance measured at 0 and 24 h following the Rapid Electrochemical Assessment of Paint (REAP) procedure.[149] The water uptake of the $(BPEI_{20}/MMT_{80})_3$ coating on the aluminum alloy 2024-T3 was computed to be 39 v% water. Additionally, a goniometer was used to measure the advancing and receding angles, 38.4º and 27.5º, respectively. Contact angle measurements and the calculated coating water uptake indicate a fairly hydrophilic behavior of the $(BPEI_{20}/MMT_{80})_3$ coating. Interestingly, the $(BPEI_{20}/MMT_{80})_3$ coating's hydrophilicity did not seem to affect its good anticorrosion properties.

3.3.4 $(BPEI_{20}/MMT_{80})_3$ Coating - Elemental Analysis Before and After Corrosion Testing

To fully comprehend the corrosion protection mechanism presented by the $(BPEI_{20}/MMT_{80})_3$–coated aluminum system, XPS and EDS were used. Elemental analysis before and after corrosion testing was performed to analyze the composition of the $(BPEI_{20}/MMT_{80})_3$–coated aluminum alloy 2024-T3 samples, **Figure 3.8**. Three $(BPEI_{20}/MMT_{80})_3$–coated aluminum alloy 2024-T3 samples were studied: 1) before corrosion tests, 2) after EIS measurements (50 d, 5 wt% NaCl), and 3) after salt spray testing (SS, 7 d, 5 wt% NaCl). Detected elements with EDS correspond to the aluminum alloy 2024-T3/PCN coating system. These elements included

aluminum, oxygen, carbon, silicon, nitrogen, copper, and magnesium. XPS data separately confirmed the elemental analysis obtained from EDS.

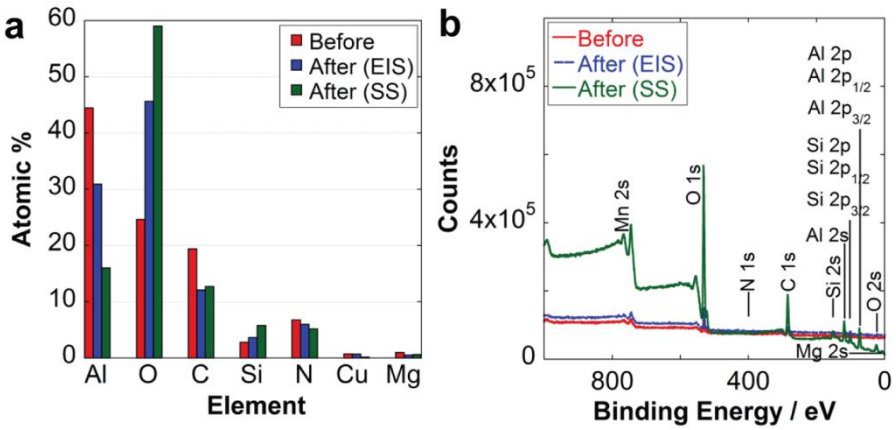

Figure 3.8 $(BPEI_{20}/MMT_{80})_3$-coated aluminum alloy 2024-T3. Sample composition before and after corrosion testing (EIS, 50 d and SS, 7 d). a) EDS and (b) XPS survey scans. Mn, Fe, and Cl < 0.25 atomic %. Only areas where the coating remained intact were examined. The increased oxygen content after 7 d of salt spray testing evidences the harsh conditions for this accelerated corrosion test compared to the continuous exposure to the stagnant 5 wt% NaCl electrolyte during EIS testing. Reprinted with permission from Elsevier.

Salt spray testing is a well-known accelerated corrosion test. Thus, salt spray testing is expected to cause greater damage to the bare/coated metal, versus EIS measurements where the bare/coated metal was exposed to a stagnant salt solution. The oxygen content after salt spray testing is around 13 atomic % higher than for EIS measurements, with values of 59.0 atomic % and 45.7 atomic %, respectively, data which supports the aggressiveness of salt spray testing. Information regarding the presence of corrosion products can be observed when comparing the atomic percentages of oxygen and aluminum present before and after corrosion tests. After corrosion testing, lower aluminum content and higher oxygen content evidence the presence of corrosion products. These corrosion products provide further corrosion resistance through a

plugging effect, where the corrosion products heal defects caused by corrosion, thus resisting and slowing down the corrosion process.[15, 152] This plugging effect is additionally supported by the resistance of the aluminum alloy 2024-T3 to corrode (Figure 3.4c). Together, all results are in agreement with a previously proposed corrosion protection mechanism,[15] where the contributions of BPEI (surface buffering) and MMT (physical barrier), together with the self-plugging effect of passivating corrosion products, provided a self-healing effect of the $(BPEI_{20}/MMT_{80})_3$–coated aluminum alloy 2024-T3 system, rendering overall long-term corrosion protection.

3.3.5 $(BPEI_{20}/MMT_{80})_3$ Coating - Effect of BPEI's Molecular Weight (Mw) on the Corrosion Protection Performance

To understand the effect of BPEI molecular weight, a new 20:80 BPEI/MMT one-pot mixture was prepared with BPEI Mw = 2,000,000 g-mol^{-1}. The structure of the new coating was characterized and compared to the $(BPEI_{20}/MMT_{80})_3$ coating (BPEI Mw = 25,000 g-mol^{-1}). **Figure 3.9** shows SEM surface and cross-sectional images of the coatings, where both present a multilayered structure (**Figure 3.9a,b)**. A significant difference on the coatings' structure can be observed from their surface (**Figure 3.9c,d**), where the coating with the higher BPEI Mw (**Figure 3.9c)** presents a crater-like surface, evidencing a non-homogeneous film deposition (roughness = 572 nm, ~ 33 % of the total coating thickness). To further understand the structure of this new coating (BPEI Mw 2,000,000 g-mol^{-1}) the extent of polymer intercalation was evaluated by XRD (**Figure 3.10**). The main peak at low 2Θ appears at 5.2º, for which the calculated interlayer spacing is 0.71 nm indicating poor polymer intercalation and clay aggregation.

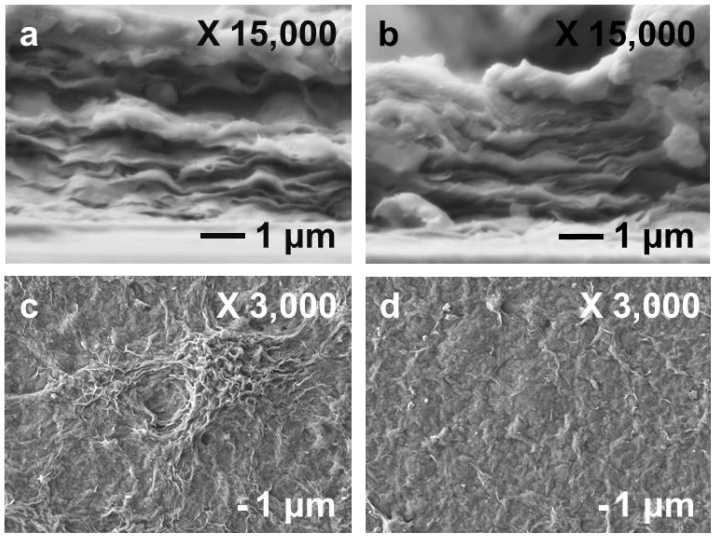

Figure 3.9 SEM images of the 20:80 BPEI/MMT coatings. Cross-sectional image (a) BPEI Mw 2,000,000 g-mol^{-1}and (b) BPEI Mw 25,000 g-mol^{-1}. Surface images (c) BPEI Mw 2,000,000 g-mol^{-1} and (d) BPEI Mw 25,000 g-mol^{-1}. Mw: Molecular weight. Reprinted with permission from Elsevier.

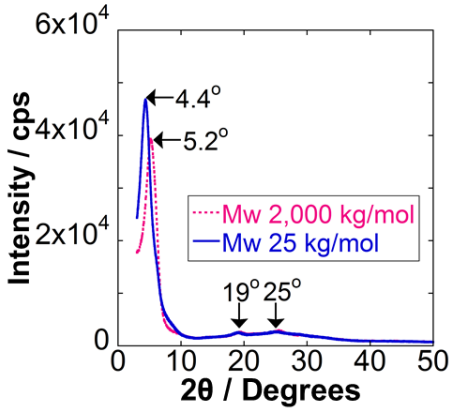

Figure 3.10 2θ patterns for the 20:80 BPEI/MMT coatings. The coating with the lower molecular weight BPEI presents higher interlayer spacing (1.15 nm). An interlayer spacing of 0.71 nm for the coating with the higher molecular weight BPEI indicates poor polymer intercalation and clay aggregation. Reprinted with permission from Elsevier.

The anticorrosion properties of the new film were evaluated by EIS measurements, **Figure 3.11** presents the Nyquist plot up to 7 d of exposure to a 5 wt% NaCl polyelectrolyte solution. The impedance decreases rapidly from day 1 to day 2, evidencing the film's failure. Together, data presented in **Figures 3.9-3.11** evidence poor anticorrosion performance of the new coating due to the higher molecular weight BPEI, where the longer polymer chains result in poor polymer intercalation, clay aggregation, and a rough coating surface.

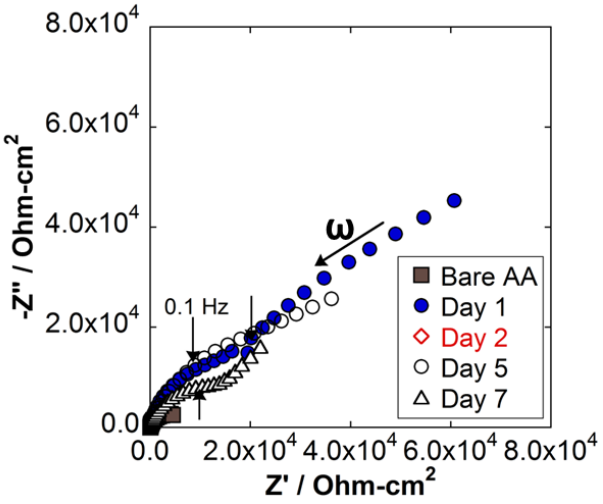

Figure 3.11 Nyquist plot for the coated aluminum alloy 2024-T3 with the 20:80 BPEI/MMT coating (v = 3 ml) containing the higher molecular weight BPEI (2,000,000 g-mol^{-1}). The Nyquist plot shows significant decrease in the impedance as a result of the rapid degradation and failure of the coating. EIS measurements are shown only up to day 7 due to the poor anticorrosion performance of the coating. The impedance response of the bare aluminum alloy 2024-T3 (Bare AA) is shown for the first day only. Reprinted with permission from Elsevier.

3.3.6 $(BPEI_{20}/MMT_{80})_3$ Coating - Effect of Substrate' Surface Finish on the Corrosion Protection Performance

Corrosion in the $(BPEI_{20}/MMT_{80})_3$-coated aluminum alloy 2024-T3 sample is greatly inhibited where the coating remains intact, **Figure 3.2l**. However, some corrosion is observed in areas away from the scribe (**Figure 3.2l)**. This may be due to the inherent defects of the aluminum alloy 2024-T3. These natural defects promote a non-uniform coating deposition, thus allowing the formation of active corrosion areas where the coating is thinner.

Surface modification was used to minimize/eliminate the natural defects of the aluminum alloy 2024-T3. Coupons were sanded to a *2,000 grit* surface finish and a mirror-like surface finish, **Figure 3.12**. Polishing the substrate significantly decreased surface defects allowing for a more uniform deposition of the coating, **Figure 3.12c-f**. The substrate polished to a mirror-like surface finish evidenced residues from the polishing cream in the aluminum matrix, **Figure 3.12e**. Therefore, the substrate sanded to a *2,000 grit* surface finish was chosen to investigate the effect of substrate' surface finish in the anticorrosion performance of the $(BPEI_{20}/MMT_{80})_3$–coated aluminum alloy 2024-T3 system.

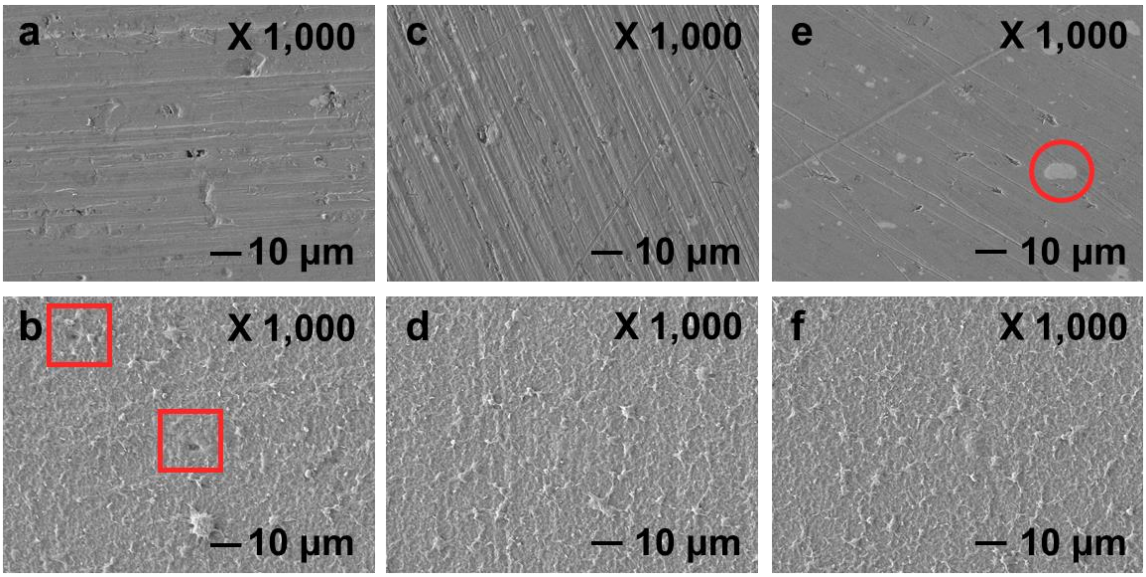

Figure 3.12 Substrate surface finish, (a,b) aluminum alloy 2024-T3, (c,d) 2,000 grit aluminum alloy 2024-T3, and (e,f) mirror-like aluminum alloy 2024-T3. (b, d, f) Coupons coated with the $(BPEI_{20}/MMT_{80})_3$ coating. BPEI Mw = 25,000 g-mol^{-1}. Modification of the surface minimizes natural defects from the aluminum alloy 2024-T3. Reprinted with permission from Elsevier.

Adhesion of the $(BPEI_{20}/MMT_{80})_3$ coating to the *2,000 grit* aluminum alloy 2024-T3 was evaluated by a tape test, **Movie 3.3** (see supplemental files). As can be observed in Movie 3.3, adhesion of the $(BPEI_{20}/MMT_{80})_3$ coating to the *2,000 grit* aluminum alloy 2024-T3 was lost as a result of the lower roughness achieved by sanding the substrate. The contact surface area between the coating and the aluminum was lower as a result of polishing, **Figure 3.13**.

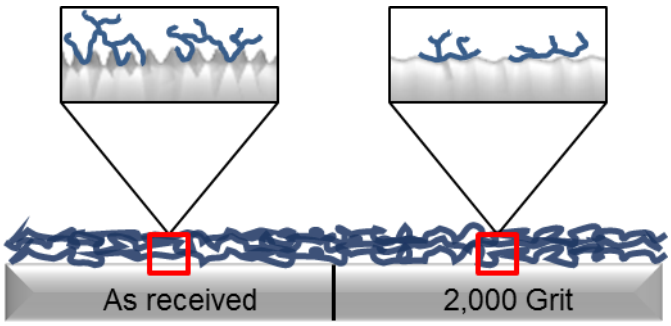

Figure 3.13 Adhesion loss due to modification of the substrate' surface finish. Reprinted with permission from Elsevier.

In order to understand the effect of the substrate's surface finish on the anticorrosion behavior, *2,000 grit* aluminum alloy 2024-T3 coupons were coated with the $(BPEI_{20}/MMT_{80})_3$ film and studied by means of EIS (40 d, 5 wt% NaCl). **Figure 3.14** shows the Nyquist plot for both $(BPEI_{20}/MMT_{80})_3$–coated surface finishes, aluminum alloy 2024-T3 (**Figure 3.14a**) and *2,000 grit* aluminum alloy 2024-T3 (**Figure 3.14b**). In both cases the impedance increased with time and stabilized. However, at day 40 the coated aluminum alloy 2024-T3 presented a total impedance value of 142,500 ohms-cm^2, while the coated *2,000 grit* aluminum alloy 2024-T3 only reached a value of 64,000 ohms-cm^2. A more significant difference can be seen in the behavior of the R_{pore} with time, **Figure 3.14c**. For the coated aluminum alloy 2024-T3 coupons there was initially no diffusion of corrosive agents through the coating. On the other hand, diffusion began on day one for the coated *2,000 grit* aluminum alloy 2024-T3 coupons. Rapid diffusion results from adhesion loss between the coating and the *2,000 grit* aluminum alloy 2024-T3. Interestingly, in both cases R_{pore} increased after 10 d and remained stable (~ 220 ohms-cm^2) during the next 30 d, regardless of the substrate's surface finish. **Figure 3.14d** depicts the behavior of R_p with time. The behavior of R_p is similar for both surface finishes, indicating that even when adhesion between the coating and the substrate is lost, the BPEI/MMT coating provided enough protection to the substrate.

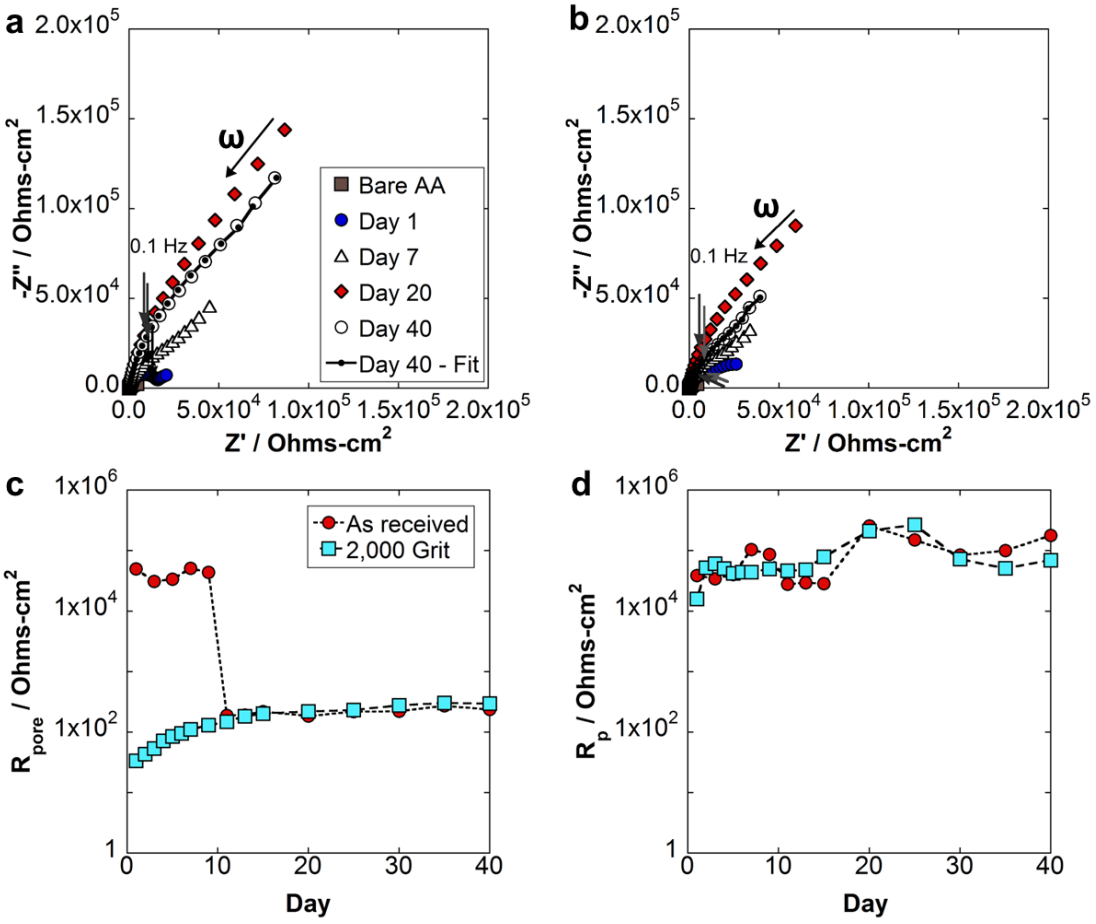

Figure 3.14 Nyquist plots for $(BPEI_{20}/MMT_{80})_3$-coated (a) aluminum alloy 2024-T3 and (b) *2,000 grit* aluminum alloy 2024-T3. b) R_{pore} and c) R_p behaviors with time. Reprinted with permission from Elsevier.

Additional elemental analysis was performed for a $(BPEI_{20}/MMT_{80})_3$–coated *2,000 grit* aluminum alloy 2024-T3 sample after EIS measurements. For comparison purposes the elemental analysis for four samples is showed in **Figure 3.15** (Sample 1: $(BPEI_{20}/MMT_{80})_3$-coated aluminum alloy 2024-T3 before corrosion testing; Sample 2: $(BPEI_{20}/MMT_{80})_3$-coated aluminum alloy 2024-T3 after EIS; Sample 3: $(BPEI_{20}/MMT_{80})_3$-coated aluminum alloy 2024-T3 after salt spray testing; Sample 4: $(BPEI_{20}/MMT_{80})_3$-coated *2,000 grit* aluminum alloy 2024-T3 after EIS). Surprisingly, the oxygen content in Sample 3 (59.0 atomic %) is lower than in Sample 4 (67.4 atomic %) taking

into consideration that they were exposed to salt spray testing and EIS measurements, respectively. Greater amounts of corrosion products present in Sample 4 may be attributed to the coating's adhesion loss caused by the modification of the aluminum alloy 2024-T3 surface finish.

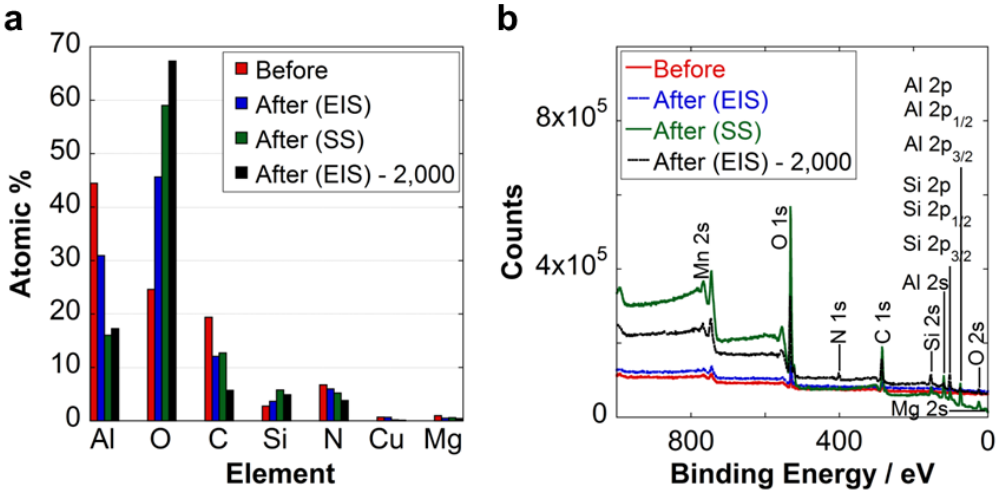

Figure 3.15 $(BPEI_{20}/MMT_{80})_3$-coated aluminum alloy 2024-T3*/2,000 grit* aluminum alloy 2024-T3. Sample composition before and after corrosion testing (EIS, 50 d and SS, 7d). a) EDS and (b) XPS survey scans. Mn, Fe, and Cl < 0.25 atomic %. Only areas where the coating remained intact were examined. Sample 1: $(BPEI_{20}/MMT_{80})_3$-coated aluminum alloy 2024-T3 before corrosion testing; Sample 2: $(BPEI_{20}/MMT_{80})_3$-coated aluminum alloy 2024-T3 after EIS; Sample 3: $(BPEI_{20}/MMT_{80})_3$-coated aluminum alloy 2024-T3 after SS; Sample 4: $(BPEI_{20}/MMT_{80})_3$-coated *2,000 grit* aluminum alloy 2024-T3 after EIS. Reprinted with permission from Elsevier.

In comparison to Sample 2 (**Figure 3.16e**), Sample 4 (**Figure 3.16f**) shows a visible white color on the surface attributed to a higher amount of corrosion products. Curiously, even with the high amount of corrosion products present in Sample 4, both the aluminum alloy 2024-T3 and *2,000 grit* aluminum alloy 2024-T3 coupons show similar resistance to corrosion, **Figure 3.14d**. Similar corrosion resistance is enabled by the plugging effect provided by the corrosion products, which heal defects caused by corrosion, thus resisting and slowing down the corrosion process.

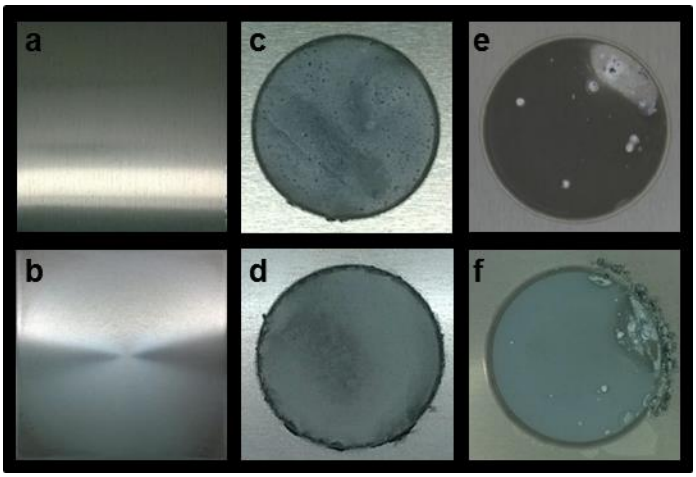

Figure 3.16 Digital images before corrosion testing (a) bare aluminum alloy 2024-T3, and (b) bare *2,000 grit* aluminum alloy 2024-T3. Digital images after EIS measurements (50 d, 5 wt% NaCl), c) bare aluminum alloy 2024-T3, d) bare *2,000 grit* aluminum alloy 2024-T3, e) $(BPEI_{20}/MMT_{80})_3$-coated aluminum alloy 2024-T3 (Sample 2), and (f) $(BPEI_{20}/MMT_{80})_3$-coated *2,000 grit* aluminum alloy 2024-T3 (Sample 4). Reprinted with permission from Elsevier.

3.4 Conclusions

The present study was designed to assess the effects of (a) the film's polymer-clay ratio and (b) the film's structure in the anticorrosion properties of $(BPEI_x/MM_y)_v$ coatings. This study identified a 1.8 μm thick coating with a polymer-clay ratio of 20:80 — processed in only 15 minutes — to provide the best corrosion protection performance. This polymer-clay coating featured an intercalated PCN structure, for which no modification of the MMT clay platelets was necessary. Polymer intercalation within the clay platelets was controlled by the BPEI content in the coating, where BPEI's deficiency or excess resulted in poor polymer intercalation or clay platelet exfoliation, respectively. Furthermore, results from EIS measurements supported the previously proposed corrosion protection mechanism,[15] where the synergistic effect of the MMT (barrier), BPEI (surface buffering), and a plugging effect resulted in long-term corrosion protection of BPEI/MMT-coated aluminum alloy 2024-T3 systems. Additionally, it was found that PCN

coatings on highly polished aluminum alloy 2024-T3 surfaces performed similarly in EIS, but exhibited more corrosion products visually and by EDS because of the poorer overall surface adhesion. Also, the use of a higher molecular weight BPEI (2,000,000 g-mol^{-1}) evidenced poor anticorrosion performance of the PCN coating due to reduced polymer-clay intercalation, increased clay aggregation, and formation of undesirably rough PCN coatings.

In comparison to previously studied BPEI/MMT LbL coatings (25 wt% MMT) for corrosion protection of the aluminum alloy 2024-T3,[15] the one-pot BPEI/MMT coating's corrosion protection performance shown here was improved. As to CCCs,[183, 184] EIS results indicated a higher substrate resistance when coated with the BPEI/MMT coating. At the same time, salt spray results indicated better corrosion protection provided by CCCs due to their self-healing capabilities. As to other chromium-free surface pretreatments for the aluminum alloy 2024-T3, such as, vanadate-doped layered double hydroxide/sol-gel coatings (1.5 – 6.0 μm thick),[185, 186] and cerium-modified sol-gel coatings (2-3 μm thick),[187, 188] we present a thin polymer-clay surface pretreatment that provides similar corrosion protection, even in the long-term (40d) without the need for corrosion inhibiting species. Furthermore, our environment-friendly polymer-clay coatings, made from a one-pot mixture, were quickly applied by using a simple airbrush. This work provides a framework for the exploration of polymer-clay coatings as surface pretreatments in industrial coating systems.

CHAPTER IV

EFFECTS OF TEMPERATURE AND WATER CONTENT ON THE DYNAMIC MECHANICAL BEHAVIOR OF PAH/PAA POLYELECTROLYTE COMPLEXES: TIME-TEMPERATURE AND TIME-WATER SUPERPOSITION PRINCIPLES

4.1 Introduction

Polyelectrolyte complexes (PECs) are the product of strong interactions between oppositely charged macromolecules.[5] When PECs were first discovered, PECs were deemed intractable due to their high physical crosslink density, dominated by intrinsic ion pairing (ion pairing between oppositely charged polymer repeat units).[4] When prepared, dry PECs are glassy and brittle (**Figure 4.1a**). However, in the presence of water PECs transition from a glassy to a rubbery state.[4] Water is considered a plasticizer (**Figure 4.1b**), which increases the free volume in the PEC while weakening the strength of the intrinsic ion pairing. In the presence of salt (**Figure 4.1c**), wet PECs further plasticize due to the ability of salt ions to transform intrinsic ion pairing into extrinsic ion pairing (ion pairing between a charged polymer repeat unit and a salt ion). In fact, adding salt to wet PECs has shown to facilitate the extrusion of PEC pellets into specific shapes.[90] However, salt only behaves as a plasticizer in the presence of sufficient water, otherwise salt behaves as a hardener.[33] Therefore, water is considered an essential plasticizer.[33, 34] Finally, pH has been found to be important — in PECs assembled with at least one weak PE — because pH modifies the charge density of weak PEs (**Figure 4.1d**), controlling the strength of the electrostatic interactions.[2, 34] Thus, in the presence of water PECs can be soft or stiff depending on assembly pH, which can be determined by their T_g or moduli.[2, 27, 34] Overall, the critical role of water in PECs thermal and mechanical properties has been highlighted

in literature. However, a systematic study is lacking regarding the effect of water content on the dynamic mechanical behavior of PECs.

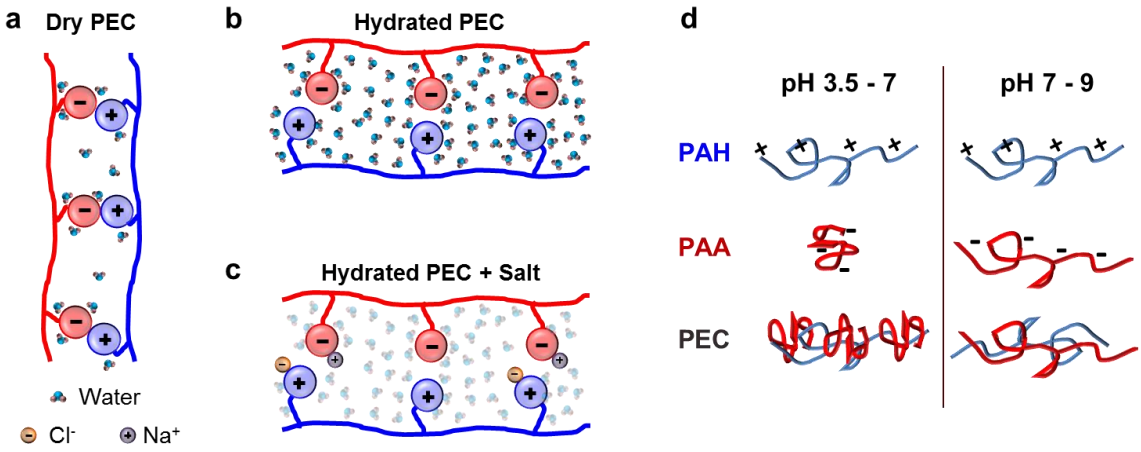

Figure 4.1 Effects of water, salt, and pH on PECs. a) Dry PEC. b) Water acts as a plasticizer increasing the free volume in the PEC, facilitating mobility of the polymer chains. c) Salt transforms intrinsic ion pairing into extrinsic ion pairing, behaving as a plasticizer in the presence of sufficient water content in the PEC. d) pH changes the strength of the electrostatic attraction between PEs (e.g., PAH and PAA), controlling PECs stiffness.

Due to the known effects of water, salt and pH on the morphology and mechanical properties of PECs, equivalence effects between time (frequency), temperature, salt, and pH have been proposed and studied: time-temperature superposition,[31] time-salt superposition,[30] time-temperature-salt superposition,[31] and time-pH superposition.[102] Yet, information is lacking regarding time-water superposition for PECs, considering that water is critical for PECs plasticization.[4, 27, 34, 189]

Therefore, the purpose of this work is to study the mechanical behavior of a salt-free polyelectrolyte complex by analyzing its dynamic mechanical response under several temperatures and relative humidity levels. Additionally, superposition principles such as time-temperature and

time-water superposition principles are used to validate their application for PECs and to predict the dynamic mechanical behavior of the PEC beyond experimental capabilities. Such information is relevant because a materials choice for specific applications relies mainly on the material's mechanical behavior under the conditions of use (time, temperature, relative humidity (water content), salt, pH, etc).

A brief introduction to dynamic mechanical analysis and superposition principles is given below.

4.1.1 Dynamic Mechanical Analysis

Dynamic mechanical analysis consists of the study of a material's response (e.g., stress) to a sinusoidal perturbation (e.g., strain). The material's response can be purely elastic (**Figure 4.2a**), purely viscous (**Figure 4.2b**), or viscoelastic (**Figure 4.2c**) depending on the material's morphology. The ideal elastic behavior follows Hooke's law (**Equation 4.1**),[190] where the stress (σ) at any time is an in phase response proportional to the strain (ε) perturbation. The ideal viscous behavior follows Newton's law (**Equation 4.2**),[190] where the shear stress (τ) at any time is a 90^o out of phase sinusoidal response proportional to the strain rate ($d\varepsilon/dt$) perturbation, with viscosity (η) as the constant of proportionality. A viscoelastic material presents an intermediate response: an out of phase stress response with a phase lag between 0^o (ideal elastic behavior) and 90^o (ideal liquid behavior).

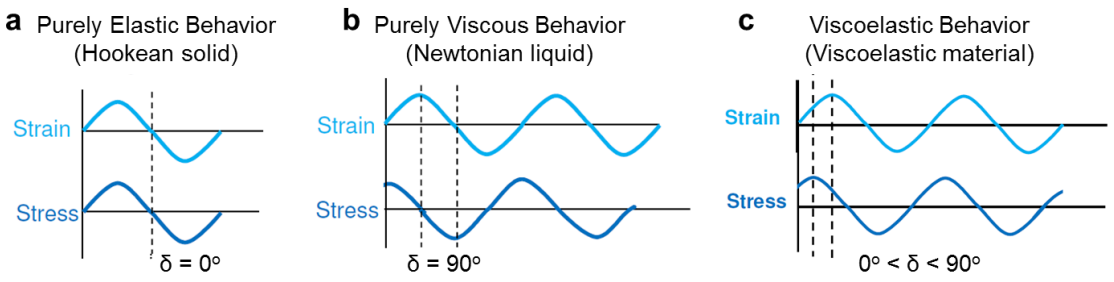

Figure 4.2 DMA sinusoidal stress-strain response curves: a) Ideal elastic behavior, b) ideal viscous behavior, and c) viscoelastic behavior. Reproduced from [91] with permission from TA Instruments. Copyright © TA Instruments. User with permission.

$$\sigma(t) = E\,\varepsilon(t) \qquad \textbf{Hooke's law (Equation 4.1)}[190]$$

$$\tau(t) = \eta\,\frac{d\varepsilon}{dt} \qquad \textbf{Newton's law (Equation 4.2)}[190]$$

A dynamic mechanical analyzer applies a constant strain (e.g., 0.01%) to a material and records the stress response, the complex modulus (E*), and the phase lag (δ). The complex modulus (**Equation 4.3**) is the ratio of the sinusoidal stress response to the sinusoidal strain perturbation, and changes only when the material does.[190] E* is measured at very small strain values, because at these conditions the material's response remains within the linear viscoelastic regime (LVR).[190] In the LVR the modulus does not change as a function of strain and the stress changes linearly with strain (**Figure 4.3**). Thus, since E* is not a function of strain, E* is only a function of time.

The complex modulus is comprised by a real and imaginary part, most commonly known as storage modulus (E') and loss modulus (E''), respectively. E' is a measurement of the material's elastic behavior (stored energy) and is related to the material's stiffness. E" is a measurement of the material's viscous behavior (dissipated energy) and is reflected in the material's damping

capacity. The ratio of E" to E' (**Equation 4.4**) represents the material loss factor or tan delta (tan δ),[190] which indicates the ratio of dissipated energy over stored energy per cycle.

$$E^* = \frac{\sigma(t)}{\varepsilon(t)} = \frac{\sigma_0}{\varepsilon_0}[cos(\delta) + i\, sin(\delta)] = E' + i\, E'' \qquad \textbf{(Equation 4.3)}[190]$$

$$tan(\delta) = \frac{E''}{E'} \qquad \textbf{(Equation 4.4)}[190]$$

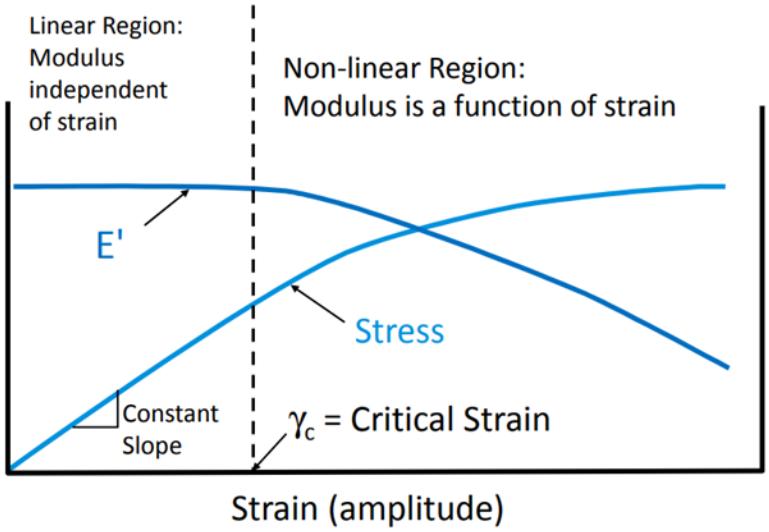

Figure 4.3 Behavior of E' and stress as a function of strain. Linear region: E' is independent of strain. Reproduced from [91] with permission from TA Instruments. Copyright © TA Instruments. User with permission.

4.1.2 Superposition Principles

Superposition principles are a tool used to study physical and mechanical responses of materials (e.g., polymers, polyelectrolyte complexes) beyond experimental capabilities.[102, 190] Specifically, superposition principles are used to analyze frequency-dependent properties such as the complex modulus. The time-temperature superposition principle (TTSP), for example, is a very well-accepted superposition principle that relates the time and temperature response of viscoelastic

materials. Thus, TTSP is used to either determine the temperature-dependence of a material's rheological behavior, or to study a material's behavior at a specific temperature over a broader time range.[190, 191] Consequently, as a result of the data prediction capabilities allowed by TTSP, other superposition principles have been explored to study the dynamic mechanical response of materials to variables other than temperature, such as: salt,[99, 192] pH,[102] and water (humidity)[97, 189, 193, 194].

TTSP is a superposition principle based on the well-known principle of time-temperature equivalence supported by the equivalent mechanical responses of a material. **Figure 4.4** illustrates the principle of time-temperature equivalence, where the mechanical responses of a material at high frequency (short time) and at low temperature are equivalent, as well as the material's responses at low frequency (long time) and at high temperature. Thus, TTSP's foundation relies on the following:[190] If the log modulus-log frequency curve (**Figure 4.4a**) and the log modulus-temperature curve (**Figure 4.4b**) have the same shape, then data taken over a short frequency range (e.g., 10^{-1} – 10^{1} Hz) at a single temperature would duplicate a portion of the log modulus-temperature curve. In consequence, other portions of the log modulus-temperature curve could be duplicated by taking data over the same short frequency range at different temperatures (**Figure 4.5a**).[190] Accordingly, a log modulus-log frequency time-temperature master curve can be constructed by shifting the data taken at different temperatures over the frequency axis (**Figure 4.5b**). This horizontal shift is known as the temperature-dependent shift factor, $\mathbf{a_T}$.

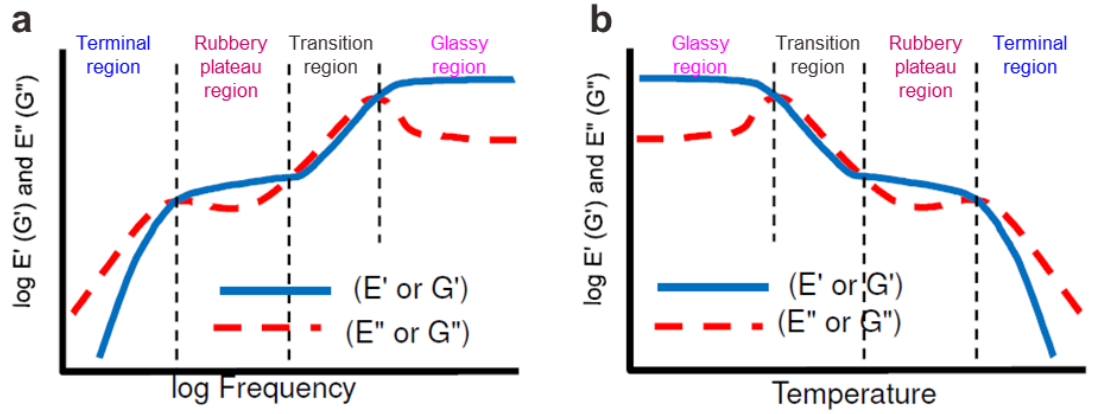

Figure 4.4 Behavior of E' and E" as a function of (a) frequency and (b) temperature. Four regions are marked: terminal, rubbery plateau, transition, and glassy. Adapted from [91] with permission from TA Instruments. Copyright © TA Instruments. User with permission.

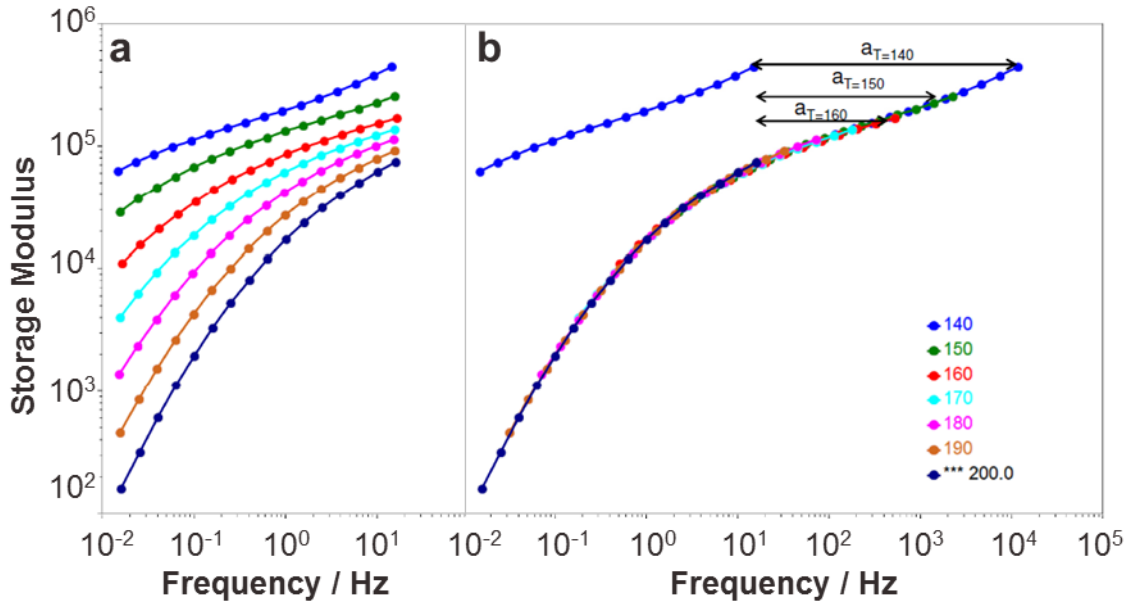

Figure 4.5 Illustration of the time-temperature superposition principle for an unspecified material. a) Log modulus-log frequency curves taken at different temperatures. b) Construction of a log modulus-log frequency master curve by shifting the data in (a) to a reference curve taken at T = 200 °C. Reproduced from [91] with permission from TA Instruments. Copyright © TA Instruments. User with permission.

TTSP provides quantifiable data regarding the temperature-dependent shift factor (a_T). Most importantly, a_T values can be fitted as a function of temperature by using equations such as Williams-Landel-Ferry (WLF, **Equation 4.5**)[190] and Arrhenius (**Equation 4.6**)[190]. Where C_1 and C_2 are empirically adjustable parameters, E_a is the activation energy, R is the universal gas constant, T is temperature, and T_{ref} is the reference temperature. Therefore, WLF and Arrhenius equations provide the means to estimate a_T values for any temperature within the temperature range used to construct the time-temperature master curve.

$$Log(a_T) = \frac{-C_1(T-T_{ref})}{C_2+(T-T_{ref})} \qquad \text{WLF equation (\textbf{Equation 4.5})[190]}$$

$$Ln(a_T) = \frac{E_a}{R}\left(\frac{1}{T} - \frac{1}{T_{ref}}\right) \qquad \text{Arrhenius equation (\textbf{Equation 4.6})[190]}$$

4.2 Experimental Section

4.2.1 Materials

Polyacrylic acid (PAA, Mw 100,000 g-mol^{-1}, 35 wt% aqueous solution) was purchased from Sigma Aldrich. Poly(allylamine hydrochloride) (PAH, Mw 120,000 – 200,000 g-mol^{-1}, 40 wt% aqueous solution) was purchased from Polysciences Inc. PAA and PAH were used as received. Milli-Q water was used for all experiments and solutions preparation.

4.2.2 PAH/PAA Polyelectrolyte Complexes Preparation

A preparation procedure developed by Zhang et at.,[34] to prepare PAH/PAA complexes was followed. 0.1M solutions of PAH and PAA were prepared with respect to their repeat unit. pH of the polyelectrolyte solutions was adjusted to pH 7.00 ± 0.01 with 1M NaOH or 1M HCl. 100 mL of the PAH solution were quickly added to 100 mL of the PAA solution. The PAH/PAA blend was stirred for 30 minutes at 600 rpm. Dialysis of the PAH/PAA PEC in solution was

performed with Milli-Q water at matching pH 7.00 ± 0.01 for 2 days. Dialysis time was determined by following the conductivity of the dialyzing Milli-Q water. The dialyzed PEC in solution was transferred to Falcon tubes and centrifuged for 10 minutes at 8500 rpm and 25 ^{o}C. Centrifuged PECs were recovered, cut into small chunks, and allowed to dry at room conditions for at least 12 hours. Once dry, the PEC chunks were grinded until achieving a powder form.

Recommendation: Prepare specimens from one batch to avoid differences in DMA results due to batch-to-batch variances. Prepare small batches (~1.5 g of PEC) to avoid scalability issues, and then grind them together to obtain one batch.

4.2.3 Sample Preparation

Specimens for dynamic mechanical testing and water content determination were prepared by compression molding according to ASTM D4703-16. A stainless steel flash mold with machined cavities was used. Dimensions of each machined cavity were: 20 mm length, 6 mm width, and 0.5 mm depth. 50 ± 1 mg of the powdered PAH/PAA PEC were carefully placed in each machined cavity. Then, 55 µl of Milli-Q water at pH 7.00 ± 0.01 were added to each cavity. Aluminum foil 1100 was used as the parting agent. The mold was placed in a hot press at 100 ^{o}F for a total of 14 minutes: 10 minutes without any load, 2 minutes with a 2 ton load, and 2 minutes with a 4 ton load. The PEC specimens were removed from the mold, placed between two glass slides to keep them flat, and allowed to dry for ~12 hours at room conditions.

4.2.4 PECs Water Content

Specimens were placed in a homebuilt humidity chamber at the desired RH value and room temperature for at least 24 hours. Weight of the hydrated PEC specimens was measured immediately after at least 24 hours of exposure in the RH chamber. The dry weight of the specimens was measured after drying the hydrated PEC specimens for 3 days in a vacuum oven at

30 ^{o}C. Longer exposure times in the humidity chamber did not increase the PEC water content. Therefore, a period of 24 hours was determined to be sufficient for the PEC specimens to reach the maximum water content (see **Table 4.1**).

4.2.5 Dynamic Mechanical Analysis Measurements

Mechanical testing was performed using a TA Q800 dynamic mechanical analyzer with a relative humidity accessory. A tension clamp configuration was used. PEC films were conditioned in the humidity chamber for at least 24 hours at the desired RH value before DMA measurements were taken. Multi-strain tests were performed to ensure all measurements were within the linear viscoelastic regime for each RH value (50, 70, 80 85, 90 and 95% RH). A strain value of 0.01% was chosen for all multi-frequency strain tests.

Multi-frequency strain (frequency sweep) tests were performed at set temperature and relative humidity values at a strain of 0.01% (value within the linear viscoelastic regime, see **Figure 4.6**) over a 10^{-1} – 10^{1} Hz frequency range. PEC films were allowed to equilibrate for 30 – 40 minutes once the temperature and relative humidity set points were reached. Three frequency sweeps (~ 6 hours) were performed to ensure an equilibrated response and to eliminate any mechanical history of the PEC film. Data from the third frequency sweep was used for time-temperature and time-water superposition analysis. A representative data set from each relative humidity value was chosen for plotting purposes.

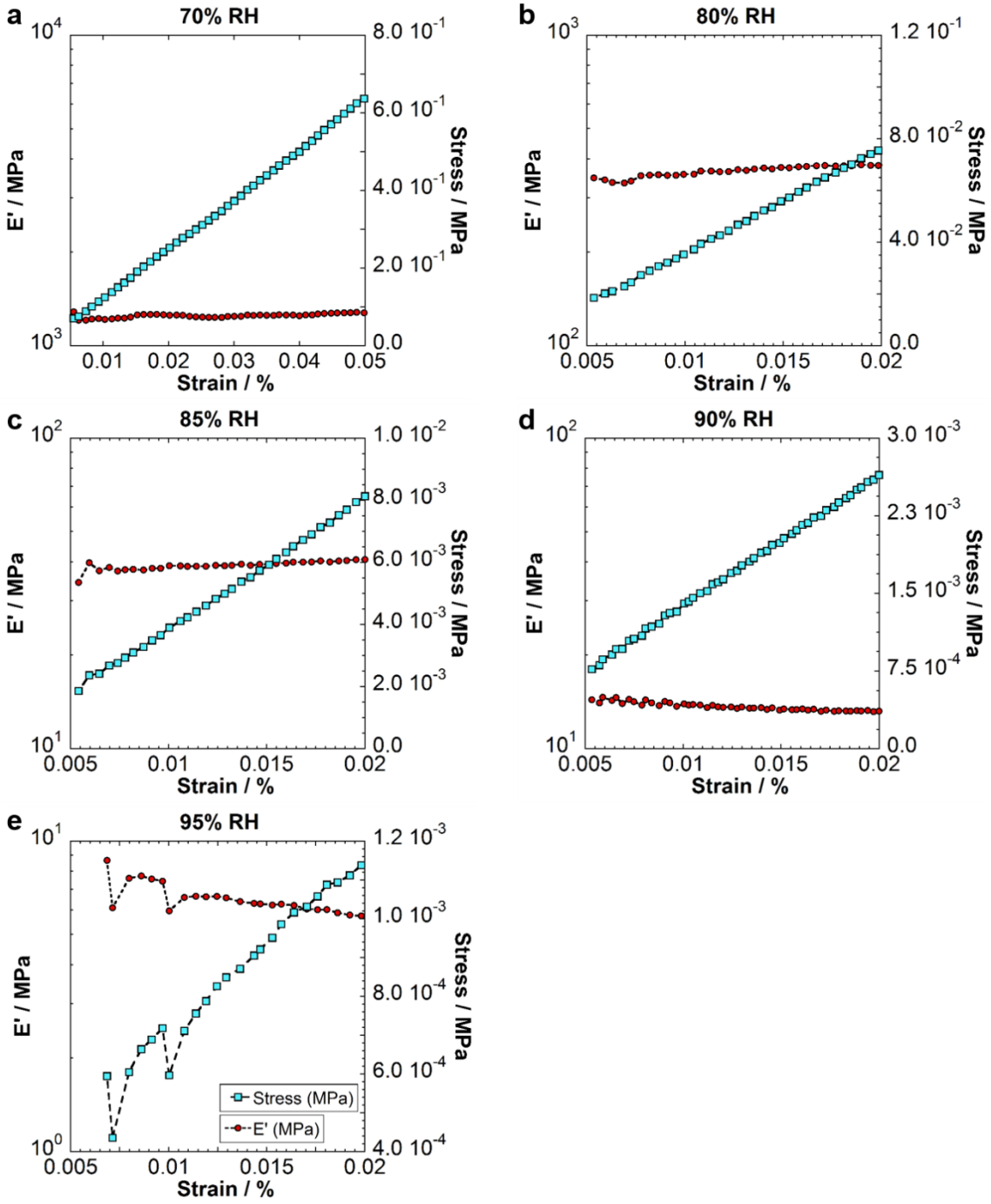

Figure 4.6 Strain sweeps. a) 70% RH, 95 ºC, 0.1 Hz. b) 80% RH, 67.5 ºC, 0.1 Hz. c) 85% RH, 57.5 ºC, 0.1 Hz. d) 90% RH, 55 ºC, 1.0 Hz. e) 95% RH, 40 ºC, 0.1 Hz. A strain value of 0.01% was chosen for all DMA measurements. Legend in (e) applies to all panels.

Multi-frequency strain experiments provided information regarding the PEC mechanical behavior: storage (E') and loss (E") moduli as well as tan delta (E"/E'). A RH range of 50 – 95% was chosen due to sample and instrument limitations. Samples at 50% RH were glassy and brittle, thus resulting in sample failure during experimental set-up (clamping) or early on during DMA testing. Therefore, RH values below 50% were not explored. The DMA relative humidity accessory presented limitations for RH and T ranges as marked in **Figure 4.7**.[195] Upper and lower temperature limits were initially determined according to operating specifications for the DMA relative humidity accessory. Temperature upper limits were additionally narrowed down according to sample failure (yielding) at specific relative humidity values (see **Table 4.1**).

New samples were used for every DMA test and all measurements were taken in duplicates (except at 50% RH). The average measurement (single temperature and single relative humidity) took between 6 – 7 hours.

Table 4.1 Temperature ranges used for frequency sweep tests and PEC water content (W) for different relative humidity values. W was measured with a homebuilt humidity chamber at room temperature (~ 23 ^{o}C).

RH / %	**W ± SD / wt%**	**Measured Temperatures / ^{o}C**
95*	35.7 ± N/A	25.0 - 40.0, ΔT = 2.5
90	31.7 ± 0.6	20.0 - 55.0, ΔT = 5.0
85	24.8 ± 0.4	20.0 - 55.0, ΔT = 5.0; 57.5
80	22.8 ± 0.5	20.0 - 65.0, ΔT = 5.0; 67.5
70	18.7 ± 0.8	20.0 – 80.0, ΔT = 10.0; 85.0, 90.0, 95.0
50	13.5 ± 0.8	20.0 - 90.0, ΔT = 10.0

*Water content at 95% RH was calculated from the linear relationship between a_W and W in section 4.3.2.2.

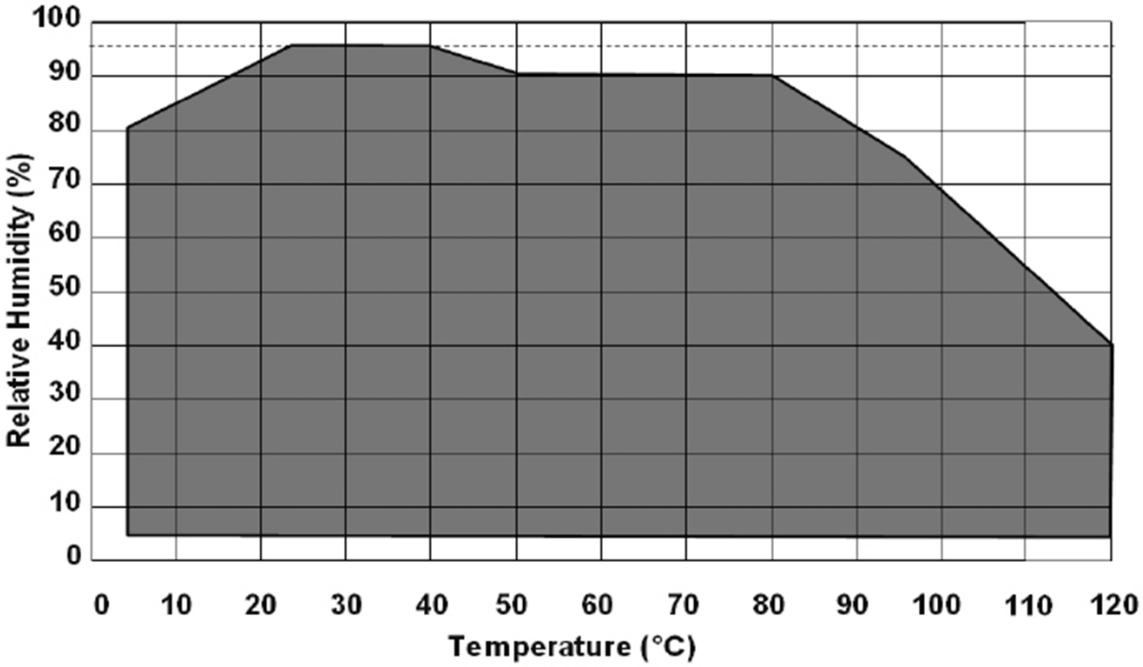

Figure 4.7 DMA-RH accessory limitations. Reproduced from [195] with permission from TA Instruments. Copyright © TA Instruments. User with permission.

4.2.6 Modulated Differential Scanning Calorimetry

Modulated DSC measurements were performed using a TA Q200 differential scanning calorimeter. A heat-cool procedure developed by Shao and Lutkenhaus was followed to measure the glass transition temperature (T_g) of dry PAH and PAA polymers.[38] The T_g for hydrated PAH/PAA PECs was measured following a heat-cool procedure developed by Zhang et.al (rate = 2 $^oC\text{-}min^{-1}$, temperature modulation period = 60 s, and temperature modulation amplitude = ± 1.272 ^oC).[34] In this work, dry (3 d, 30 ^oC under vacuum) powdered PEC samples were hydrated with Milli-Q water at pH 7.00 ± 0.01. Sample mass ranged from 5 – 12 mg. MDSC measurements were performed in duplicates for the dry polymers and in triplicates for the hydrated PECs.

4.3 Results and Discussion

4.3.1 PECs Water Content and T_g

In order to understand the effect of water on the dynamic mechanical behavior of PAH/PAA PEC specimens, their water content was determined at specific relative humidity (RH) values. **Figure 4.8a** shows the equivalent water content in the PAH/PAA PEC at the corresponding relative humidity values, where a linear behavior is observed between 50 and 85% RH. At 90% RH, the PEC absorbs more water from the environment due to increased rearrangement of the PEC structure with increasing RH.[196] This sudden increase in water content above 85% RH, resembles a similar effect observed by Nolte, et al.,[196] when studying the swelling of PEMs as a function of RH, where PEMs evidenced a significant increase in swelling above 90% RH. **Figure 4.8b** presents a linear behavior of the molar fraction of water in the PEC as a function of relative humidity. Finally, **Figure 4.8c** illustrates the glass transition temperature (T_g) as a function of water content in the PAH/PAA PEC. The T_g values measured for the PECs at varying RH values (water content) are in agreement with previously published T_g values for hydrated PAH/PAA PECs studied by Zhang et al.[34] Figure 4.8c shows a relationship between T_g and water content, where T_g decreases with increasing water content. This phenomenon can be explained by the plasticizing effect of water: when water molecules enter the polymeric network the average distance between chains increases, polymer chains relax, and free volume within the PEC increases. This facilitates segmental motion, as evidenced by a decrease in T_g.[197]

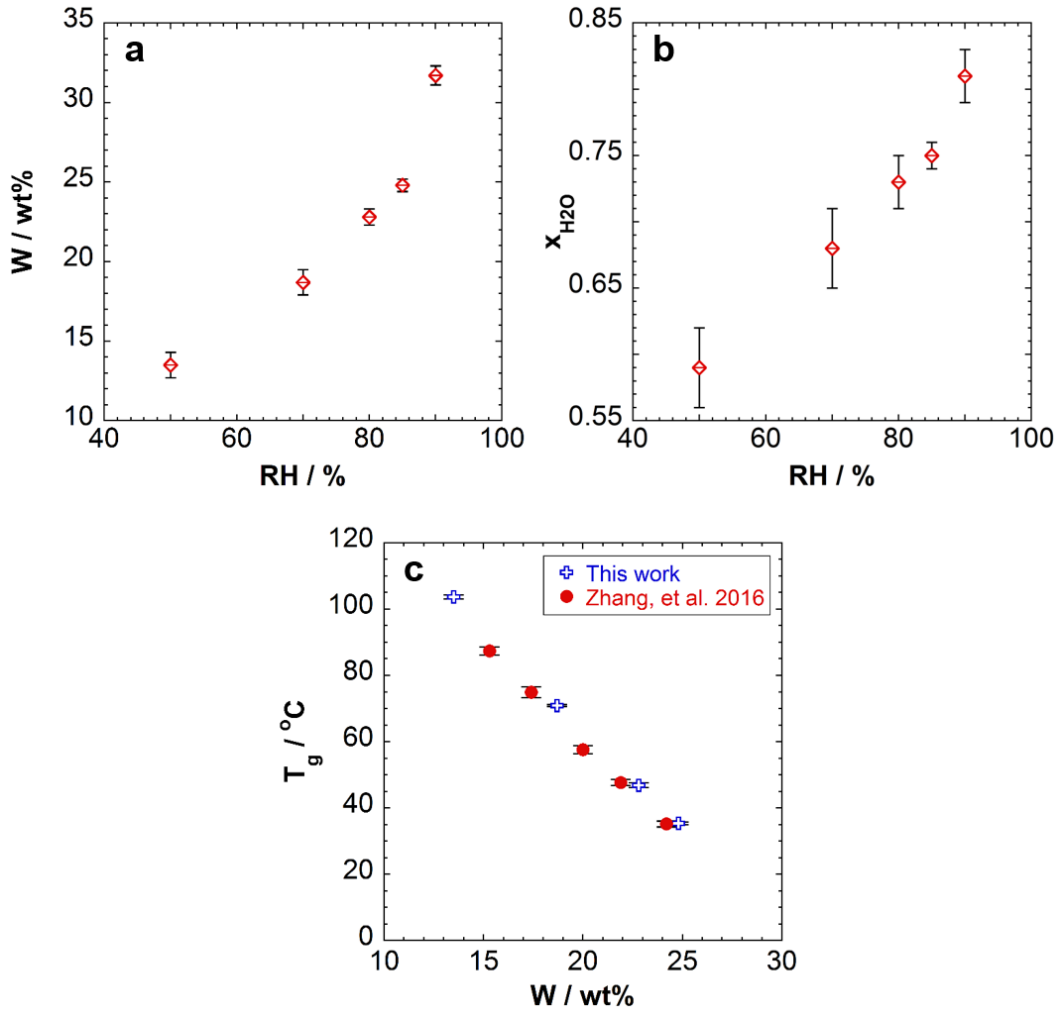

Figure 4.8 a) PAH/PAA PEC water content as a function of relative humidity. b) PAH/PAA PEC water mole fraction as a function of relative humidity. c) Glass transition temperature (T_g) of the PAH/PAA PEC as a function of water content measured using modulated DSC. T_g values for the dry polymers: PAH T_g = 188.3 ± 0.1 °C and PAA T_g = 109.4 ± 0.8 °C.

4.3.2 Dynamic Mechanical Analysis

4.3.2.1 Time-Temperature Superposition

E' data was measured over a 10^{-1} – 10^{1} Hz frequency range at different temperatures and relative humidity values (see **Table 4.1**). **Figure 4.9** presents the application of the time-temperature superposition principle (TTSP) for data taken at 90% RH. **Figure 4.9a** shows the

behavior of E' at different temperatures (20.0 – 55.0, ΔT = 5.0 °C, where ΔT describes the temperature interval) as a function of frequency, where E' decreases with increasing temperature and decreasing frequency. This behavior can be attributed to weakening of polymer-water hydrogen bonding with increasing temperature, followed by polymer chain relaxation.[34] **Figure 4.9b** shows the master curve obtained after application of the TTSP with an arbitrarily chosen reference temperature (T_{ref}) of 40 °C, where data in Figure 4.9a was shifted horizontally along the frequency axis. This horizontal shift over the frequency range is known as the temperature-dependent shift factor, $\mathbf{a_T}$. Figure 4.9b shows a broader frequency range of 10^{-4} – 10^{6} Hz after the application of the TTSP to data taken in a 10^{-1} – 10^{1} Hz frequency range. Therefore, TTSP allows for the study of PAH/PAA PEC mechanical behavior over a frequency range beyond DMA capabilities (10^{-2} – 10^{2} Hz).

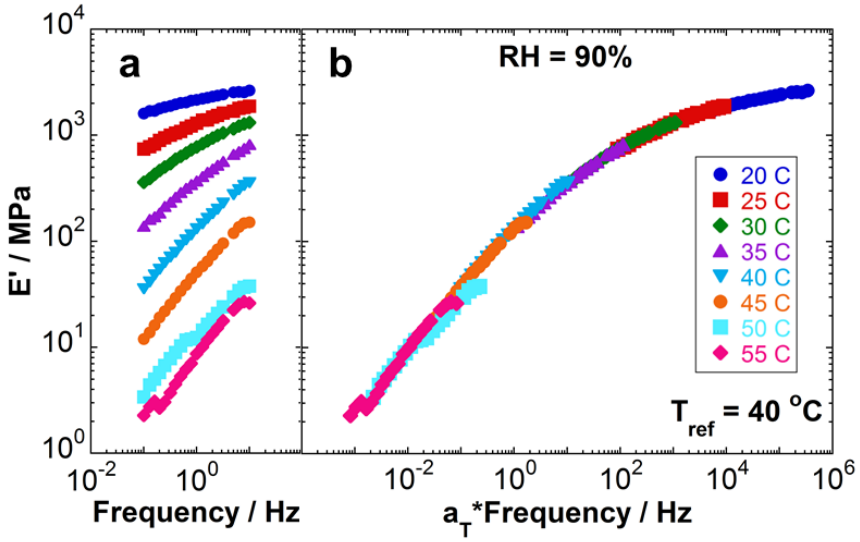

Figure 4.9 Application of the time-temperature superposition principle. a) E' data taken at 90% RH over a 10^{-1} – 10^{1} Hz frequency range and a 20.0 – 55.0 °C temperature range. b) Time-temperature master curve made from experimental data in (a) with T_{ref} = 40 °C. Legend in (b) applies to all panels. E' data taken over a 10^{-1} – 10^{1} Hz frequency range for 50% RH, 70% RH, 80% RH, 85% RH, and 95% RH is shown in **Figure 4.10**. Tan delta data over the same frequency range, for all RH values, is presented in **Figure 4.11**.

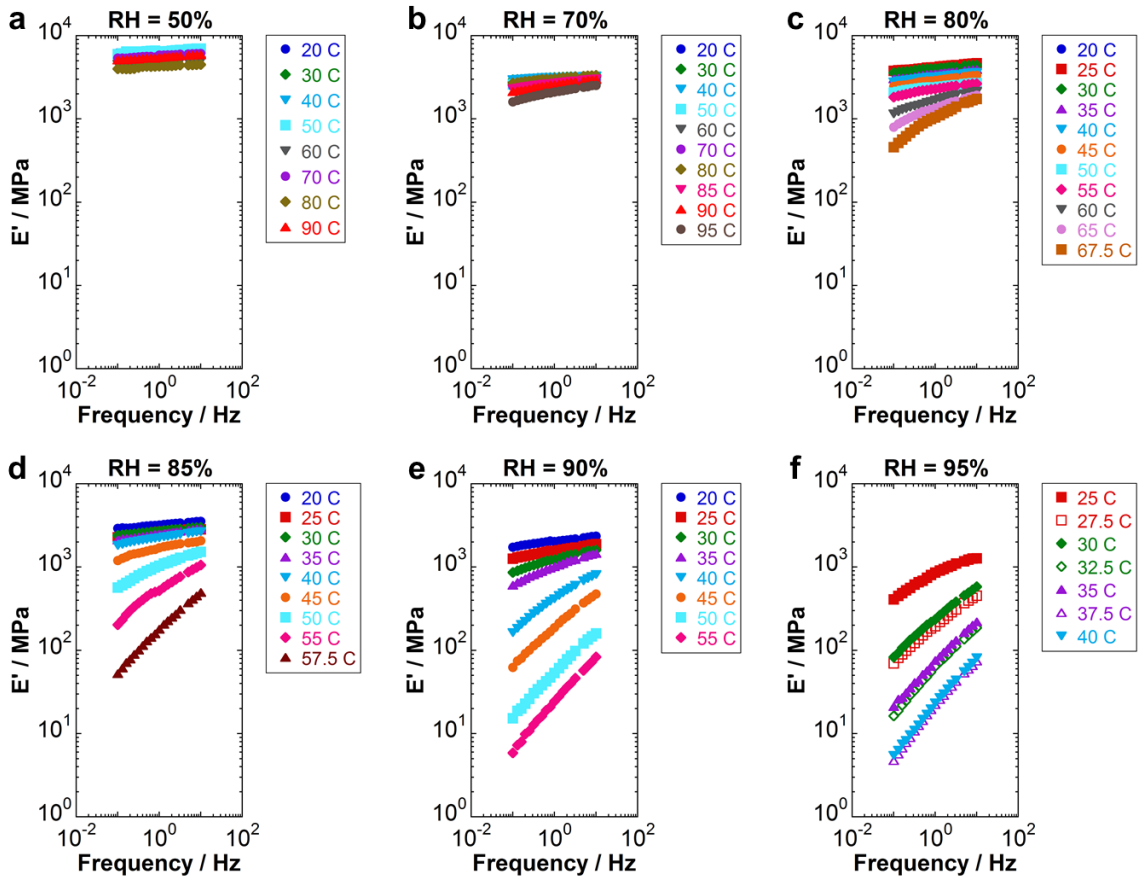

Figure 4.10 Storage modulus (E') data taken over a 10^{-1} – 10^{1} Hz frequency range at different RH values. a) 50% RH, b) 70% RH, c) 80% RH, d) 85% RH, e) 90% RH, and f) 95% RH.

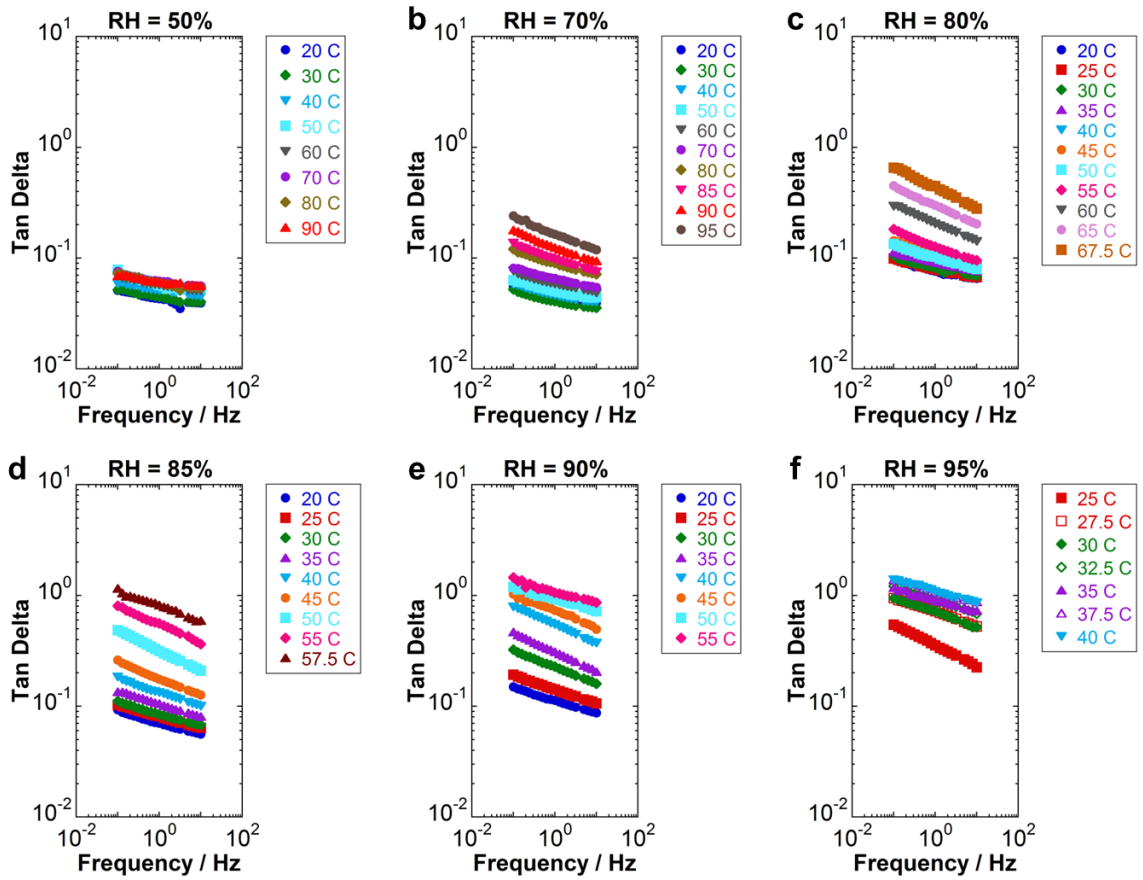

Figure 4.11 Tan delta data over a 10^{-1} – 10^{1} Hz frequency range at different RH values. a) 50% RH, b) 70% RH, c) 80% RH, d) 85% RH, e) 90% RH, and f) 95% RH.

Successful superpositioning of data taken at different temperatures was obtained for RH values of 50, 70, 80, 85, 90, and 95%, indicating applicability of TTSP for PAH/PAA PECs. **Figure 4.12** shows the temperature dependence of a_T fitted with the Arrhenius equation (Equation 4.6), where E_a is the activation energy, R is the universal gas constant, T is temperature, and T_{ref} is the reference temperature. An attempt to fit a_T data using the WLF equation (Equation 4.5) was also made, see **Figure 4.13** and **Table 4.2**. However, values for C_1 and C_2 (empirically adjustable parameters) were not reasonable for RH values below 90%. Additionally, the WLF equation should not be used for cases where: 1) $T > T_g + 100\ ^oC$, 2) $T < T_g$, and 3) the temperature range is

small.[91] Therefore, WLF was deemed not appropriate to describe the dynamic behavior of PAH/PAA PECs.

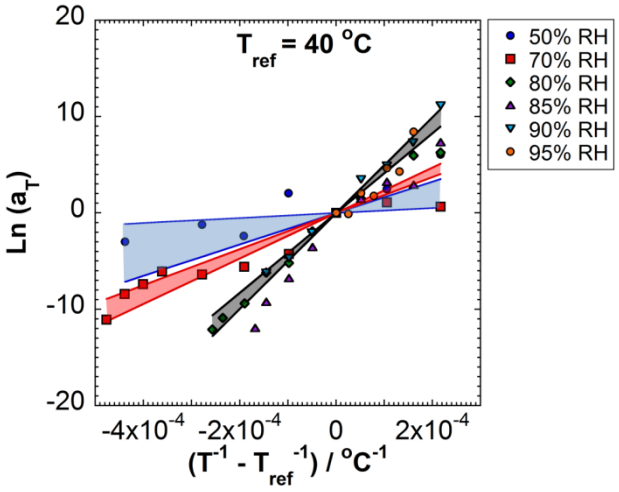

Figure 4.12 Temperature-dependent shift factor (a_T) data calculated for different relative humidity values (T_{ref} = 40 °C) and fitted using the Arrhenius equation (Equation 1). A linear trend is observed, where the slope of the line is equal to the activation energy divided by the universal gas constant. 95% confidence intervals for the slope are represented by the shaded areas: 50% RH (blue), 70% RH (red), and 80 – 95% RH (black).

The activation energy in the Arrhenius equation is related to the small-scale molecular motions causing the relaxation of polyelectrolyte-hydrogen bonds within the PAH/PAA PECs.[190] An activation energy of 379 ± 35 kJ-mol^{-1} (95% confidence interval) was calculated for RH values between 80 and 95%, which suggests that a_T is independent of relative humidity (water content) within that range. Figure 4.12 also shows activation energies of 176 ± 20 kJ-mol^{-1} and 78 ± 57 kJ-mol^{-1} for 70% RH and 50% RH, respectively. An increase in activation energy with increasing water content indicates that the increasing polyelectrolyte-water hydrogen bonding results in a stiffening mechanism. Thus, the energy barrier necessary for the occurrence of molecular motions causing the relaxation of the polyelectrolyte-water hydrogen bonds increases

with increasing water content in the PAH/PAA PEC.[198] For RH < 80%, a_T covers a shorter range suggesting that temperature has a weaker effect on the relaxation of the polyelectrolyte-water hydrogen bonding. For RH $\geq$ 80%, a_T covers a broader range suggesting that temperature has a stronger effect on the relaxation of the polymer chains. **Table 4.3** presents E_a, C_1, and C_2 values for other materials, where a wide range of E_a values is observed.

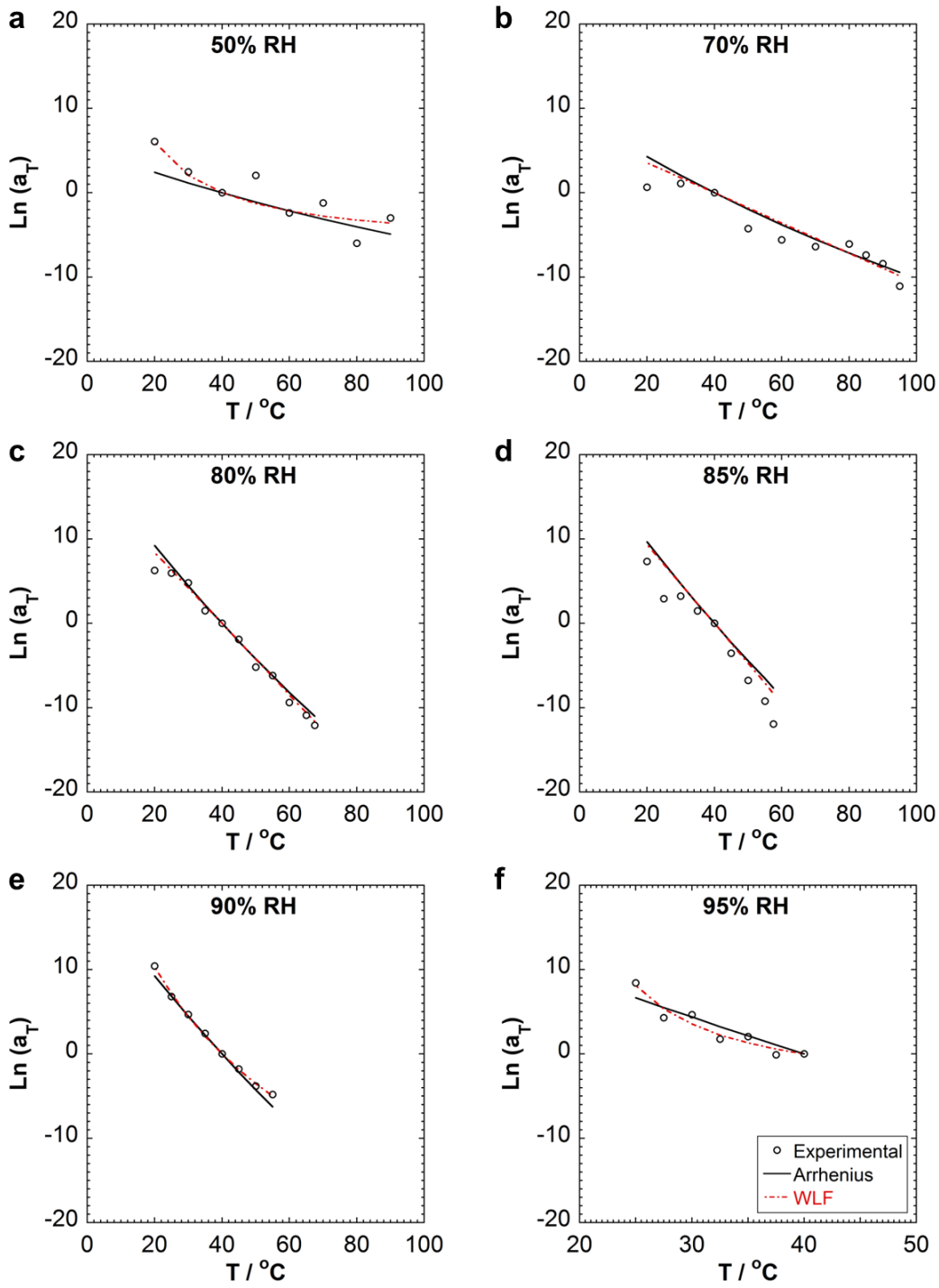

Figure 4.13 Ln(a_T) data fit with Arrhenius and WLF equations. a) 50% RH, b) 70% RH, c) 80% RH, d) 85% RH, e) 90% RH, and f) 95% RH. T_{ref} = 40 °C. Legend in (f) applies to all panels.

Table 4.2 E_a, C_1 and C_2 values. T_{ref} = 40 ^oC.

RH / %	W ± SD[a] / wt%	E_a[b,c] / kJ-mol^{-1}	C_1[d]	C_2[d] / K
95	35.7 ± N/A	379 ± 35	2.222	24.300
90	31.7 ± 0.6	379 ± 35	14.140	82.500
85	24.8 ± 0.4	379 ± 35	2.38×10^8	1.16×10^9
80	22.8 ± 0.5	379 ± 35	5.98×10^7	3.24×10^8
70	18.7 ± 0.8	176 ± 20	4.84×10^7	6.23×10^8
50	13.5 ± 0.8	78 ± 57	2.869	41.750

[a] Water content calculated from exposure of PEC specimens to humidity in a homebuilt humidity chamber
[b] E_a values obtained from fitting a_T data with the Arrhenius equation (Equation 4.6)
[c] 95% confidence interval
[d] C_1 and C_2 values obtained from fitting a_T data with the WLF equation (Equation 4.5)

Table 4.3 E_a, C_1, and C_2 values for other polymeric materials

Material	Ref.	Technique/Test conditions	E_a[a] / kJ-mol^{-1}	C_1[b]	C_2[b] / K
This work	-	DMA Testing / Film tension clamp Conditioned samples (see Table 1)	78 ± 57 (50% RH)[d] 176 ± 20 (70% RH)[d] 379 ± 35 (80 – 95% RH)[d]	-	-
High-temperature epoxy adhesive (Cytec FM300)	[198]	DMA Testing / Three-point bend clamp Dry samples (40 – 140 °C) Conditioned samples (40 – 95 °C)	194[d] (Dry) 143[d] (60% RH and 60 °C) 223[d] (Immersion in water at 70 °C) 804[e] (Dry) 698[e] (60% RH and 60 °C) 360[e] (Immersion in water at 70 °C)	-	-
Nafion	[199]	DMA Testing / Film tension clamp 30% RH. 40 – 90 °C	39[d]	-	-
	[200]	Underwater Stress Relaxometer Immersion. 20 – 70 °C	160[d]	-	-
Epoxy Novolac Resin	[201][c]	DMA Testing / Three-point bend mode Room Temperature – 200 °C	499[e]		
Poly(methyl methacrylate) (PMMA)	[202][c]	Viscoelasticity spectrometer 6 – 80 °C	71.0[d]	8.0	36.0
Polyethylene (LDPE)	[202][c]	Viscoelasticity spectrometer 6 – 80 °C	75.0[d]	71.9	788
Poly(ethylene oxide) (PEO)	[203]	Rheometer / Oscillatory shear rheometry 66 – 138 °C. Dry sample	26.8[d]	6.9	88.0
	[204]	Plazek torsion pendulum 68 – 120 °C. Dry sample	48.9[d]	-	-
Polyacrylate (PAr)	[205]	DMTA Testing / Bending and shear mode 179 – 199 °C. Dry sample	1950[e] 833[d] 799[d]	-	-

Table 4.3 Continued

Material	Ref.	Technique/Test conditions	E_a[a] / kJ-mol^{-1}	C_1[b]	C_2[b] / K
Poly(aryl ether sulfone) (PSF)	[205]	DMTA Testing / Bending and shear mode 179 – 199 °C. Dry sample	1937[e] 770[d] 1038[d]	-	-
Bisphenol A polycarbonate	[205]	DMTA Testing / Bending and shear mode 144 – 164 °C. Dry sample	1012[e] 485[d] 774[d]	-	-
Phenoxy (PH)	[205]	DMTA Testing / Bending and shear mode 86 – 104 °C. Dry sample	1548[e] 389[d] 490[d]	-	-
Carbon fiber / Epoxy Composite 12 K x 3 K	[206]	DMA Testing / Three-point bend clamp 30 – 75 °C. Dry and immersed in water	408[e] (Dry) 382[e] (Wet environment for 11 months) 393[e] (Wet environment for 18 months)	-	-
Carbon fiber / Epoxy Composite 6 K x 3 K	[206]	DMA Testing / Three-point bend clamp 30 – 75 °C. Dry and immersed in water	367[e] (Dry) 344[e] (Wet environment for 11 months) 354[e] (Wet environment for 18 months)	-	-

[a] Arrhenius equation
[b] WLF equation
[c] Water content of the material was not reported
[d] Activation energy for a relaxation process
[e] Activation energy for the glass transition

Glass transition temperature (T_g) data determined by DMA is usually obtained from a) a peak in the loss modulus (which "more closely denotes the initial drop of E' from the glassy state into the transition") or b) a peak in tan delta (which "corresponds more closely to the transition midpoint or inflection point of the decreasing log E' curve").[190] **Figure 4.14** presents E', E'', and tan delta data as a function of temperature for each RH value. No peaks in E'' or tan delta were observed, except for data taken at 90% RH where a peak in tan delta appeared at a temperature of 50 ^oC. Therefore, T_g data was taken at the intersection of two tangents for E' and tan delta curves (Figure 4.14), which in this work is referred as the onset T_g determined by DMA (onset $T_{g,\,DMA}$) and presented in **Table 4.4**. Onset T_g values of 80.0, 58.7, 40.0 and < 20.0 ^oC were observed for 70, 80, 85, and 90% RH values, respectively. In general, T_g values determined by MDSC ($T_{g,\,MDSC}$) are in agreement with onset T_g values determined by DMA (onset $T_{g,\,DMA}$).

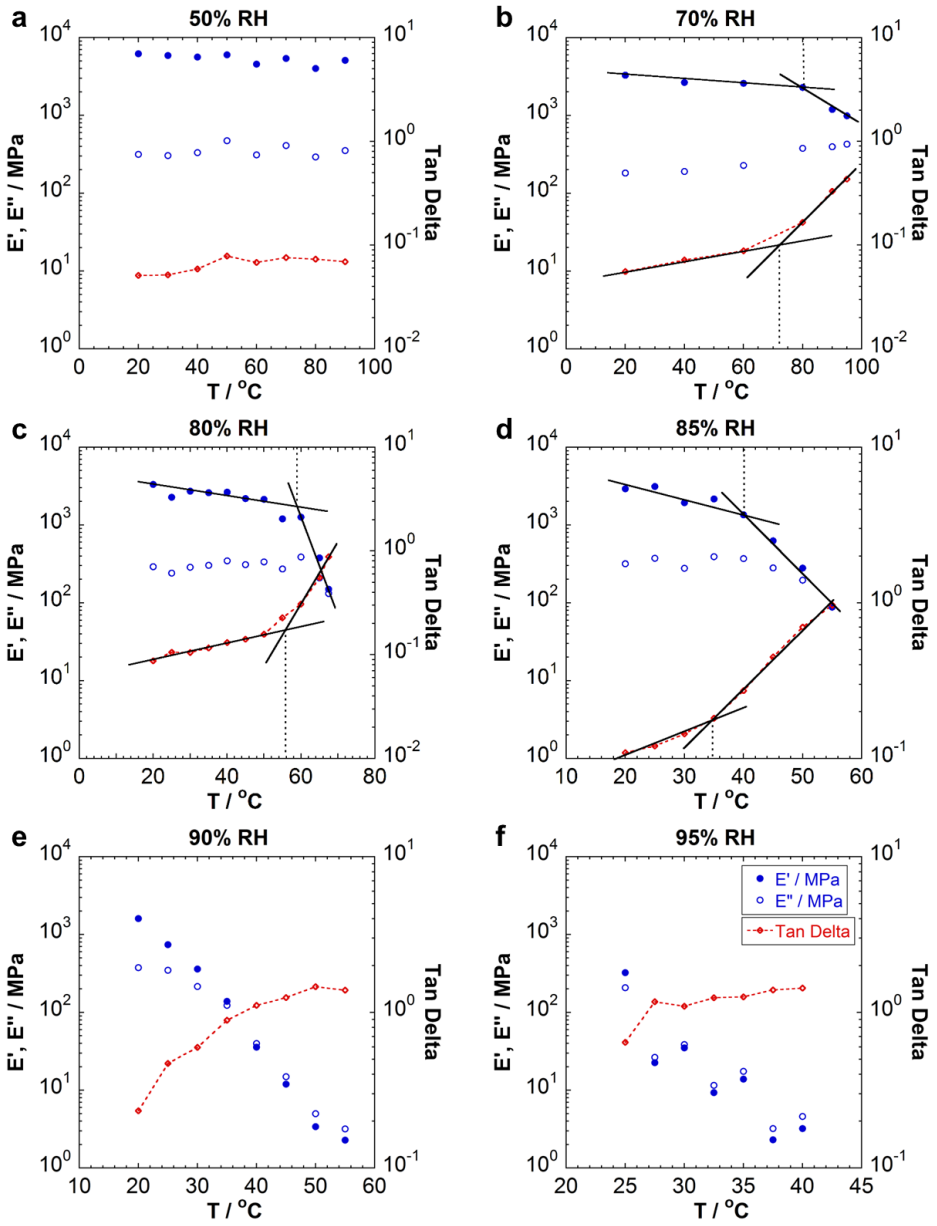

Figure 4.14 Storage modulus, loss modulus, and tan delta (measured at 0.1 Hz) as function of temperature. a) 50% RH, b) 70% RH, c) 80% RH, d) 85% RH, e) 90% RH, and f) 95% RH. Legend in (f) applies to all panels. A peak in tan delta is only observed in panel (e) at 50 °C, evidencing the transition of the PAH/PAA PEC from glassy to rubbery. The intersection of the two tangents were used to determine onset T_g values from E' and tan delta. Onset T_g values are presented in Table 4.4.

Table 4.4 Comparison of T_g data obtained from MDSC and DMA measurements. T_g data for PEC specimens exposed to RH > 85% were not detected with MDSC.

RH / %	W ± SD[a] / wt%	$T_{g,\,MDSC}$ ± SD / °C	Onset $T_{g,\,DMA}$[b] / °C	Onset $T_{g,\,DMA}$[c] / °C
95*	35.7 ± N/A	-	-	-
90	31.7 ± 0.6	-	-	< 20.0
85	24.8 ± 0.4	35.4 ± 0.4	34.8	40.0
80	22.8 ± 0.5	46.9 ± 0.7	55.8	58.7
70	18.7 ± 0.8	70.9 ± 0.3	72.2	80.0
50	13.5 ± 0.8	103.7 ± 0.6	-	-

[a] Water content calculated from exposure of PEC specimens to humidity in a homebuilt humidity chamber
[b] Onset T_g determined from Tan Delta in Figure S5
[c] Onset T_g determined from E' in Figure S5, where a sharp decrease in E' occurs

In reviewing the literature, only a few articles were found on the study of temperature effects on the dynamic mechanical behavior of PECs and on the application of the time temperature superposition principle (see Table 1.1).[31, 109, 110, 114] Shamoun,[31] , Ali,[114] Wang,[109] and Sadman,[110] studied wet solid PECs and PEC coacervates, thus ignoring the effect of water content on the dynamical behavior of PECs. These studies, however, proved the successful application of the TTSP for PECs such as PDADMA/PSS (poly(diallyldimethylammonium chloride) / poly(styrene sulfonate)),[31, 114] PMMA/F127 (poly(methacrylic acid) / triblock copolymer Pluronic VR),[109] and PSS/QVP (poly(styrene sulfonate) / quaternizing poly(4-vinylpyridine)).[110] In this work, the application of the TTSP was validated for PAH/PAA PECs. Most importantly, the effects of temperature on the dynamic mechanical behavior of PECs were studied at different PEC hydration levels (13.5 – 35.7 wt%). Thus, providing novel information

regarding the plasticizing effect of water when PECs are not fully hydrated, which emulate real ambient conditions such as RH known to affect the mechanical behavior of polymeric materials.

4.3.2.2 Time-Water Superposition

Time-temperature master curves were obtained for six relative humidity values: 50, 70, 80, 85, 90, and 95%. **Figure 4.15** presents the application of the time-water superposition principle (TWSP). **Figure 4.15a** shows all six time-temperature master curves in one single E' versus frequency plot, where E' decreases with increasing relative humidity (increasing water content). This behavior can be attributed to an increase in free volume with increasing water content, which promotes structural rearrangement within the PEC.[27, 33] **Figure 4.15b** shows the super master curve obtained after application of the TWSP with an arbitrarily chosen reference relative humidity (RH_{ref}) of 80% (22.8 wt% H_2O), where data in Figure 4.15a was shifted horizontally along the frequency axis. Due to this additional data shifting, a second shift factor was defined as the water-dependent shift factor, $\mathbf{a_W}$. The time-water super master curve shown in Figure 4.15b corresponds to a doubly shifted hygrothermal master curve, which represents the time dependence of E' at a single reference temperature and a single reference relative humidity (water content). Therefore, the successful construction of the time-water super master curve indicates the applicability of the time-water superposition principle for PAH/PAA PECs. E', E'', and tan delta super master curves, with T_{ref} = 40 ^{o}C and RH_{ref} = 80%, are shown in **Figure 4.16**.

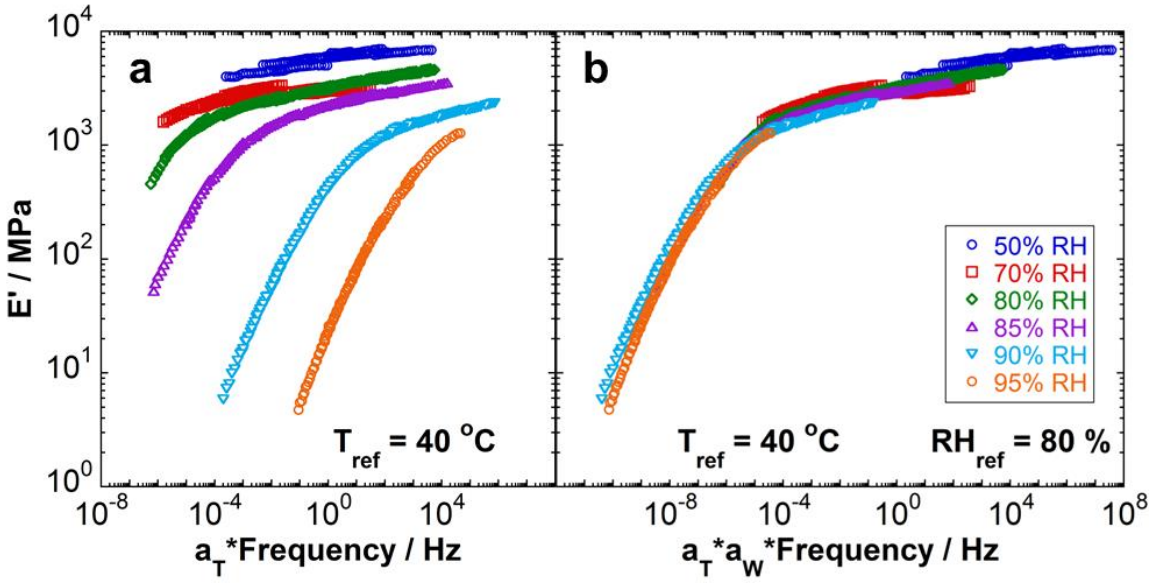

Figure 4.15 Application of the time-water superposition principle. a) Time-temperature master curves for RH values of 50, 70, 80, 85, 90, and 95%. b) Time-water super master curve made from time-temperature master curves in (a) with RH_{ref} = 80% and T_{ref} = 40 °C. Legend in (b) applies to all panels.

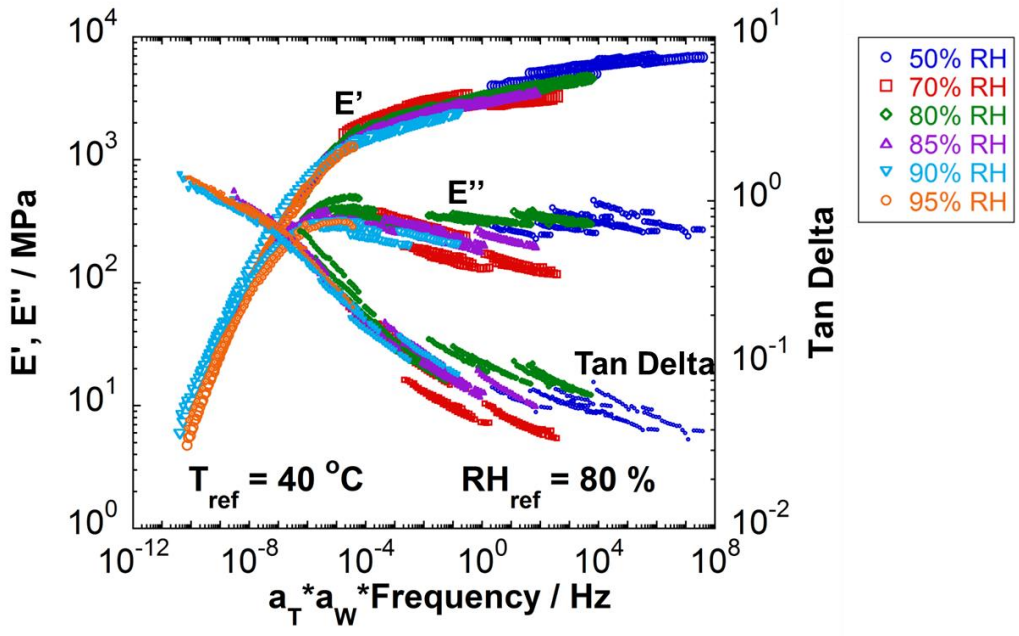

Figure 4.16 Storage modulus (E'), loss modulus (E''), and tan delta super master curves as a function of a_T*a_W*f. T_{ref} = 40 °C and RH_{ref} = 80%. a_T: temperature-dependent shift factor, a_W: water-dependent shift factor, and f: frequency.

Analogous to TTSP, TWSP provides information regarding a water-dependent shift factor a_W. **Figure 4.17** shows the behavior of $\ln(a_W)$ as a function of different parameters. **Figure 4.17a** presents a non-linear behavior for $\ln(a_W)$ with RH, which is probably due to RH being related to the water vapor present in the air, not to the water present in the PEC. **Figures 4.17b-c** show a linear behavior for $\ln(a_W)$ as a function of water content (W / wt%) in the PEC, with Figure 5c taking into account the water content in the PEC at the RH_{ref}. Finally, **Figure 4.17d** shows a non-linear behavior for $\ln(a_W)$ as a function of partial vapor pressure (P_i), which was expected because P_i is directly related to the water vapor present in the air. An attempt to fit a_W data using a WLF-like equation (**Equation 4.7**) was also made, see **Figure 4.18** and **Table 4.5**. However, values for D_1 and D_2 (empirically adjustable parameters) were not reasonable, thus deeming the WLF-like equation not appropriate to describe the dynamic behavior of PAH/PAA PECs. Therefore, a log-linear equation (**Equation 4.8**), with a slope B and a y-intercept c, was proposed to fit a_W as a function of W instead of RH.

$$Ln(a_W) = \frac{-2.303 D_1 (W - W_{ref})}{D_2 + (W - W_{ref})}$$

WLF equation (**Equation 4.7**)[207]

$$Ln(a_W) = B\,(W - W_{ref}) + c$$

(**Equation 4.8**)

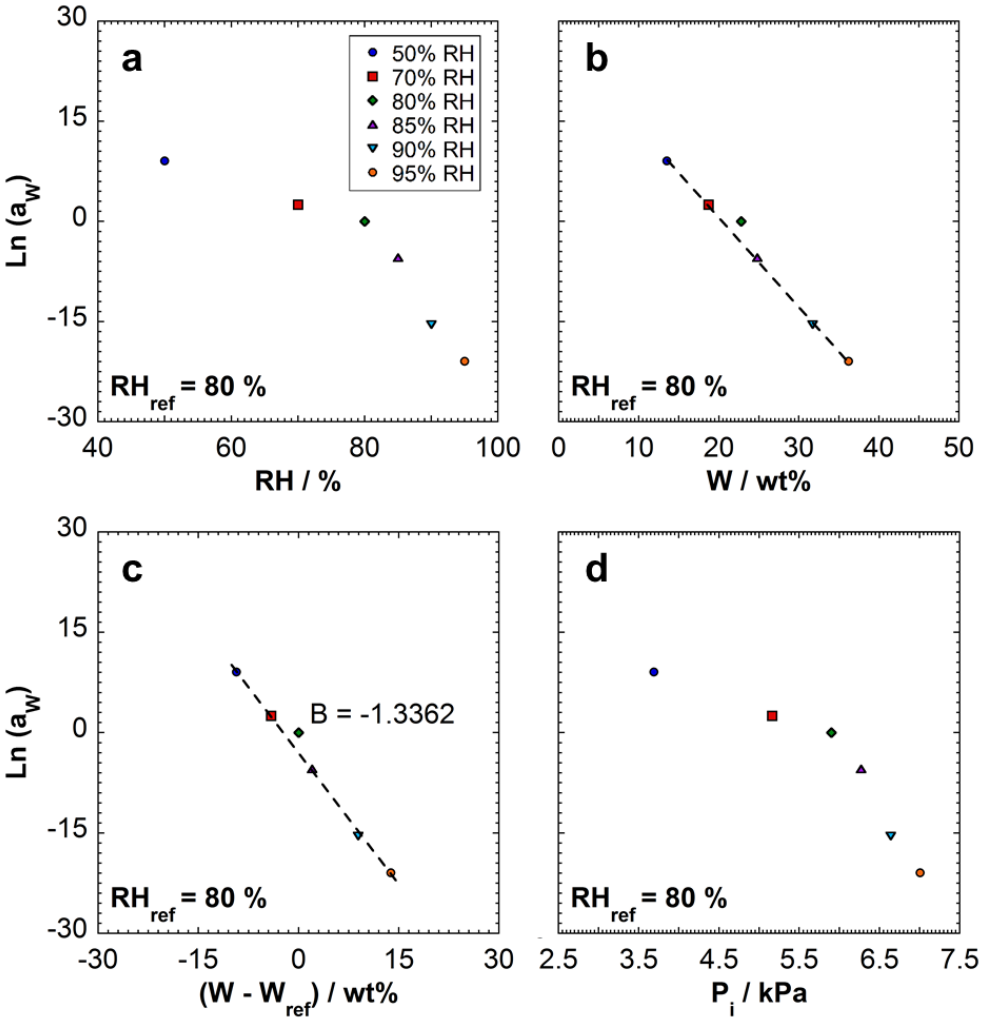

Figure 4.17 Water-dependent shift factor (a_W) data as a function of: a) relative humidity; b) water content in the PEC (ln a_W = -1.3362 W + 27.9342, R^2 = 0.9753); c) water content in the PEC relative to a reference state (ln a_W = -1.3362 (W - W_{ref}) – 2.5316, R^2 = 0.9870); and d) partial vapor pressure. W_{ref}: W at the RH_{ref} (80% RH, 22.8 ± 0.5 wt%). RH_{ref} = 80% and T_{ref} = 40 ^oC.

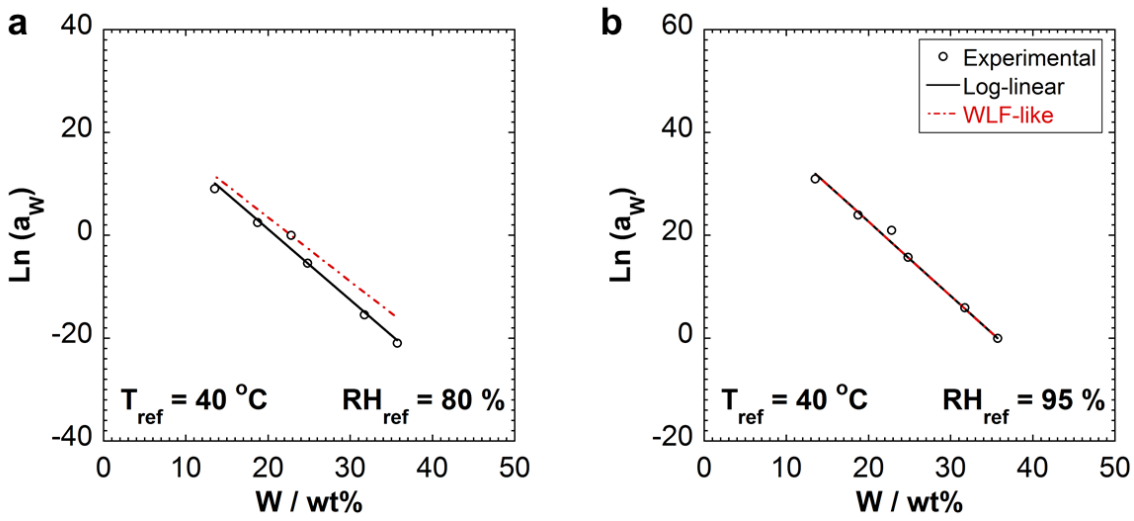

Figure 4.18 Ln(a_W) data fit with log-linear and WLF equations. a) RH_{ref} = 80% and b) RH_{ref} = 95%. T_{ref} = 40 °C. Legend in (b) applies to all panels.

Table 4.5 B, c, D_1 and D_2 values. T_{ref} = 40 °C.

RH_{ref} / %	W_{ref} ± SD[a] / wt%	B[b] / wt%$^{-1}$	c[b]	D_1[c]	D_2[c] / wt%
95	35.7 ± N/A	-1. 4428	0.0000	1.96 x 10^9	3.13 x 10^9
80	22.8 ± 0.5	-1. 3755	-2.6528	1.84 x 10^9	3.40 x 10^9

[a] Water content calculated from exposure of PEC specimens to humidity in a homebuilt humidity chamber
[b] B and c values obtained from fitting a_W data with a log-linear equation (Equation 4.8)
[c] D_1 and D_2 values obtained from fitting a_W data with a WLF-like equation (Equation 4.7)

Effects of relative humidity (water content) on the dynamic mechanical behavior of PECs and the application of the TWSP to PECs or PEMs have not been studied before. De and Cramer studied the effect of relative humidity (or water content) on the ion conductivity of PECs and explored the application of a time-humidity superposition principle.[55, 97] Most importantly, De and Cramer proposed two equations: 1) a log-linear equation that captured the relationship between

relative humidity and a humidity-dependent shift factor,[55] and 2) an equation that estimated the contribution of temperature to the humidity-dependent shift factor.[97] However, the latter was not supported with experimental data.

In this work, the application of the TWSP provided a_W data that was fitted with a log-linear equation (Equation 4.8) equivalent to the equation proposed by De et al.,[55] but for the dynamic mechanical behavior of a PAH/PAA PEC as a function of water content not RH. Additionally, an equation (**Equation 4.9**) combining the contributions of temperature and water content — obtained from the application of TTSP and TWSP to DMA experimental data — is proposed, where: a_c is the computational combined shift factor, E_a is the activation energy, R is the universal gas constant, T is temperature, T_{ref} is the reference temperature chosen during the application of the TTSP, B and c are the slope and the y-intercept of Equation 4.8, W is the water content in the PEC, and W_{ref} is the corresponding water content to the chosen reference relative humidity (RH_{ref}) during the application of the TWSP. Although Equation 4.9 seems similar to the equation proposed by Cramer et al.,[97] Equation 4.9 can actually be used to calculate a_c in order to predict a hygrotermal master curve.

$$a_c(T,W) = exp\left[\frac{E_a}{R}\left(\frac{1}{T}-\frac{1}{T_{ref}}\right) + \left[B\left(W - W_{ref}\right) + c\right]\right] \quad \textbf{(Equation 4.9)}$$

4.4 Conclusions

Application of superposition principles demonstrated equivalent effects of temperature and water content — under the studied temperature and relative humidity conditions — on the dynamic mechanical behavior of PAH/PAA PECs. Temperature and water content strongly influenced the storage modulus, where E' decreased with both increasing temperature and increasing water

content. For example, when temperature increased from 20 ºC to 50 ºC for data taken at 90% RH, E' (at 0.1 Hz) decreased from 1.6 x 10^9 Pa to 2.3 x 10^6 Pa. Additionally, when relative humidity (water content) increased from 80 to 95% (22.8 to 35.7 wt%) for data taken at 50 ºC, E' (at 0.1 Hz) decreased from 1.2 x 10^9 Pa to 2.3 x 10^6 Pa.

Time-temperature master curves were constructed for each relative humidity value (50 - 95%), where data at different temperatures was successfully superimposed at an arbitrarily chosen reference temperature. Successful data superposition validated the applicability of TTSP for salt-free PAH/PAA PECs. Additionally, temperature-dependent shift factor (a_T) data was successfully fitted with the Arrhenius equation, allowing for the prediction of a_T values for any temperature within the studied temperature range.

TWSP was successfully applied and validated for salt-free PAH/PAA PECs, through the creation of a time–water super master curve (or hygrothermal master curve). The effect of water content on the dynamic mechanical response of PAH/PAA PECs was quantified by a second shift factor, a_W. Most importantly, this water-dependent shift factor was found to be related to water content in the PEC (W) instead of the water content in the air (RH). Thus, the degree of plasticization in the PEC is controlled by its water content, which is determined by the relative humidity.[95] Consequently, the designation time-water superposition principle (TWSP) was deemed more appropriate than the more commonly used time-humidity superposition principle (THSP).

In conclusion, the rheological behavior of the PAH/PAA PECs is dominated by the dynamics of the ion-pairs as a function of water and temperature.

CHAPTER V

SUMMARY AND FUTURE WORK

5.1 Summary

In this dissertation, PEMs anticorrosive properties and PECs mechanical properties were studied.

In Chapters II and III, anticorrosive properties of BPEI/MMT PEM films were studied as a function of thickness, clay content, polymer molecular weight, substrate' surface finish, and application technique. All while keeping in mind industry requirements such as rapid application process and minimum impact on the environment.

In Chapter II, BPEI/MMT PEM films were prepared through spray-assisted layer-by-layer assembly onto an aluminum alloy substrate. LbL assembly does not easily allow for polymer-clay ratio tailoring, thus a BPEI/MMT PEM film with 25 wt% clay content was obtained. The anticorrosive properties of the PEM coating/substrate system were assessed through salt spray testing — a standard accelerated corrosion test in the coatings industry — and electrochemical impedance spectroscopy, where corrosion protection improvement was observed with the thicker PEM films (~ 0.4 μm). Thus, a corrosion protection mechanism was proposed, where MMT provided a physical barrier to corrosive agents and BPEI provided surface buffering, both slowing down the corrosion process. These results were promising, especially because the BPEI/MMT PEM film was chromium-free and did not contain any additional corrosion inhibiting species. However, the application of these BPEI/MMT PEM films required long times — 2 hours for a 0.4 μm thick PEM film — which is unrealistic for industrial applications in the coatings industry.

In Chapter III, BPEI/MMT PEM films were prepared through a one-pot formulation technique, which allowed polymer-clay ratio tunability in the coating and was quickly applied onto a substrate through airbrushing. A correlation between film thickness and corrosion protection was found, where corrosion protection improved with increasing thickness. BPEI/MMT PEM films were prepared with three different polymer-clay ratios — 50:50, 20:80, and 10:90 — for which a relationship between polymer-clay ratio and corrosion protection was found. Increasing clay content in the film from 50 to 80 wt%, resulted in great improvement in the corrosion protection provided to the aluminum substrate. However, increasing the clay content in the film even more from 80 to 90 wt%, resulted in lesser corrosion protection. These results evidenced the important roles of both BPEI and MMT in the PEM coating, where MMT provided a physical barrier and BPEI provided surface buffering and structural support. Additionally, the role of BPEI's molecular weight on the anticorrosion properties of the PEM coating was evaluated. BPEI/MMT PEM films, with a 20:80 polymer-clay ratio, were prepared with two different BPEI molecular weights (25,000 and 2,000,000 g-mol^{-1}) and assessed through EIS and SEM. The BPEI/MMT PEM film containing the higher molecular weight polymer evidenced a rapid breakdown upon exposure to the electrolyte solution during EIS testing. Early coating failure was attributed to a crater-like structure observed on the PEM coating surface. Finally, the effect of substrate' surface finish on the corrosion protection provided by the BPEI/MMT PEM film was evaluated, where a polished surface (*2,000 grit*) resulted in adhesion loss between the coating and the substrate, causing the acceleration of the corrosion process. In conclusion, Chapter III presents an environment-friendly BPEI/MMT PEM coating with a 20:80 polymer-clay ratio and a 2 μm thickness, as the coating that provided the best corrosion protection to the aluminum alloy substrate.

In Chapter IV the dynamic mechanical behavior of salt-free PAH/PAA PECs, assembled at pH 7.0, was systematically studied as a function of humidity (water content) and temperature. DMA data curves, containing information regarding the storage and loss moduli, were collected as a function of frequency, temperature, and relative humidity (water content). Data analysis evidenced water and temperature effects on PAH/PAA PECs dynamics: a) at a small-scale water causes a stiffening mechanism due to the increase of polyelectrolyte-water hydrogen bonding with increasing water content in the PEC; and b) the strength of temperature effects in the dynamics of the PEC depends on the water content in the PEC, where temperature had a stronger effect on samples exposed to RH $\geq$ 80%. Finally, TTSP and TWSP were successfully applied and validated for the PAH/PAA PECs.

5.2 Future Work

5.2.1 Anticorrosive Properties of PEMs

Even though Chapters II and III presented excellent corrosion protection achieved with a BPEI/MMT PEM film containing a 20:80 polymer-clay ratio, more work is needed in order to accomplish corrosion protection comparable to the one provided by chromium conversion coatings. This can accomplished in two ways: 1) Including an environment-friendly corrosion inhibitor material (e.g., 8HQ) in the coating matrix through nanoreservoirs or microcapsules; and 2) including corrosion inhibitor species (e.g., Cerium) in small dosages through chemical modification of MMT. Additionally, it is necessary to study the mechanical properties of the BPEI/MMT PEM coatings, because a balance between corrosion protection and mechanical performance is necessary for all coating systems. Finally, all possible versions of the BPEI/MMT PEM film need to be assessed in full coating systems to determine their corrosion protection and

mechanical behavior under real conditions of use (e.g., stress, chipping, temperature, humidity, etc).

5.2.2 Mechanical Properties of PECs

Chapter IV presented a systematic analysis of PAH/PAA PECs dynamic mechanical behavior as a function of frequency, temperature and relative humidity. However, this analysis was only performed for PAH/PAA PECs assembled at pH 7.0. pH is a critical factor in PECs and PEMs containing at least one weak PE (e.g., PAH and PAA). pH affects PECs and PEMs morphology and properties. Zhang et al.,[34] for example, showed the effect of assembly pH on PAH/PAA PECs glass transition temperature (**Figure 5.1**). Zhang showed that their intrinsic ion pairing — directly related to the composition — increased with increasing pH. This increase in the intrinsic ion pairing resulted in PECs stiffening, evidenced by an increase in T_g. As covered in Chapter I, PECs and PEMs thermal and mechanical properties are directly correlated, thus an increase in T_g could translate into higher moduli. Nolte et al.,[95] studied the effect of assembly pH on PAH/PAA PEMs Young's modulus. He showed that swelling and plasticization differ as a function of assembly pH, where PAH/PAA PEMs assembled at pH 2.5 demonstrated abrupt swelling and some antiplasticization as a function of relative humidity.

Changes in the properties of PECs containing at least one weak PE occur due to the change in ionic groups dissociation (charge density).[3] It is expected that for PECs assembled at pH values of 3.5 or 9.0, pH will play an important role in PECs mechanical properties. Thus, it is important to study the dynamic mechanical behavior of PAH/PAA PECs assembled at different pH values as a function of RH and temperature.

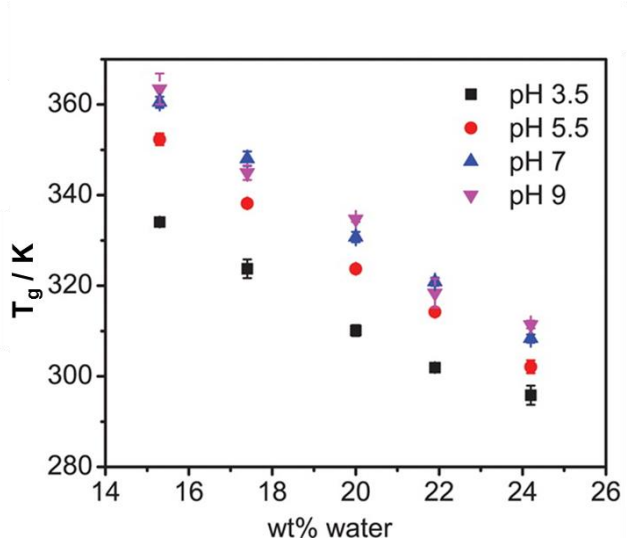

Figure 5.1 PAH/PAA PECs T_g as a function of assembly pH and water content. T_g increases with increasing assembly pH. Adapted with permission from reference [34]. Copyright 2016 American Chemical Society.

REFERENCES

1. Bungenberg De Jong, H.G. and H.R. Kruyt, *Coacervation (partial miscibility in colloid systems).* Proc. K. Ned. Akad. Wet., 1929. **32**: p. 849-856.
2. Reisch, A., et al., *Compact Saloplastic Poly(Acrylic Acid)/Poly(Allylamine) Complexes: Kinetic Control Over Composition, Microstructure, and Mechanical Properties.* Advanced Functional Materials, 2013. **23**(6): p. 673-682.
3. Meka, V.S., et al., *A comprehensive review on polyelectrolyte complexes.* Drug Discovery Today, 2017. **22**(11): p. 1697-1706.
4. Michaels, A.S., *Polyelectrolyte Complexes.* Industrial & Engineering Chemistry, 1965. **57**(10): p. 32-40.
5. Michaels, A.S. and R.G. Miekka, *Polycation-polyanion complexes: Preparation and properties of Poly-(vinylbenzyltrimethylammonium) Poly-(styrenesulfonate).* The Journal of Physical Chemistry, 1961. **65**(10): p. 1765-1773.
6. Olek, M., et al., *Layer-by-Layer Assembled Composites from Multiwall Carbon Nanotubes with Different Morphologies.* Nano Letters, 2004. **4**(10): p. 1889-1895.
7. Hyder, M.N., et al., *Layer-by-Layer Assembled Polyaniline Nanofiber/Multiwall Carbon Nanotube Thin Film Electrodes for High-Power and High-Energy Storage Applications.* ACS Nano, 2011. **5**(11): p. 8552-8561.
8. Fávero, V.O., et al., *Layer-by-layer nanostructured supercapacitor electrodes consisting of ZnO nanoparticles and multi-walled carbon nanotubes.* Journal of Materials Science, 2018. **53**(9): p. 6719-6728.
9. Cho, C., et al., *Stretchable electrically conductive and high gas barrier nanocomposites.* Journal of Materials Chemistry C, 2018. **6**(8): p. 2095-2104.

10. De, S. and J.L. Lutkenhaus, *Corrosion behaviour of eco-friendly airbrushed reduced graphene oxide-poly(vinyl alcohol) coatings.* Green Chemistry, 2018. **20**(2): p. 506-514.

11. Jeon, J.-W., S.R. Kwon, and J.L. Lutkenhaus, *Polyaniline nanofiber/electrochemically reduced graphene oxide layer-by-layer electrodes for electrochemical energy storage.* Journal of Materials Chemistry A, 2015. **3**(7): p. 3757-3767.

12. Kwon, S.R., et al., *Mechanically Strong Graphene/Aramid Nanofiber Composite Electrodes for Structural Energy and Power.* ACS Nano, 2017. **11**(7): p. 6682-6690.

13. Kwon, S.R., et al., *Robust and Flexible Aramid Nanofiber/Graphene Layer-by-Layer Electrodes.* ACS Applied Materials & Interfaces, 2017. **9**(20): p. 17125-17135.

14. Kwon, S.R., J.-W. Jeon, and J.L. Lutkenhaus, *Sprayable, paintable layer-by-layer polyaniline nanofiber/graphene electrodes.* RSC Advances, 2015. **5**(20): p. 14994-15001.

15. Suarez-Martinez, P.C., et al., *Spray-On Polymer–Clay Multilayers as a Superior Anticorrosion Metal Pretreatment.* Macromolecular Materials and Engineering, 2017. **302**(6): p. 1600552-n/a.

16. Suarez-Martinez, P.C., et al., *Polymer-clay nanocomposite coatings as efficient, environment-friendly surface pretreatments for aluminum alloy 2024-T3.* Electrochimica Acta, 2018. **260**: p. 73-81.

17. Chakraborty, U., et al., *Organic-inorganic hybrid layer-by-layer electrostatic self-assembled film of cationic dye Methylene Blue and a clay mineral: Spectroscopic and Atomic Force microscopic investigations.* Journal of Luminescence, 2017. **187**: p. 322-332.

18. Qiu, X., et al., *Flame retardant coatings prepared using layer by layer assembly: A review*. Chemical Engineering Journal, 2018. **334**: p. 108-122.

19. Rodrigues, J.R., N.M. Alves, and J.F. Mano, *Nacre-inspired nanocomposites produced using layer-by-layer assembly: Design strategies and biomedical applications.* Materials Science and Engineering: C, 2017. **76**: p. 1263-1273.

20. Holder, K.M., R.J. Smith, and J.C. Grunlan, *A review of flame retardant nanocoatings prepared using layer-by-layer assembly of polyelectrolytes.* Journal of Materials Science, 2017. **52**(22): p. 12923-12959.

21. Lutkenhaus, J.L., et al., *Anisotropic Structure and Transport in Self-Assembled Layered Polymer−Clay Nanocomposites.* Langmuir, 2007. **23**(16): p. 8515-8521.

22. Tsurko, E.S., et al., *Large Scale Self-Assembly of Smectic Nanocomposite Films by Doctor Blading versus Spray Coating: Impact of Crystal Quality on Barrier Properties.* Macromolecules, 2017. **50**(11): p. 4344-4350.

23. O'Neal, J.T., et al., *Hydrogen-bonded polymer nanocomposites containing discrete layers of gold nanoparticles.* Journal of Colloid and Interface Science, 2017. **485**: p. 260-268.

24. Fu, J., Q. Wang, and J.B. Schlenoff, *Extruded Superparamagnetic Saloplastic Polyelectrolyte Nanocomposites.* ACS Applied Materials & Interfaces, 2015. **7**(1): p. 895-901.

25. Eom, T., et al., *Nanoarchitecturing of Natural Melanin Nanospheres by Layer-by-Layer Assembly: Macroscale Anti-inflammatory Conductive Coatings with Optoelectronic Tunability.* Biomacromolecules, 2017. **18**(6): p. 1908-1917.

26. An, H., et al., *Surface-agnostic highly stretchable and bendable conductive MXene multilayers.* Science Advances, 2018. **4**(3).

27. Schaaf, P. and J.B. Schlenoff, *Saloplastics: Processing Compact Polyelectrolyte Complexes.* Advanced Materials, 2015. **27**(15): p. 2420-2432.

28. Richardson, J.J., M. Björnmalm, and F. Caruso, *Technology-driven layer-by-layer assembly of nanofilms.* Science, 2015. **348**(6233).

29. Porcel, C.H. and J.B. Schlenoff, *Compact Polyelectrolyte Complexes: "Saloplastic" Candidates for Biomaterials.* Biomacromolecules, 2009. **10**(11): p. 2968-2975.

30. Liu, Y., et al., *Rheological characterization of liquid-to-solid transitions in bulk polyelectrolyte complexes.* Soft Matter, 2017.

31. Shamoun, R.F., et al., *Thermal Transformations in Extruded Saloplastic Polyelectrolyte Complexes.* Macromolecules, 2012. **45**(24): p. 9759-9767.

32. Sukhishvili, S.A., E. Kharlampieva, and V. Izumrudov, *Where Polyelectrolyte Multilayers and Polyelectrolyte Complexes Meet.* Macromolecules, 2006. **39**(26): p. 8873-8881.

33. Zhang, R., et al., *Role of Salt and Water in the Plasticization of PDAC/PSS Polyelectrolyte Assemblies.* The Journal of Physical Chemistry B, 2017. **121**(1): p. 322-333.

34. Zhang, Y., et al., *Effect of Water on the Thermal Transition Observed in Poly(allylamine hydrochloride)–Poly(acrylic acid) Complexes.* Macromolecules, 2016. **49**(19): p. 7563-7570.

35. Turgeon, S.L., C. Schmitt, and C. Sanchez, *Protein–polysaccharide complexes and coacervates.* Current Opinion in Colloid & Interface Science, 2007. **12**(4): p. 166-178.

36. Decher, G., *Fuzzy Nanoassemblies: Toward Layered Polymeric Multicomposites.* Science, 1997. **277**(5330): p. 1232-1237.

37. Bieker, P. and M. Schönhoff, *Linear and Exponential Growth Regimes of Multilayers of Weak Polyelectrolytes in Dependence on pH.* Macromolecules, 2010. **43**(11): p. 5052-5059.

38. Shao, L. and J.L. Lutkenhaus, *Thermochemical properties of free-standing electrostatic layer-by-layer assemblies containing poly(allylamine hydrochloride) and poly(acrylic acid).* Soft Matter, 2010. **6**(14): p. 3363-3369.

39. Selin, V., J.F. Ankner, and S.A. Sukhishvili, *Diffusional Response of Layer-by-Layer Assembled Polyelectrolyte Chains to Salt Annealing.* Macromolecules, 2015. **48**(12): p. 3983-3990.

40. Selin, V., J.F. Ankner, and S.A. Sukhishvili, *Nonlinear Layer-by-Layer Films: Effects of Chain Diffusivity on Film Structure and Swelling.* Macromolecules, 2017. **50**(16): p. 6192-6201.

41. O'Neal, J.T., et al., *QCM-D Investigation of Swelling Behavior of Layer-by-Layer Thin Films upon Exposure to Monovalent Ions.* Langmuir, 2018. **34**(3): p. 999-1009.

42. Xiang, F., et al., *Improving the Gas Barrier Property of Clay–Polymer Multilayer Thin Films Using Shorter Deposition Times.* ACS Applied Materials & Interfaces, 2014. **6**(9): p. 6040-6048.

43. Hagen, D.A., L. Saucier, and J.C. Grunlan, *Controlling Effective Aspect Ratio and Packing of Clay with pH for Improved Gas Barrier in Nanobrick Wall Thin Films.* ACS Applied Materials & Interfaces, 2014. **6**(24): p. 22914-22919.

44. Kouji, F., et al., *Fabrication of Layer-by-Layer Self-Assembly Films Using Roll-to-Roll Process.* Japanese Journal of Applied Physics, 2005. **44**(1L): p. L126.

45. Li, Y., X. Wang, and J. Sun, *Layer-by-layer assembly for rapid fabrication of thick polymeric films.* Chemical Society Reviews, 2012. **41**(18): p. 5998-6009.

46. Dalmoro, A., et al., *Hydrophilic drug encapsulation in shell-core microcarriers by two stage polyelectrolyte complexation method.* International Journal of Pharmaceutics, 2017. **518**(1): p. 50-58.

47. Bigucci, F., et al., *Vaginal inserts based on chitosan and carboxymethylcellulose complexes for local delivery of chlorhexidine: Preparation, characterization and antimicrobial activity.* International Journal of Pharmaceutics, 2015. **478**(2): p. 456-463.

48. Insua, I., et al., *Preparation and antimicrobial evaluation of polyion complex (PIC) nanoparticles loaded with polymyxin B.* European Polymer Journal, 2017. **87**: p. 478-486.

49. Moustafine, R.I., et al., *Indomethacin-containing interpolyelectrolyte complexes based on Eudragit® E PO/S 100 copolymers as a novel drug delivery system.* International Journal of Pharmaceutics, 2017. **524**(1): p. 121-133.

50. Bourganis, V., et al., *Polyelectrolyte complexes as prospective carriers for the oral delivery of protein therapeutics.* European Journal of Pharmaceutics and Biopharmaceutics, 2017. **111**: p. 44-60.

51. Cifani, N., et al., *Improved stability and efficacy of chitosan/pDNA complexes for gene delivery.* Biotechnology Letters, 2015. **37**(3): p. 557-565.

52. Jiang, R., et al., *Monodispersed Brush-Like Conjugated Polyelectrolyte Nanoparticles with Efficient and Visualized SiRNA Delivery for Gene Silencing.* Biomacromolecules, 2013. **14**(10): p. 3643-3652.

53. Wu, Q.-X., et al., *Characterization of novel lactoferrin loaded capsules prepared with polyelectrolyte complexes.* International Journal of Pharmaceutics, 2013. **455**(1): p. 124-131.

54. Reisch, A., et al., *On the Benefits of Rubbing Salt in the Cut: Self-Healing of Saloplastic PAA/PAH Compact Polyelectrolyte Complexes.* Advanced Materials, 2014. **26**(16): p. 2547-2551.

55. De, S., C. Cramer, and M. Schönhoff, *Humidity Dependence of the Ionic Conductivity of Polyelectrolyte Complexes.* Macromolecules, 2011. **44**(22): p. 8936-8943.

56. Chen, G.Y., et al., *Ultra-fast Hygrometer based on U-shaped Optical Microfiber with Nanoporous Polyelectrolyte Coating.* Scientific Reports, 2017. **7**(1): p. 7943.

57. Brown, P.S. and B. Bhushan, *Mechanically durable, superoleophobic coatings prepared by layer-by-layer technique for anti-smudge and oil-water separation.* Scientific Reports, 2015. **5**: p. 8701.

58. Syed, J.A., S. Tang, and X. Meng, *Super-hydrophobic multilayer coatings with layer number tuned swapping in surface wettability and redox catalytic anti-corrosion application.* Scientific Reports, 2017. **7**(1): p. 4403.

59. Guan, B., et al., *Establishing Antibacterial Multilayer Films on the Surface of Direct Metal Laser Sintered Titanium Primed with Phase-Transited Lysozyme.* Scientific Reports, 2016. **6**: p. 36408.

60. Shao, L., J.-W. Jeon, and J.L. Lutkenhaus, *Polyaniline nanofiber/vanadium pentoxide sprayed layer-by-layer electrodes for energy storage.* Journal of Materials Chemistry A, 2014. **2**(35): p. 14421-14428.

61. Seo, J., et al., *Development of Surface Morphology in Multilayered Films Prepared by Layer-by-Layer Deposition Using Poly(acrylic acid) and Hydrophobically Modified Poly(ethylene oxide).* Macromolecules, 2007. **40**(11): p. 4028-4036.

62. Seo, J., et al., *Effect of the Layer-by-Layer (LbL) Deposition Method on the Surface Morphology and Wetting Behavior of Hydrophobically Modified PEO and PAA LbL Films.* Langmuir, 2008. **24**(15): p. 7995-8000.

63. Qin, S., et al., *Combined High Stretchability and Gas Barrier in Hydrogen-Bonded Multilayer Nanobrick Wall Thin Films.* ACS Applied Materials & Interfaces, 2017. **9**(9): p. 7903-7907.

64. Priolo, M.A., et al., *Recent Advances in Gas Barrier Thin Films via Layer-by-Layer Assembly of Polymers and Platelets.* Macromolecular Rapid Communications, 2015. **36**(10): p. 866-879.

65. Das, B.P. and M. Tsianou, *From polyelectrolyte complexes to polyelectrolyte multilayers: Electrostatic assembly, nanostructure, dynamics, and functional properties.* Advances in Colloid and Interface Science, 2017. **244**: p. 71-89.

66. Tiwari, A., L.H. Hihara, and J.W. Rawlins, *Intelligent coatings for corrosion control. First edition. [edited by] Atul Tiwari, James Rawlins, Lloyd Hihara*. 2015: Oxford, U.K. ; Waltham, MA : Butterworth-Heinemann, 2015.

First edition.

67. Zarras, P. and J.D. Stenger-Smith, *Chapter 3 - Smart Inorganic and Organic Pretreatment Coatings for the Inhibition of Corrosion on Metals/Alloys*, in *Intelligent Coatings for Corrosion Control*. 2015, Butterworth-Heinemann: Boston. p. 59-91.

68. Hihara, L.H., *Chapter 1 - Electrochemical Aspects of Corrosion-Control Coatings*, in *Intelligent Coatings for Corrosion Control*. 2015, Butterworth-Heinemann: Boston. p. 1-15.

69. Zhao, J., G. Frankel, and R.L. McCreery, *Corrosion Protection of Untreated AA-2024-T3 in Chloride Solution by a Chromate Conversion Coating Monitored with Raman Spectroscopy*. J Electrochem Soc, 1998. **145**(7): p. 2258-2264.

70. Błasiak, J. and J. Kowalik, *A comparison of the in vitro genotoxicity of tri- and hexavalent chromium.* Mutat Res-Gen Tox En, 2000. **469**(1): p. 135-145.

71. Wetterhahn, K.E. and J.W. Hamilton, *The Chromium Paradox in Modern Life Molecular basis of hexavalent chromium carcinogenicity: Effect on gene expression.* Sci Total Environ, 1989. **86**(1): p. 113-129.

72. Cui, L.-Y., et al., *Electrodeposition of TiO2 layer-by-layer assembled composite coating and silane treatment on Mg alloy for corrosion resistance.* Surface and Coatings Technology, 2017. **324**: p. 560-568.

73. Zhao, Y.-B., et al., *Corrosion resistance and adhesion strength of a spin-assisted layer-by-layer assembled coating on AZ31 magnesium alloy.* Applied Surface Science, 2018. **434**: p. 787-795.

74. Gomes, E.C. and M.A.S. Oliveira, *Corrosion protection by multilayer coating using layer-by-layer technique.* Surface and Coatings Technology, 2011. **205**(8): p. 2857-2864.

75. Skorb, E.V. and D.V. Andreeva, *Self-healing properties of layer-by-layer assembled multilayers.* Polymer International, 2015. **64**(6): p. 713-723.

76. Andreeva, D.V., et al., *Buffering polyelectrolyte multilayers for active corrosion protection.* Journal of Materials Chemistry, 2008. **18**(15): p. 1738-1740.

77. Andreeva, D.V., et al., *Self-Healing Anticorrosion Coatings Based on pH-Sensitive Polyelectrolyte/Inhibitor Sandwichlike Nanostructures.* Adv Mater, 2008. **20**(14): p. 2789-2794.

78. Li, P., et al., *Highly effective anti-corrosion epoxy spray coatings containing self-assembled clay in smectic order.* Journal of Materials Chemistry A, 2015. **3**(6): p. 2669-2676.

79. Kachurina, O., et al., *Corrosion protection with synergistic LBL/Ormosil nanostructured thin films.* Int J Nanotechnol, 2004. **1**(3): p. 347-365.

80. Westcott, S.L., et al. *Corrosion protection by multifunctional stratified coatings*. in *2004 NSTI nanotechnology conference and trade show—NSTI nanotech*. 2004.

81. Andreeva, D.V., E.V. Skorb, and D.G. Shchukin, *Layer-by-Layer Polyelectrolyte/Inhibitor Nanostructures for Metal Corrosion Protection.* ACS Applied Materials & Interfaces, 2010. **2**(7): p. 1954-1962.

82. Skorb, E.V., et al., *Surface-Modified Mesoporous SiO2 Containers for Corrosion Protection.* Advanced Functional Materials, 2009. **19**(15): p. 2373-2379.

83. Leal, D.A., et al., *Smart coating based on double stimuli-responsive microcapsules containing linseed oil and benzotriazole for active corrosion protection.* Corrosion Science, 2018. **130**: p. 56-63.

84. Izadi, M., T. Shahrabi, and B. Ramezanzadeh, *Synthesis and characterization of an advanced layer-by-layer assembled Fe3O4/polyaniline nanoreservoir filled with Nettle extract as a green corrosion protective system.* Journal of Industrial and Engineering Chemistry, 2018. **57**: p. 263-274.

85. Liu, X., et al., *Improvement of active corrosion protection of carbon steel by water-based epoxy coating with smart CeO2 nanocontainers.* Progress in Organic Coatings, 2018. **115**: p. 195-204.

86. Grunlan, J.C., L. Liu, and O. Regev, *Weak polyelectrolyte control of carbon nanotube dispersion in water.* Journal of Colloid and Interface Science, 2008. **317**(1): p. 346-349.

87. Wang, Q. and J.B. Schlenoff, *The Polyelectrolyte Complex/Coacervate Continuum.* Macromolecules, 2014. **47**(9): p. 3108-3116.

88. Zhang, L., et al., *Ion Conduction in Poly(ethylene oxide) Ionically Assembled Complexes.* Macromolecules, 2011. **44**(24): p. 9723-9730.

89. Hariri, H.H., A.M. Lehaf, and J.B. Schlenoff, *Mechanical Properties of Osmotically Stressed Polyelectrolyte Complexes and Multilayers: Water as a Plasticizer.* Macromolecules, 2012. **45**(23): p. 9364-9372.

90. Shamoun, R.F., A. Reisch, and J.B. Schlenoff, *Extruded Saloplastic Polyelectrolyte Complexes.* Advanced Functional Materials, 2012. **22**(9): p. 1923-1931.

91. Instruments, T., *Dynamic Mechanical Analysis: Basic Theory & Applications Training*. TA Instruments. p. 85.

92. Lutkenhaus, J.L., et al., *Elastomeric Flexible Free-Standing Hydrogen-Bonded Nanoscale Assemblies.* Journal of the American Chemical Society, 2005. **127**(49): p. 17228-17234.

93. Mueller, R., et al., *Melting of PDADMAC/PSS Capsules Investigated with AFM Force Spectroscopy*. Macromolecules, 2005. **38**(23): p. 9766-9771.

94. Jaber, J.A. and J.B. Schlenoff, *Mechanical Properties of Reversibly Cross-Linked Ultrathin Polyelectrolyte Complexes.* Journal of the American Chemical Society, 2006. **128**(9): p. 2940-2947.

95. Nolte, A.J., et al., *Effect of Relative Humidity on the Young's Modulus of Polyelectrolyte Multilayer Films and Related Nonionic Polymers.* Macromolecules, 2008. **41**(15): p. 5793-5798.

96. Cranston, E.D., et al., *Determination of Young's Modulus for Nanofibrillated Cellulose Multilayer Thin Films Using Buckling Mechanics.* Biomacromolecules, 2011. **12**(4): p. 961-969.

97. Cramer, C., S. De, and M. Schönhoff, *Time-Humidity-Superposition Principle in Electrical Conductivity Spectra of Ion-Conducting Polymers.* Physical Review Letters, 2011. **107**(2): p. 028301.

98. Lee, S.-W. and D. Lee, *Integrated Study of Water Sorption/Desorption Behavior of Weak Polyelectrolyte Layer-by-Layer Films.* Macromolecules, 2013. **46**(7): p. 2793-2799.

99. Spruijt, E., M.A. Cohen Stuart, and J. van der Gucht, *Linear Viscoelasticity of Polyelectrolyte Complex Coacervates.* Macromolecules, 2013. **46**(4): p. 1633-1641.

100. Toda, M., et al., *Thin Polyelectrolyte Multilayers Made by Inkjet Printing and Their Characterization by Nanomechanical Cantilever Sensors.* The Journal of Physical Chemistry C, 2014. **118**(15): p. 8071-8078.

101. Priftis, D., et al., *Ternary, Tunable Polyelectrolyte Complex Fluids Driven by Complex Coacervation.* Macromolecules, 2014. **47**(9): p. 3076-3085.

102. Tekaat, M., et al., *Scaling properties of the shear modulus of polyelectrolyte complex coacervates: a time-pH superposition principle.* Physical Chemistry Chemical Physics, 2015. **17**(35): p. 22552-22556.

103. Costa, R.R., et al., *Compact Saloplastic Membranes of Natural Polysaccharides for Soft Tissue Engineering.* Chemistry of Materials, 2015. **27**(21): p. 7490-7502.

104. Rodrigues, M.N., et al., *Chitosan/Chondroitin Sulfate Membranes Produced by Polyelectrolyte Complexation for Cartilage Engineering.* Biomacromolecules, 2016. **17**(6): p. 2178-2188.

105. Zhu, F., et al., *Processing tough supramolecular hydrogels with tunable strength of polyion complex.* Polymer, 2016. **95**: p. 9-17.

106. Gai, M., et al., *Patterned Microstructure Fabrication: Polyelectrolyte Complexes vs Polyelectrolyte Multilayers.* Scientific Reports, 2016. **6**: p. 37000.

107. Zhang, H., et al., *Self-Healing of Bulk Polyelectrolyte Complex Material as a Function of pH and Salt.* ACS Applied Materials & Interfaces, 2016. **8**(39): p. 26258-26265.

108. Cuthbert, T.J., et al., *Self-Healing Polyphosphonium Ionic Networks.* Macromolecules, 2017. **50**(14): p. 5253-5260.

109. Wang, Y., et al., *Rheological behavior and self-healing of hydrogen-bonded complexes of a triblock Pluronic® copolymer with a weak polyacid.* Journal of Rheology, 2017. **61**(6): p. 1103-1119.

110. Sadman, K., et al., *Influence of Hydrophobicity on Polyelectrolyte Complexation.* Macromolecules, 2017. **50**(23): p. 9417-9426.

111. Lyu, X., B. Clark, and A.M. Peterson, *Thermal transitions in and structures of dried polyelectrolytes and polyelectrolyte complexes.* Journal of Polymer Science Part B: Polymer Physics, 2017. **55**(8): p. 684-691.

112. Wang, C., et al., *A family of mechanically adaptive supramolecular graphene oxide/poly(ethylenimine) hydrogels from aqueous assembly.* Soft Matter, 2017. **13**(6): p. 1161-1170.

113. Wang, L., et al., *A multifunctional supramolecular hydrogel: preparation, properties and molecular assembly.* Soft Matter, 2018. **14**(4): p. 566-573.

114. Ali, S. and V. Prabhu, *Relaxation Behavior by Time-Salt and Time-Temperature Superpositions of Polyelectrolyte Complexes from Coacervate to Precipitate.* Gels, 2018. **4**(1): p. 11.

115. Marciel, A.B., S. Srivastava, and M.V. Tirrell, *Structure and rheology of polyelectrolyte complex coacervates.* Soft Matter, 2018. **14**(13): p. 2454-2464.

116. Huang, S., et al., *Effect of small molecules on the phase behavior and coacervation of aqueous solutions of poly(diallyldimethylammonium chloride) and poly(sodium 4-styrene sulfonate).* Journal of Colloid and Interface Science, 2018. **518**: p. 216-224.

117. Nolte, A.J., M.F. Rubner, and R.E. Cohen, *Determining the Young's Modulus of Polyelectrolyte Multilayer Films via Stress-Induced Mechanical Buckling Instabilities.* Macromolecules, 2005. **38**(13): p. 5367-5370.

118. G. Koch, J.V., N. Thompson, O. Moghissi, M. Gould, J. Payer, *International Measures of Prevention, Application, and Economics of Corrosion Technologies Study*. 2016, NACE International.

119. Osborne, J.H., *Observations on chromate conversion coatings from a sol–gel perspective.* Progress in Organic Coatings, 2001. **41**(4): p. 280-286.

120. Vignati, D.A.L., et al., *Chromium(VI) is more toxic than chromium(III) to freshwater algae: A paradigm to revise?* Ecotox Environ Safe, 2010. **73**(5): p. 743-749.

121. Katzman, H.A., et al., *Corrosion-protective chromate coatings on aluminum.* Applications of Surface Science, 1979. **2**(3): p. 416-432.

122. Kendig, M., et al., *Role of hexavalent chromium in the inhibition of corrosion of aluminum alloys.* Surface and Coatings Technology, 2001. **140**(1): p. 58-66.

123. Ilevbare, G.O., et al., *Inhibition of Pitting Corrosion on Aluminum Alloy 2024-T3: Effect of Soluble Chromate Additions vs Chromate Conversion Coating.* Corrosion, 2000. **56**(3): p. 227-242.

124. Zhuk, A., R. Mirza, and S. Sukhishvili, *Multiresponsive Clay-Containing Layer-by-Layer Films.* ACS Nano, 2011. **5**(11): p. 8790-8799.

125. Yeh, J.-M., et al., *Enhancement of Corrosion Protection Effect in Polyaniline via the Formation of Polyaniline−Clay Nanocomposite Materials.* Chemistry of Materials, 2001. **13**(3): p. 1131-1136.

126. Kunz, D.A., et al., *Clay-Based Nanocomposite Coating for Flexible Optoelectronics Applying Commercial Polymers.* ACS Nano, 2013. **7**(5): p. 4275-4280.

127. Priolo, M.A., D. Gamboa, and J.C. Grunlan, *Transparent Clay−Polymer Nano Brick Wall Assemblies with Tailorable Oxygen Barrier.* ACS Appl Mater Inter, 2010. **2**(1): p. 312-320.

128. Navarchian, A.H., M. Joulazadeh, and F. Karimi, *Investigation of corrosion protection performance of epoxy coatings modified by polyaniline/clay nanocomposites on steel surfaces.* Prog Org Coat, 2014. **77**(2): p. 347-353.

129. Singh-Beemat, J. and J.O. Iroh, *Characterization of corrosion resistant clay/epoxy ester composite coatings and thin films.* Progress in Organic Coatings, 2012. **74**(1): p. 173-180.

130. Olad, A. and A. Rashidzadeh, *Preparation and anticorrosive properties of PANI/Na-MMT and PANI/O-MMT nanocomposites.* Progress in Organic Coatings, 2008. **62**(3): p. 293-298.

131. Huffer, S., et al., *Modified sheet silicates as corrosion protection*. 2013, Google Patents.

132. Zhu, D. and W.J. van Ooij, *Corrosion protection of AA 2024-T3 by bis-[3-(triethoxysilyl)propyl]tetrasulfide in neutral sodium chloride solution. Part 1: corrosion of AA 2024-T3.* Corrosion Science, 2003. **45**(10): p. 2163-2175.

133. Narayanan, T.S., *Surface pretreatment by phosphate conversion coatings–a review*. Rev. Adv. mater. sci, 2005. **9**: p. 130-177.

134. Hamdy, A.S. and H. Hussien, *Deposition, characterization and electrochemical properties of permanganate-based coating treatments over ZE41 Mg-Zn-rare earth alloy.* Int. J. Electrochem. Sci, 2013. **8**: p. 11386-11402.

135. Bhatt, H. *Trivalent Chromium Conversion Coating for Corrosion Protection of Aluminum Surface*. in *2009 DoD Corrosion Conference*. 2009.

136. Wang, S.H., C.S. Liu, and L. Wang. *A comparative study of zirconium-based coating on cold rolled steel*. in *Advanced Materials Research*. 2011. Trans Tech Publ.

137. Hamdy, A.S. and M. Farahat, *Chrome-free zirconia-based protective coatings for magnesium alloys.* Surface and Coatings Technology, 2010. **204**(16–17): p. 2834-2840.

138. Zheludkevich, M., I.M. Salvado, and M. Ferreira, *Sol–gel coatings for corrosion protection of metals.* J Mater Chem, 2005. **15**(48): p. 5099-5111.

139. Wittmar, A., et al., *Simple preparation routes for corrosion protection hybrid sol-gel coatings on AA 2024.* Surface and Interface Analysis, 2012. **44**(1): p. 70-77.

140. Wapner, K., M. Stratmann, and G. Grundmeier, *Structure and stability of adhesion promoting aminopropyl phosphonate layers at polymer/aluminium oxide interfaces.* International Journal of Adhesion and Adhesives, 2008. **28**(1–2): p. 59-70.

141. Rohwerder, M., G. Grundmeier, and M. Stratmann, *Corrosion prevention by adsorbed organic monolayers and ultrathin plasma polymer films.* CORROSION TECHNOLOGY-NEW YORK AND BASEL-, 2002. **17**: p. 479-528.

142. de Leon, A. and R.C. Advincula, *Chapter 11 - Conducting Polymers with Superhydrophobic Effects as Anticorrosion Coating*, in *Intelligent Coatings for Corrosion Control*. 2015, Butterworth-Heinemann: Boston. p. 409-430.

143. Stankiewicz, A., I. Szczygieł, and B. Szczygieł, *Self-healing coatings in anti-corrosion applications.* Journal of Materials Science, 2013. **48**(23): p. 8041-8051.

144. Fan, F., et al., *Layer-by-Layer Assembly of a Self-Healing Anticorrosion Coating on Magnesium Alloys.* ACS Applied Materials & Interfaces, 2015. **7**(49): p. 27271-27278.

145. Luckachan, G.E. and V. Mittal, *Anti-corrosion behavior of layer by layer coatings of cross-linked chitosan and poly(vinyl butyral) on carbon steel.* Cellulose, 2015. **22**(5): p. 3275-3290.

146. Sonawane, S.H., et al., *Improved active anticorrosion coatings using layer-by-layer assembled ZnO nanocontainers with benzotriazole.* Chemical Engineering Journal, 2012. **189–190**: p. 464-472.

147. Farhat, T.R. and J.B. Schlenoff, *Corrosion control using polyelectrolyte multilayers.* Electrochemical and solid-state letters, 2002. **5**(4): p. B13-B15.

148. Schaaf, P., et al., *Spray-Assisted Polyelectrolyte Multilayer Buildup: from Step-by-Step to Single-Step Polyelectrolyte Film Constructions.* Advanced Materials, 2012. **24**(8): p. 1001-1016.

149. Kendig, M., et al., *Rapid electrochemical assessment of paint.* J Coating Technol, 1996. **68**(863).

150. Malwitz, M.M., et al., *Orientation of platelets in multilayered nanocomposite polymer films.* Journal of Polymer Science Part B: Polymer Physics, 2003. **41**(24): p. 3237-3248.

151. Palomino, L.E.M., et al., *Investigation of the corrosion behaviour of a bilayer cerium-silane pre-treatment on Al 2024-T3 in 0.1 M NaCl.* Electrochimica Acta, 2007. **52**(27): p. 7496-7505.

152. Zhu, D. and W.J. van Ooij, *Corrosion protection of AA 2024-T3 by bis-[3-(triethoxysilyl)propyl]tetrasulfide in sodium chloride solution.: Part 2: mechanism for corrosion protection.* Corros Sci, 2003. **45**(10): p. 2177-2197.

153. Zheludkevich, M.L., et al., *Nanostructured sol–gel coatings doped with cerium nitrate as pre-treatments for AA2024-T3: Corrosion protection performance.* Electrochimica Acta, 2005. **51**(2): p. 208-217.

154. Campestrini, P., E.P.M. van Westing, and J.H.W. de Wit, *Influence of surface preparation on performance of chromate conversion coatings on Alclad 2024 aluminium alloy: Part II: EIS investigation.* Electrochimica Acta, 2001. **46**(17): p. 2631-2647.

155. Yasakau, K.A., et al., *Influence of inhibitor addition on the corrosion protection performance of sol–gel coatings on AA2024.* Progress in Organic Coatings, 2008. **63**(3): p. 352-361.

156. Alexandre, M. and P. Dubois, *Polymer-layered silicate nanocomposites: preparation, properties and uses of a new class of materials.* Materials Science and Engineering: R: Reports, 2000. **28**(1): p. 1-63.

157. Gaikwad, K., *Overview on in Polymer-Nano Clay Composite Paper Coating for Packaging Application.* J Mater Sci Eng, 2015. **2015**.

158. Finšgar, M., et al., *Polyethyleneimine as a corrosion inhibitor for ASTM 420 stainless steel in near-neutral saline media.* Corrosion Science, 2009. **51**(3): p. 525-533.

159. Roberts, A.P., et al., *Gas permeation in silicon-oxide/polymer (SiOx/PET) barrier films: role of the oxide lattice, nano-defects and macro-defects.* J Membrane Sci, 2002. **208**(1–2): p. 75-88.

160. Wang, H. and R. Akid, *A room temperature cured sol–gel anticorrosion pre-treatment for Al 2024-T3 alloys.* Corrosion Science, 2007. **49**(12): p. 4491-4503.

161. Wise, S.S., et al., *Hexavalent chromium induces chromosome instability in human urothelial cells.* Toxicol Appl Pharm, 2016. **296**: p. 54-60.

162. Huang, J., et al., *Chromium contributes to human bronchial epithelial cell carcinogenesis by activating Gli2 and inhibiting autophagy.* Toxicol Res-UK, 2017. **6**(3): p. 324-332.

163. Ganapathy, S., et al., *Chromium IV exposure, via Src/Ras signaling, promotes cell transformation.* Mol Carcinogen, 2017: p. n/a-n/a.

164. Hughes, A.E., J.M.C. Mol, and M.L. Zheludkevich, *Springer Series in Materials Science : Active Protective Coatings : New-Generation Coatings for Metals*. 2016, Dordrecht, NL: Springer.

165. Wu, Q., et al., *Contamination, toxicity and speciation of heavy metals in an industrialized urban river: Implications for the dispersal of heavy metals.* Mar Pollut Bull, 2016. **104**(1–2): p. 153-161.

166. Jaishankar, M., et al., *Toxicity, mechanism and health effects of some heavy metals.* Interdiscip Toxicol, 2014. **7**(2): p. 60-72.

167. Hughes, A.E., J.M.C. Mol, and I.S. Cole, *10 - The cost and availability of rare earth-based corrosion inhibitors*, in *Rare Earth-Based Corrosion Inhibitors*. 2014, Woodhead Publishing. p. 291-305.

168. Wang, D. and G.P. Bierwagen, *Sol–gel coatings on metals for corrosion protection.* Prog Org Coat, 2009. **64**(4): p. 327-338.

169. Figueira, R., et al., *Hybrid Sol-Gel Coatings: Smart and Green Materials for Corrosion Mitigation.* Coatings, 2016. **6**(1): p. 12.

170. A. M. Pereira, G.P., B. D. Dunn, *Assessment of chemical conversion coatings for the protection of aluminium alloys*. 2008, European Space Agency.

171. Yeh, J.-M., et al., *Enhanced corrosion prevention effect of polysulfone–clay nanocomposite materials prepared by solution dispersion.* J Appl Polym Sci, 2004. **92**(1): p. 631-637.

172. Chang, K.-C., et al., *Comparative studies on the corrosion protection effect of DBSA-doped polyaniline prepared from in situ emulsion polymerization in the presence of*

hydrophilic Na+-MMT and organophilic organo-MMT clay platelets. Electrochim Acta, 2006. **51**(26): p. 5645-5653.

173. Yeh, J.-M., et al., *Comparative studies of the properties of poly(methyl methacrylate)–clay nanocomposite materials prepared by in situ emulsion polymerization and solution dispersion.* J Appl Polym Sci, 2004. **94**(5): p. 1936-1946.

174. Hagen, D.A., L. Saucier, and J.C. Grunlan, *Controlling Effective Aspect Ratio and Packing of Clay with pH for Improved Gas Barrier in Nanobrick Wall Thin Films.* ACS Appl Mater Inter, 2014. **6**(24): p. 22914-22919.

175. Song, Y., et al., *Edge Charge Neutralization of Clay for Improved Oxygen Gas Barrier in Multilayer Nanobrick Wall Thin Films.* ACS Appl Mater Inter, 2016. **8**(50): p. 34784-34790.

176. Qin, S., et al., *Combined High Stretchability and Gas Barrier in Hydrogen-Bonded Multilayer Nanobrick Wall Thin Films.* ACS Appl Mater Inter, 2017. **9**(9): p. 7903-7907.

177. Cui, Y., et al., *Gas barrier properties of polymer/clay nanocomposites.* RSC Adv, 2015. **5**(78): p. 63669-63690.

178. Lambert, J.F. and F. Bergaya, *Chapter 13.1 - Smectite–Polymer Nanocomposites*, in *Developments in Clay Science*, B. Faïza and L. Gerhard, Editors. 2013, Elsevier. p. 679-706.

179. Gürses, A., *Introduction to polymer-clay nanocomposites*. 2015: Singapore : Pan Stanford Publishing, [2015].

180. Holtz, R.D.K., W. D, *An introduction to geotechnical engineering*. 1981: Prentice-Hall

181. Alexandre, M. and P. Dubois, *Polymer-layered silicate nanocomposites: preparation, properties and uses of a new class of materials.* Mater Sci Eng R Rep, 2000. **28**(1–2): p. 1-63.

182. Vandewijngaarden, J., et al., *Gas Permeability Properties of Poly(3-hydroxybutyrate-co-3-hydroxyhexanoate).* J Polym Environ, 2014. **22**(4): p. 501-507.

183. Bonnel, K., C. Le Pen, and N. Pébère, *E.I.S. characterization of protective coatings on aluminium alloys.* Electrochim Acta, 1999. **44**(24): p. 4259-4267.

184. Carreira, A.F., et al., *Alternative corrosion protection pretreatments for aluminum alloys.* J Coat Technol Res, 2017. **14**(4): p. 879-892.

185. Yasakau, K.A., et al., *Active Corrosion Protection by Nanoparticles and Conversion Films of Layered Double Hydroxides.* Corrosion, 2014. **70**(5): p. 436-445.

186. Wu, J., et al., *In Situ Formation of Decavanadate-Intercalated Layered Double Hydroxide Films on AA2024 and their Anti-Corrosive Properties when Combined with Hybrid Sol Gel Films.* Materials, 2017. **10**(4): p. 426.

187. Lakshmi, R.V., et al., *EIS and XPS studies on the self-healing properties of Ce-modified silica-alumina hybrid coatings: Evidence for Ce(III) migration.* Surf Coat Tech, 2017. **309**: p. 363-370.

188. Lakshmi, R.V., et al., *Effect of surface pre-treatment by silanization on corrosion protection of AA2024-T3 alloy by sol–gel nanocomposite coatings.* Surf Coat Tech, 2014. **240**: p. 353-360.

189. Zhou, S.M., K. Tashiro, and T. Ii, *Confirmation of universality of time–humidity superposition principle for various water-absorbable polymers through dynamic viscoelastic measurements under controlled conditions of relative humidity and*

temperature. Journal of Polymer Science Part B: Polymer Physics, 2001. **39**(14): p. 1638-1650.

190. Chartoff, R.P., J.D. Menczel, and S.H. Dillman, *Dynamic Mechanical Analysis (DMA)*, in *Thermal Analysis of Polymers*. 2008, John Wiley & Sons, Inc. p. 401-409.

191. Van Gurp, M. and J. Palmen, *Time-temperature superposition for polymeric blends.* Rheol. Bull, 1998. **67**(1): p. 5-8.

192. Spruijt, E., et al., *Relaxation Dynamics at Different Time Scales in Electrostatic Complexes: Time-Salt Superposition.* Physical Review Letters, 2010. **105**(20): p. 208301.

193. Fabre, V., et al., *Time-Temperature-Water Content equivalence on dynamic mechanical response of polyamide 6,6.* Polymer.

194. Ishisaka, A. and M. Kawagoe, *Examination of the time–water content superposition on the dynamic viscoelasticity of moistened polyamide 6 and epoxy.* Journal of Applied Polymer Science, 2004. **93**(2): p. 560-567.

195. Instruments, T., *DMA-RH Accessory - Getting Started Guide*. 2013: p. 13.

196. Secrist, K.E. and A.J. Nolte, *Humidity Swelling/Deswelling Hysteresis in a Polyelectrolyte Multilayer Film.* Macromolecules, 2011. **44**(8): p. 2859-2865.

197. Fujita, H. and A. Kishimoto, *Diffusion-controlled stress relaxation in polymers. II. Stress relaxation in swollen polymers.* Journal of Polymer Science, 1958. **28**(118): p. 547-567.

198. Gabriel, L. and L.-S. Pearl, *Moisture effects on FM300 structural film adhesive: Stress relaxation, fracture toughness, and dynamic mechanical analysis.* Journal of Applied Polymer Science, 2005. **95**(5): p. 1285-1294.

199. A., P.K., et al., *Linear Hygrothermal Viscoelastic Characterization of Nafion NRE 211 Proton Exchange Membrane.* Fuel Cells, 2012. **12**(5): p. 787-799.

200. Thein, K. and E. Adi, *Underwater stress relaxation studies of nafion (perfluorosulfonate) ionomer membranes.* Journal of Polymer Science: Polymer Symposia, 1984. **71**(1): p. 203-219.

201. Li, G., P. Lee-Sullivan, and R.W. Thring, *Determination of Activation Energy for Glass Transition of an Epoxy Adhesive Using Dynamic Mechanical Analysis.* Journal of Thermal Analysis and Calorimetry, 2000. **60**(2): p. 377-390.

202. Capodagli, J. and R. Lakes, *Isothermal viscoelastic properties of PMMA and LDPE over 11 decades of frequency and time: a test of time–temperature superposition.* Rheologica Acta, 2008. **47**(7): p. 777-786.

203. Colby, R.H., *Breakdown of time-temperature superposition in miscible polymer blends.* Polymer, 1989. **30**(7): p. 1275-1278.

204. Yin, T.P., S.E. Lovell, and J.D. Ferry, *Viscoelastic Properties of Polyethylene Oxide in the Rubber-like State.* The Journal of Physical Chemistry, 1961. **65**(3): p. 534-538.

205. Alegria, A., E. Macho, and J. Colmenero, *Dynamic mechanical study of four amorphous polymers around and above the glass transition: breakdown of the time-temperature superposition principle in the frame of the coupling model.* Macromolecules, 1991. **24**(18): p. 5196-5202.

206. Keller, M.W., B.D. Jellison, and T. Ellison, *Moisture effects on the thermal and creep performance of carbon fiber/epoxy composites for structural pipeline repair.* Composites Part B: Engineering, 2013. **45**(1): p. 1173-1180.

207. Fabre, V., et al., *Time-Temperature-Water Content equivalence on dynamic mechanical response of polyamide 6,6.* Polymer, 2018. **137**: p. 22 - 29.

APPENDIX A

LIST OF MOVIES

2.1 Adhesion by tape test on the as prepared $(BPEI/MMT)_{40}$ LbL film to the AA2024-T3 substrate

3.1 Airbrushing of the BPEI/MMT one-pot mixture onto a substrate

3.2 Adhesion by tape test on the as prepared $(BPEI_{20}/MMT_{80})_3$ film to the A2024-T3 substrate

3.3 Adhesion by tape test on the as prepared $(BPEI_{20}/MMT_{80})_3$ film to the *2,000 grit* AA2024-T3 substrate